INSECT LOCOMOTION: CONTROL, STABILITY, AND OPTIMIZATION

A Dissertation

Presented to the Faculty of the Graduate School

of Cornell University

in Partial Fulfillment of the Requirements for the Degree of

Doctor of Philosophy

by

Robert Matthijs Noest

August 2017

INSECT LOCOMOTION:

CONTROL, STABILITY, AND OPTIMIZATION

Robert Matthijs Noest, Ph.D.

Cornell University 2017

In complex dynamical systems consisting of many interacting degrees of freedom it can be impossible to predict how any single one will behave. Yet, usually, out of the chaos emerge simple laws that guide the behavior of the system as a whole. Many examples exist in Nature, from the ideal gas law to superconductivity, and it can be expected that the same principle holds in the study of insect locomotion.

This thesis examines three aspects of insect locomotion and attempts to provide simple laws that guide them. First, the focus is on the steering control of a tiger beetle while it chases its prey. The steering is governed by a proportional controller with a distance dependent gain. Moreover, the same control law can be seen in the position that the front leg is placed at each individual step.

Next, this thesis provides insight into the principles that guide evolution as it drives morphological adaptations in flying insects. Using computer simulations of 3D flight, we find that the wing hinge position relative to the center of mass of a model fly has a significant effect on the lift production and only marginally affects flight stability. Most intriguing is the result that the nominal hinge position of a fruit fly optimizes its lift production and maximizes ascending speed, irrespective of stroke amplitude. This can be understood by looking at the coupling between the body and wing motions. We construct a new model, which shows that the maximum speed, associated with the maximum vertical lift, is

due to an antiresonance between the body and wing oscillations.

In addition, the evolutionary process from four-winged to two-winged flight is investigated. The four-winged dragonfly, an example of one of the oldest flying insects, flies with the body horizontal during steady state flight. In contrast, two-winged insects, which developed later, fly with their body pitched up vertically. The simulations presented here will show that during the evolutionary transition the flight style naturally switches from horizontal to vertical. This change must be accompanied by a switch from an asymmetric to a symmetric wing stroke in order to maintain flight. The results indicate that small changes to the wing size of a four-winged flyer require simultaneous large adaptations to the front wing pitch if successful flight is to be maintained.

Finally, the last chapter will report on the construction of an interactive insect flight simulator, where a human can control the insect flight by flapping a wing model in the lab. The system combines the previous insect flight simulations with real-time input of the wing beat. Initial results will be discussed, which indicate the setup and code are functioning properly. In addition, we show that a human can reproduce typical fruit fly flight and can control the longitudinal flight of a dragonfly. This setup allows for experiments that look at how control laws are developed and how they might change over time, but those experiments have yet to be performed.

BIOGRAPHICAL SKETCH

Robert Matthijs Noest grew up in Amsterdam, the Netherlands, where he attended the Vossius Gymnasium. He received his undergraduate degree from the University of Amsterdam in 2010 for a double major program in Math and Physics. He continued with a double masters in Mathematical and Theoretical Physics at the same university. As part of that degree he spend a year at the University of California at Berkeley, paid for by the prestigious Huygens Scholarship Programme, doing research on the Bethe Ansatz. In 2012 Robert started his PhD in Physics at Cornell University where he worked with Prof. Jane Wang on insect locomotion. He received a Prins Bernard Fellowship and a Dr. V. Ramachandra Rao Fellowship in support of his research while at Cornell.

Robert likes to play badminton in his spare time and was the treasurer at Cornell Badminton for three years. He was also part of the team that won the 2014 Ivy League Badminton Championships.

This thesis, just as most waking minutes of the past five years of my life, is dedicated to science and the advancement of knowledge.

ACKNOWLEDGEMENTS

First, I would like to thank my advisor, Jane Wang, for her mentorship throughout my studies. She was an indispensable guide as I tried to contribute my first original pieces of knowledge to the world. I would also like to thank my other committee members, Kyle Shen and Tomás Arias, for their help in getting this thesis over the finish line.

Thanks to my family for support and encouragement, whether from afar over the internet or when visiting Ithaca in person. I am grateful for all my friends that were also struggling towards a PhD. Together we made the bad parts bearable and the good parts enjoyable. Special thanks to Arthur and Bob, who came all the way from the Netherlands to visit me in Ithaca.

Last, but certainly not least, I would like to thank the Cornell Badminton Club and its members. Badminton has been my outlet for work stress for many years and I am grateful that I could continue playing here in Ithaca and in the region against many kind and excellent players.

TABLE OF CONTENTS

LIST OF TABLES

LIST OF FIGURES

CHAPTER 1

INTRODUCTION

At first glance the behavior of any organism may seem highly complex and usually appears to be the result of an intricate interplay of competing objectives [1–4]. Yet, when one looks through the noise and the constraints imposed on the organism by the physical world, it can turn out that its behavior is actually guided by a simple law [5–9]. Here, in this thesis, we will study these simple mathematical laws that underpin the behavior of the life that we observe.

Behavior in this context is the action of any organism or system that emerges as a result of exterior or interior stimuli, received either in the past or in the present [10]. For example, we will study how a tiger beetle chases its prey. In this case the behavior is the chasing pattern that we observe, which relates the current visual stimulus of the prey to the muscle output on its legs. However, this behavior was developed over time by incorporating all the beetle's past experiences with chasing prey and perhaps also results from specialized neural circuitry passed on through its DNA [11].

It might seem remarkable that the actions resulting from highly complex dynamical systems which feature large amounts of variables, such as the example above, could result in relatively simple behavioral laws. Yet, it turns out this is a common feature of collective phenomena and the study of emergent behavior from complex systems has a long history [12–14]. A large number of examples exist from surface friction or phase transitions to flocks of birds or schools of fish [15–18]. Emergent behavior is even used in an attempt to understand gravity and blackhole horizons [19–21]. In each case the macroscopic behavior of the system can be described, despite not fully understanding the complex interac-

tions of all the components in the system. The aim is to continue in this line of study and investigate the emergent laws that form in the control, stability, and evolutionary optimization of insect locomotion.

This thesis will start with a discussion of the behavior that the tiger beetle exhibits during experimentally recorded chase pursuits of its prey. In chapter 2 the movement of the body is analyzed and a control law for the orientation of the beetle is found that depends on the distance to the prey. This control law links the rotation rate of the body to the angle of misalignment towards the prey and its parameters are such that they minimize the time required to direct the body towards the prey. Chapter 3 will discuss the leg positioning at each step and examine how the stride is modulated based on the visual information. It turns out that different legs have different functions with the steering coming from the front legs and the propulsion provided by the hind legs.

The second part of this thesis concerns emergent behavior in the evolutionary process and in particular studies the effect of morphological adaptations on the flight of insects. The evolution of a species stems from the complicated interplay between the random genetic changes of each new generation and a variety of selective pressures that determine who survives [22]. From this complex system it can emerge that evolution seems to act purposefully to optimize certain traits [23–25]. The emergent behavior comes in the form of guiding principles which evolution naturally follows. It is those guiding principles that we will try to discover when studying morphological adaptations to insect flight.

Chapter 4 will focus on the first morphological feature, the wing hinge location on the fruit fly, and the effect it has on the flight performance and stability. This will be studied using a 3D insect flight simulator that allows for large para-

metric studies of the fly's morphology. The steady-state flight profile of the fly and its stability are determined using Floquet stability analysis on periodic orbits. It turns out that the wing hinge is positioned to maximize the vertical force generation independent of the wing stroke amplitude, giving the fly the largest range of possible flight velocities. This specific wing position is advantageous due to an antiresonance in the coupled wing-body system, where the lift and inertial torques nearly cancel each other out on the body.

The second morphological feature is covered in chapter 5, where reductions in the hind wing size are studied to model the evolutionary process that leads from four to two-winged insect flight. Dragonflies, who fly with a horizontal body, are some of the oldest known flying insects [26]. Later insects, such as mayflies or fruit flies, commonly fly with their body pitch up vertical [27]. The evolutionary process connecting the two flight styles will be studied by determining the changes to the flight kinematics and the effect on the power consumption. The results indicate that the transition to two-winged flight was likely a sudden development, which was only possible after a significant change to the front wing muscle.

Finally, chapter 6 covers the experiment I built to see if a human can learn to control insect flight. The aim was to combine the previous projects and study how control laws naturally develop when the brain has to deal with a novel task, for which in my case the human control of insect flight was very suitable. In the lab an infrared camera system is used to track a wing model and the provided motion is fed into the insect flight simulator. This allows a human to provide the wing motion and receive real-time visual feedback of its effect on the insect's flight. To test the system I attempted to maintain hovering as a fruit

fly and studied if it is possible to traverse a horizontal distance as a dragonfly. The initial results show that humans are able to control insect flight, but further study is needed to elucidate the exact nature of the laws through which this control is achieved.

CHAPTER 2

PREY PURSUIT BY TIGER BEETLES DEPENDS ON DISTANCE [1]

Visually guided pursuit behavior [9, 29–36] provides a rich experimental playground to examine connections between behavior and neural computations [37–42]. In spite of the increasingly sophisticated understanding in animal behavior and their neural systems, simple questions such as how animals measure distance or generally how they extract relevant information from the visual field do not have clear-cut answers [34, 43–46].

This chapter will examine the control of the tiger beetle chase behavior and focus on whether tiger beetles use distance information during their pursuit of prey. Tiger beetles are fast diurnal predators capable of chasing prey using closed-loop visual guidance [32]. Because their pursuit takes place in a two-dimensional plane, it provides a convenient system for behavioral analyses. The initial analysis of tiger beetle's pursuit dynamics elicited by a moving bead showed that the beetle uses a proportional control law in which the angular position of the prey in the beetle's visual field drives the beetle's angular velocity with a delay of half a stride period, about 28ms [9]. This suggested a physical interpretation of the observed control law: to turn toward its prey, the beetle on average exerts a sideways force proportional to the angular position of the prey measured a half stride earlier. The control gain is close to the critical value, $k = \frac{1}{\tau e}$, with τ being the time delay, further suggesting the beetle reorients itself toward the prey in the least amount of time without exciting oscillations [47].

The results presented here provide clear evidence that tiger beetles adjust their control gain based on distance to the prey. After its initiation, the beetle

[1] This work is reported in [28].

follows the prey with sub-critical gain. When the prey is within a radius of about 10cm, it increases its gain to a near-critical value, and when the prey is within a few strides, the beetle increases its gain again to catch the prey.

2.1 The proportional control law

First, the experiments and the control law analysis, on which this chapter is based, are summarized [9]. Pursuits of a prey dummy, a high-contrast black sphere of 4.5mm diameter glued to a nylon monofilament, by tiger beetles were filmed at 250 frames per second with 1024×1024 resolution using a high-speed video camera (Phantom v. 5.0, AMETEK, USA). The digital greyscale images were imported into Matlab (MathWorks, Natick, MA, USA) for analysis. The experiments were performed in a cylindrical arena (33 cm diameter, 18 cm tall). The walls were patterned alternately with black (4 mm) and white (12 mm) vertical stripes to provide contrast for the beetle moving through the arena. In total 6 different beetles were tested and each performed multiple chases, each beetle was around 13mm long. They were acclimatized to the arena for 10 min before the prey dummy was introduced by lowering it from above and moving it across the floor by hand. The positions and the orientations were extracted using a home-written algorithm that tracked white dots painted on the black beetle. Figure 2.1a shows the spatial patterns of the beetle and the prey during a typical case in the lab frame. The beetle is represented by a small rod with the head marked by a dot and the prey is depicted by an asterisk. The pattern shows that the beetle orients itself so that the prey is directly in front of it by aligning the body axis (solid line) with the line of sight to the prey (dashed line). The active orientation of the body is described by $\omega_B(t) = K\theta_e(t - \tau)$, where $\omega_B = \dot{\theta}_B$

is the body angular velocity, and θ_e prey's angular position relative to beetle's body-axis, see figure 2.1c for variable definitions. Figure 2.1d-e show that the correlation coefficient is maximal at $\tau = 28$ms, and the corresponding gain in the proportional control law is $K = 12.7\text{s}^{-1}$. As it has been noted previously, given a time delay of 28ms the gain value is close to the optimal value, $K = 1/e\tau \approx 13.1\text{s}^{-1}$.

Control of force and torque

To expand on the previous discussion the control of force and torque on the body can be studied. For the beetle to abide by the control law for ω_b it must provide a torque to rotate its body. The expectation is thus to find a similar control law governing the angular acceleration $\alpha_b = k_2\omega_e(t-\tau_2)$. This relationship is derived by taking the time derivative of the control law for ω_b. Figure 2.2a and c show this proportional control for α_b. The delay here is $\tau_2 = 24$ms, close to τ_1. The gain is slightly higher at $k_2 = 14.6\text{s}^{-1}$. These values for τ_2 and k_2 should be the same as for τ and K found in the previous section. The discrepancy is due to the increased noise that comes with taking an additional derivative, as can also be seen by the overall reduction in correlation coefficient in Figure 2.2a compared to Figure 2.1e. Despite this complication, the angular acceleration and thus torque is clearly modulated based on the error angle.

While torque control allows the beetle to rotate its body, a sideways force is needed to control its heading. The perpendicular acceleration on the body, denoted as $a_\perp$, causes the change in the heading by rotating the velocity vector v_b. The magnitude of the velocity can be changed by the parallel acceleration $a_\parallel$,

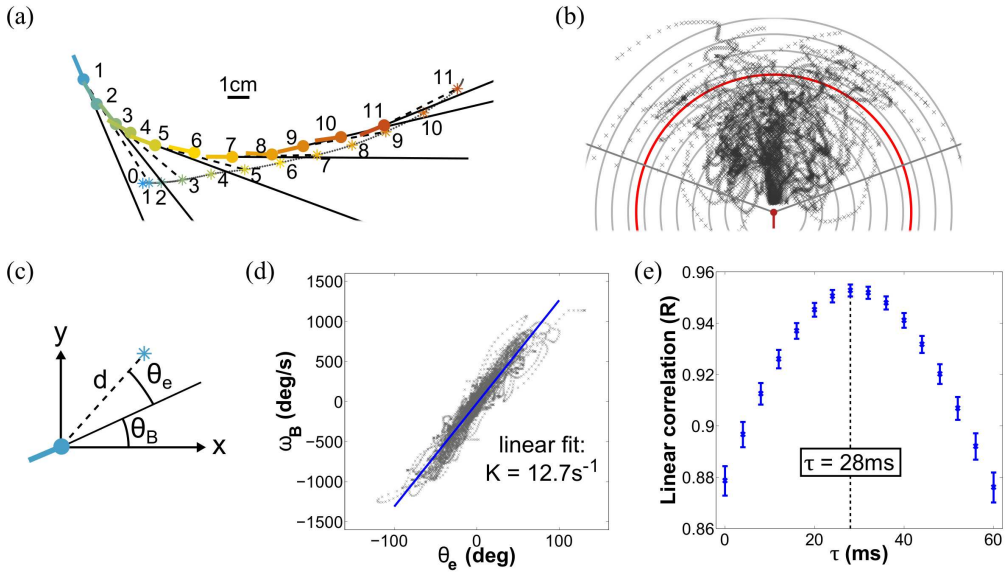

Figure 2.1: (a) Example of tiger beetle pursuit dynamics. The position of the beetle (rod) and the prey (asterisk) are shown at 56ms intervals, the walking gait period. During the chase the beetle reduces the angle between the body axis (solid line) with the line of sight to the prey (dashed line). (b) Prey location in the beetle's frame of reference for all recorded chases. The prey starts at error angles up to 70° and mostly stays within the arc defined by this angle. Circles at 1cm interval indicate equidistant points and the thick (red) circle indicates the critical distance. (c) Definition of the beetle variables. θ_B is the beetle's body angle measured in the lab-frame, θ_e is the prey's angular position relative to beetle's body axis and d is the distance to the prey. (d) The beetle's angular velocity as a function of the error angle supports the linear model $\omega_B = K\theta_e(t-\tau)$ with gain coefficient $K = 12.7\text{s}^{-1}$. (e) The linear correlation coefficient between ω_B and θ_e as a function of the time delay τ. The maximum correlation occurs at 28ms, indicating the beetle has a delay equal to half its walking gait period.

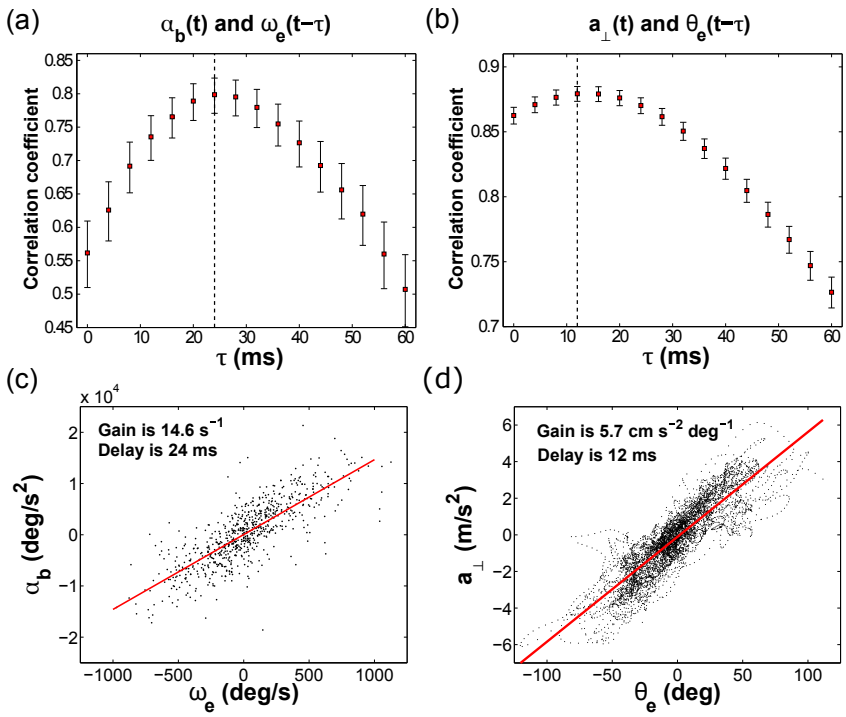

Figure 2.2: Two control models for the force and torque. (a-b) The linear correlation coefficient for each of the models. Dashed vertical line indicates highest correlation. a) The torque or angular acceleration model is $\alpha_b(t) = k_2\omega_e(t-\tau_2)$. The time delay is $\tau_2 = 24$ms and the gain is 14.6s^{-1}. b) The force or perpendicular accelaration model is $a_\perp(t) = k_3\theta_e(t-\tau_3)$ with the time delay $\tau_3 = 12$ms. (c-d) The fitted control model for each case. Note that taking the additional derivative increases the noise in the data in (c). The overall correlation coefficient in (a) is also lower than in (b). Black dots indicate recorded data for each frame. Red line is the line of best fit. The gain k for each model is indicated in the respective figure.

which is defined as the acceleration along the trajectory. Figure 2.2b and d show a third control law which governs the sideways acceleration $a_\perp(t) = k_3\theta_e(t-\tau_3)$. Interestingly the time delay here is short, at just $\tau_3 = 12$ms, indicating the heading is corrected before the body orientation. The gain is $k_3 = 5.7\text{cm s}^{-2}\ \text{deg}^{-1}$. Given that the control laws for the angular acceleration α and perpendicular acceleration $a_\perp$ have different time delays τ it seems probable that they are ac-

tuated by different mechanisms. The actuation of the force and torque will be studied in detail in the next chapter.

2.2 Distance dependent gain for the control law

Here we return to the original control law for the body orientation. The first clue that the proportional gain K depends on the distance can be seen in figure 2.1a when the beetle is close to the prey. After time step 8, the beetle is seen to overshoot in its corrections in the error angle, suggesting an increased gain as the beetle gets closer to the prey. This observation led to a systematical examination of the distance-dependence of the control gain. This analysis reveals two transitions in the gain; one at $d \approx 10$cm in addition to the transition at short-distance, $d \approx 2$cm (figure 2.3).

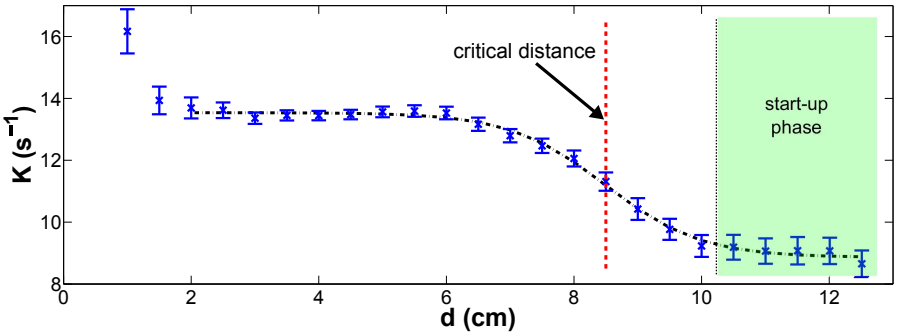

Figure 2.3: The gain coefficient in the proportional control as a function of distance. Two regions of changing gain are visible, one below 2cm and one between 6 and 10cm. In between those the gain value is near the critical value of $13.1s^{-1}$ for $\tau = 28$ms. The results are generated by grouping all data based on the beetle-prey distance in bins with a width of 2cm centered 5mm apart.

To examine the distance dependence of the delay $\tau(d)$ and gain $K(d)$, the same analysis as described for figure 2.1d-e is applied to a series of data subsets,

where each subset is binned according to the distance to the prey. The time delay τ is nearly constant at 28 ± 4ms over the range of observed distance, from d is 1 to 12.5cm. Therefore the time delay is fixed at τ = 28ms for the remainder of the analysis.

The main result is summarized in figure 2.3, which shows the dependence of the gain on distance. When the tiger beetle is far away from the prey, beyond 10cm, it uses the lower gain of $K = 9.0\text{s}^{-1}$. Below 10cm, the gain increases with decreasing distance and reaches a near-critical value $K = 13.5\text{s}^{-1}$ at $d \approx 6$cm. $K(d)$ can be well fitted by a hyperbolic tangent function between $d = 2$cm and $d = 12$cm, with the middle of the transition occurring at the critical distance $d^* = 8.5$cm. At small distances below 2cm, when the prey is within reach, the beetle increases its gain sharply to catch the prey.

The next question is whether the distance is a direct cause for the change in K, as opposed to an indirect cause via other intermediate variables. Relevant kinematic variables in the system are displayed as a function of the distance in figure 2.4a-c. At $d \geq 10$cm the beetle increases its velocity, v_B, to initiate the chase. In contrast the beetle's angular velocity, ω_B, initially decreases as v_B increases. However, note that over the range 6-10cm, where the transition in gain occurs, both of these quantities are nearly constant while $K(d)$ increases. It is therefore unlikely that they are the cause for the observed gain increase. Interestingly the combination of the velocity and angular velocity leads to a nearly constant sideways acceleration, $a_{\perp B} = v_B\omega_B$ (figure 2.4c). This suggests the chases are constrained by the maximal sideways acceleration of the beetle [9].

One can further ask whether the increase in gain might be correlated to the

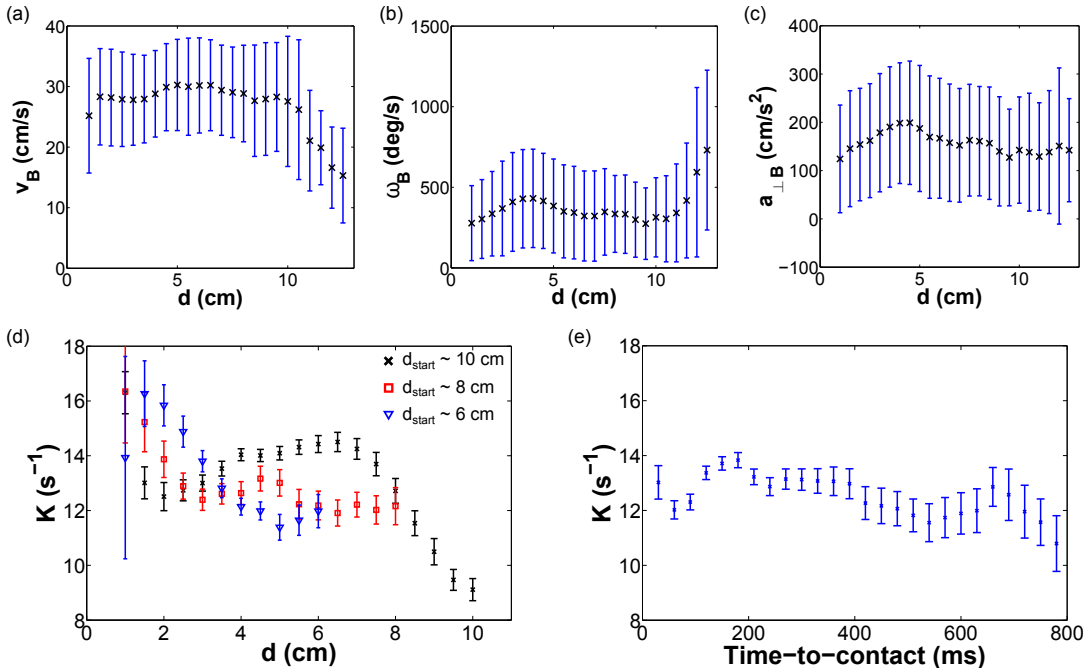

Figure 2.4: (a-c) Distance dependence of the absolute value of the beetle velocity, beetle angular velocity and beetle sideways acceleration respectively. Each is showing the mean value and standard deviation of all measurements, without removing the stride oscillations, within the same bins as in 2.3. The velocity and angular velocity of the beetle show a start-up phase beyond $d \approx 10$cm, however over the distance between 6 and 10cm, the gain transition region, both variables are approximately constant. In contrast to this, $a_{\perp B} = v_B \omega_B$ is roughly constant over the full range of distances, suggesting that the beetle is using a constant sideways force to reorient its body [9]. (d) Recreating of figure 2.3 using only the chases that started at a beetle-prey distance of around 6, 8 or 10cm. Notice that for the 10cm start distance the double transition is at the same location. For the 6 and 8cm start distance data there is no double transition. This indicates that the chase start-up phase does not cause the transition in K. (e) The gain coefficient in the proportional control as a function of time-to-contact (TTC). The gain fluctuates around the average value of $K = 12.7\text{s}^{-1}$, but there is no sharp transition based on TTC. This implies the beetle does not use TTC to modulate its proportional gain.

initial start-up phase, where the beetle accelerates. To exclude the initial phase, chases that start with a beetle-prey distance of 6, 8 or 10cm (±1cm) are selected (figure 2.4d). The 10cm data shows the gain transition occurring around the same d^*. The chases that start at 6 and 8cm bypass the lower gain of $K = 9.0\text{s}^{-1}$, but start directly with a higher gain. This suggests that the gain increase is not due to a start-up phase.

Finally, another potential candidate for the cause of increase in K is time-to-capture (TTC), a quantity that has been studied in the control of escape behavior [48–53]. Assuming a constant approach velocity, the TTC and the distance would be proportional to each other. As a result, a gain dependence on TTC can be wrongfully interpreted as a dependence on distance. To differentiate these two scenarios, the data is binned according to TTC. Here TTC is computed as the beetle-prey distance divided by its time-derivative (figure 2.4e). The figure shows that the gain does not depend on TTC, and in particular, there is no sharp increase at the small distance, where TTC would be expected to play a role.

All of these observations suggest that the distance to the prey is the direct cause for the change of the control gain. This implies the tiger beetle must have a mechanism by which it can extract distance information from the visual cues it receives.

2.3 Discussion of possible methods for distance detection

Insects use a variety of visual cues for distance detection [54]. Many studies have postulated mechanisms for distance detection in a variety of insects [55–60]. Examples include the peering motion used by locusts [61], the long range

distance detection used by honeybees [58], and the head movements used by dragonflies to determine the apparent size of a moving prey [46]. In the case of tiger beetle larvae it was shown that they possess a distance-sensitive visual interneuron [62]. It thus seems plausible that the tiger beetle can determine the distance to the prey using visual cues.

Although it will require further experiments to tease out the means by which tiger beetles detect the distance to their prey, I can at least examine the predictions from different methods and compare with the data. For this, two candidate theories will be analyzed. Each one is used by some insects for distance measurements. The first is based on motion parallax [61] and the second on the elevation angle of the prey [63].

Motion Parallax

Like many other insects, tiger beetle vision is monocular, as the visual fields of their two eyes do not have a large overlap [60,64]. However, the beetle can move its head back and forth to simulate binocular vision to detect distance, a strategy known as motion parallax [55,57,61,65]. The distance d can be measured by the amplitude of the side-to-side motion of the observer A and the change in the angular position α: $d = A/\tan(\alpha/2)$ (figure 2.5b). Recent work further suggests that insects have developed specific movement patterns to facilitate distance measurement through motion parallax [38,40,59,66].

The simple formula above applies to a stationary prey and an observer moving only perpendicular to the line of sight, whereas in a pursuit both are moving freely. This raises two interesting questions: does the beetle measure and make

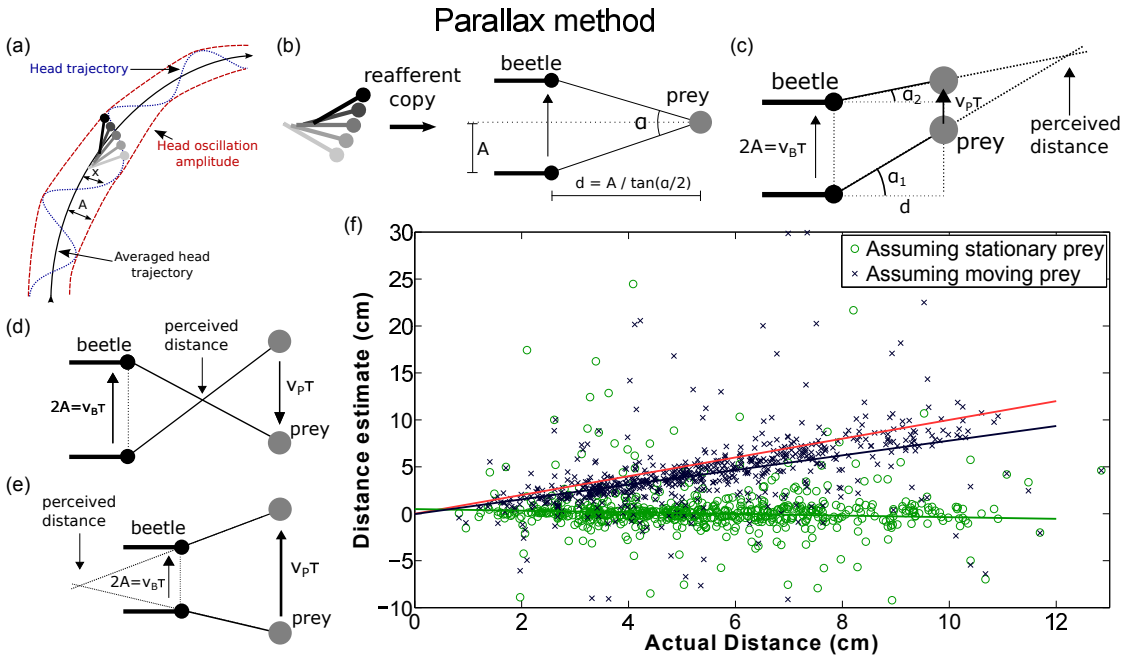

Figure 2.5: *Motion parallax method*. (a) Sketch of a head trajectory during a chase. Due to the walking gait the head makes a natural sway. The head trajectory can be described as an oscillation on the averaged trajectory. (b) Sketch of the parallax method for a stationary prey. Assuming the beetle can negate the effect of its own motion it would see the prey at different angles during one head oscillation. The angle α can easily be used to compute a distance to the prey. (c) Sketch of the motion parallax method in the case where the prey is moving. The estimated distance, which assumes a stationary prey, needs to be corrected to obtain the actual distance d.(d) Sketch of a case where the estimated distance is very short. (e) Sketch of a case where the estimated distance is negative. (f) Distance computed from measured angles α using the recorded image data. Green circles are used to indicate the distance based on the stationary prey assumption and black crosses for the corrected distance assuming a moving prey. Trend lines, in matching colors, are fits through the data. Red line indicates a perfect measurement.

use of prey's velocity, and does it subtract its own velocity? For the analysis here, two possibilities are considered. In the first case, the beetle does not make use of prey's velocity. In the second case, the beetle can measure the sideways velocity of the prey and takes it into account for the distance measurement. Both cases also assume that the beetle can correct for its own body rotation.

To work out the distance detection for a moving prey, note the geometry in figure 2.5c),

$$v_B T = v_P T + d \tan \alpha_1 - d \tan \alpha_2 \tag{2.1}$$

where v_B and v_P are beetle and prey velocities, respectively, and T is the time of a half stride. In the case when $\Delta\alpha_{12} = \alpha_1 - \alpha_2$ is small,

$$d \approx \frac{2A}{\Delta\alpha_{12}} \left(1 - \frac{v_P}{v_B}\right) \tag{2.2}$$

Note that when $v_P = 0$, it reduces to the formula for the stationary prey case, as expected. The correction due to prey movement appears in the form of $\frac{v_P}{v_B}$. If the beetle uses this distance estimate, it needs to estimate the prey's velocity relative to the beetle's.

In figure 2.5f, the two distance estimates are compared with the data. The formula that takes into account the sideways prey velocity gives a reasonable estimate of the actual distance, while the formula assuming a stationary prey clearly fails. The latter over-predicts the distance if the prey is slower and moves in the same direction as the beetle (figure 2.5c), while under-predicts if the prey moves in the opposite direction as the beetle (figure 2.5d). In cases where the prey moves faster than the beetle, the formula can even give negative distance (figure 2.5e). These negative measurements lead to the conclusion that in order to measure the distance using motion parallax, the beetle must take into account

the prey's velocity, and more specifically, it needs to measure the velocity ratio v_P/v_B.

Distance based on vertical angle

Another potential method that tiger beetles can use for distance detection is to measure the elevation angle of the prey (figure 2.6) [63]. This elevation method exploits the idea that the elevation, or vertical position, of the prey on the visual field is directly related to the distance. This simple method has a few advantages. The visual angle can be readily determined by a compound eye. By measuring the angles both to the bottom (β) and top of prey (γ), the beetle can estimate both the distance to the prey (d) as well as the size of the prey (L). This distance measurement is less noisy compared to motion parallax, because the prey's sideways stride oscillation does not affect the elevation angle.

In order to find out whether the distance given by this method can be used during the beetle's pursuit, the accuracy of such measurements is calculated. The error in the distance measurement ϵ_d is given by the angular resolution of the eye, which is associated with the finite size of the ommatidia. The error increases with the distance. At a distance $d = 8.5$cm, where the transition occurs, the error is around 20%, or 1.7cm, which, interestingly, coincides with the width of the transition region seen in $K(d)$. A similar calculation also gives the error associated with the estimated size of the prey, ϵ_L. At $d = 15$cm, $\epsilon_d \approx 80 - 120\%$. This implies that it would not be wise for the beetle to chase a prey, as it would run the risk of chasing objects larger than its own sizes, including predators.

The error calculations are based on the geometry shown in figure 2.6: $d =$

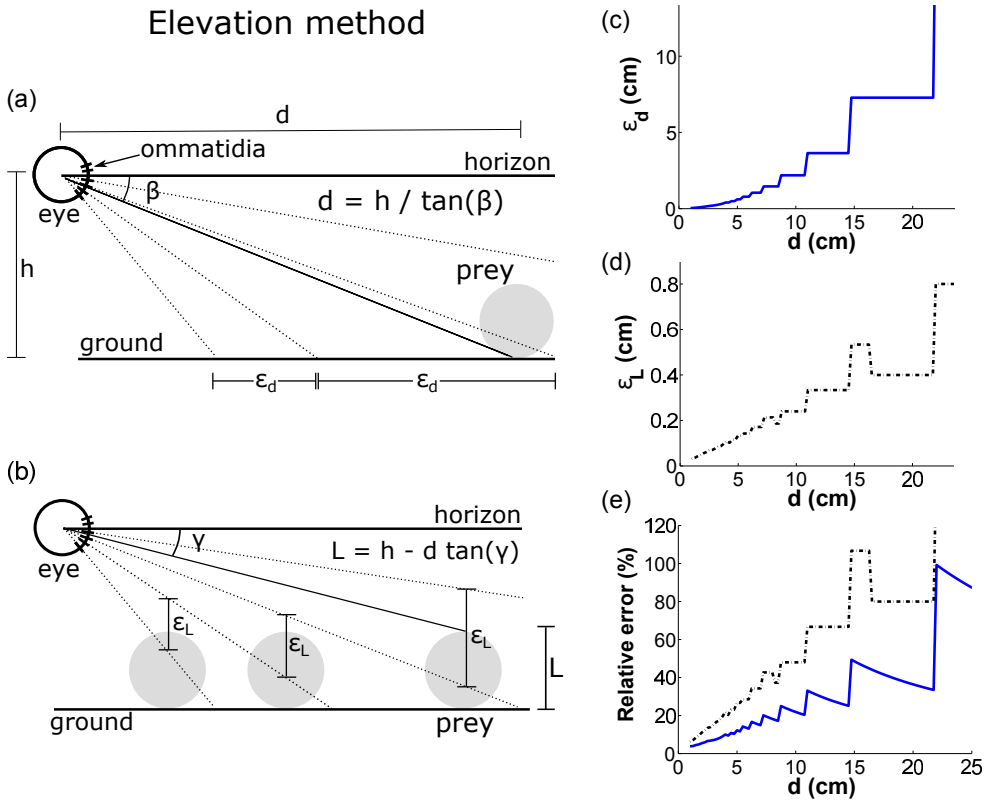

Figure 2.6: *Elevation method*. (a) Sketch of the elevation method for distance measurement. Knowing its own eye height h, the beetle can measure the distance to the prey by determining the angle β. Due to the finite resolution of the beetle eye this measurement leads to measurement error ϵ_d. Dashed lines represent the lines of sight of ommatidia. (b) Sketch of the elevation method for size measurement. Once the distance is known, measuring the angle γ allows the size L of the prey to be determined. Again the finite resolution of the eye leads to measurement errors in the size ϵ_L. (c-d) The estimated absolute error on distance and size measurement as a function of distance to the prey. The estimates were computed using an interommaditial angle of 1.05°. (e) Relative error for both distance and size as a function of distance. The graphs show a large number of big jumps, but those are artifacts of the simplistic model, a more realistic model allowing for partial activation of ommatidia would smooth those out and possibly lower the uncertainty slightly.

$h/\tan(\beta)$, where h is the beetle's height, and β is the angle downward to the ground where the prey is. If the beetle further measures the angle γ from its eye to the top of the prey it can also determines the size of the prey, $L = h - d\tan(\gamma)$ (figure 2.6b). The uncertainty in distance is due to the angular resolution for measuring β,

$$\epsilon_d = d_{max} - d_{min} = \frac{h}{\tan(\theta_{min} \cdot \lfloor \frac{\beta}{\theta_{min}} \rfloor)} - \frac{h}{\tan(\theta_{min} \cdot \lceil \frac{\beta}{\theta_{min}} \rceil)} \tag{2.3}$$

For the angular resolution, the value of the minimum vertical interommatidial angle is $\theta_{min} = 1.05^\circ$, and the beetle height h is 8mm [63]. The brackets in the first and second term in equation 2.3 indicate rounding down and up to the next integer respectively. The uncertainty in size ϵ_L is based on the same idea, but depends on β, through d_{min} and d_{max}, and on γ:

$$\epsilon_L = L_{max} - L_{min} = d_{min}\tan(\theta_{min} \cdot \lfloor \frac{\gamma}{\theta_{min}} \rfloor) - d_{max}\tan(\theta_{min} \cdot \lceil \frac{\gamma}{\theta_{min}} \rceil). \tag{2.4}$$

2.4 Summary

The analysis here shows that tiger beetles adjust the gain in their control law for the body orientation. The gain depends on the distance instead of other variables. The transitions in gain occur at two distances, one near capture, and the other at a distance of about 8.5cm. Two additional control laws, one for the sideways force and one for the torque, were described. Furthermore, two potential methods for distance detection by the tiger beetle were analyzed: motion parallax and elevation angle. In order for motion parallax to explain the data, the beetle needs to correct for the ratio of the prey's velocity relative to its own. How this would be achieved is an open question. The method based on elevation angle can simultaneously detect the distance and the prey's size. The

accuracy of distance detection depends on the beetle's visual acuity. The analysis suggests an explanation for the typical distance at which the beetle initiates its chase. Beyond this distance the beetle would run the risk of chasing after a large predator due to the error in determining the size of the moving object. Given these results it seems likely that a distance dependence in the pursuit of prey may also be present in other insects which use visually guided control laws. Hopefully this work will stimulate further investigations in quantifying the role of distance detection in animal pursuit dynamics.

CHAPTER 3

VISUAL CUES MODULATE LEG PLACEMENT OF THE TIGER BEETLE

The control law for the beetle's chasing behavior as described in the previous chapter provides a picture on long time scales. Given that the tiger beetle walks with a tripod gait, the neural control likely modulates each step individually to implement these control laws. The control then only appears smooth over time scales that are long compared to a single stride. In other insects and animals, legged locomotion is known to comprise of a centrally generated motor pattern with variations that result from mechanical and sensory feedback [67–72]. Therefore a natural hypothesis is that the beetle implements its chasing behavior by adapting each tripod, or perhaps even each leg, based on the visual cues from the prey. In the literature it remains largely unknown how the step-to-step variability of the gait is affected by visual cues. Therefore this chapter can provide insight into this issue and show if and how the tiger beetle's gait is modulated by the visual information received about the prey.

To analyze the beetle gait the images from the previously recorded chases are re-examined and each of the feet of the tiger beetle is tracked. The results indicate that the tiger beetle's front feet are most strongly controlled by the visual information. The middle legs appear to be used as an anchor around which the body can rotate, especially during sharp turns. This suggests the middle legs mainly produce centripetal force during turning. The results hint that the outside legs are the main producers of the torque required to rotate the body axis, while the inner legs steer the trajectory by regulating the sideways acceleration. The hind leg is completely independent of the visual cues, which suggest they are not under active control.

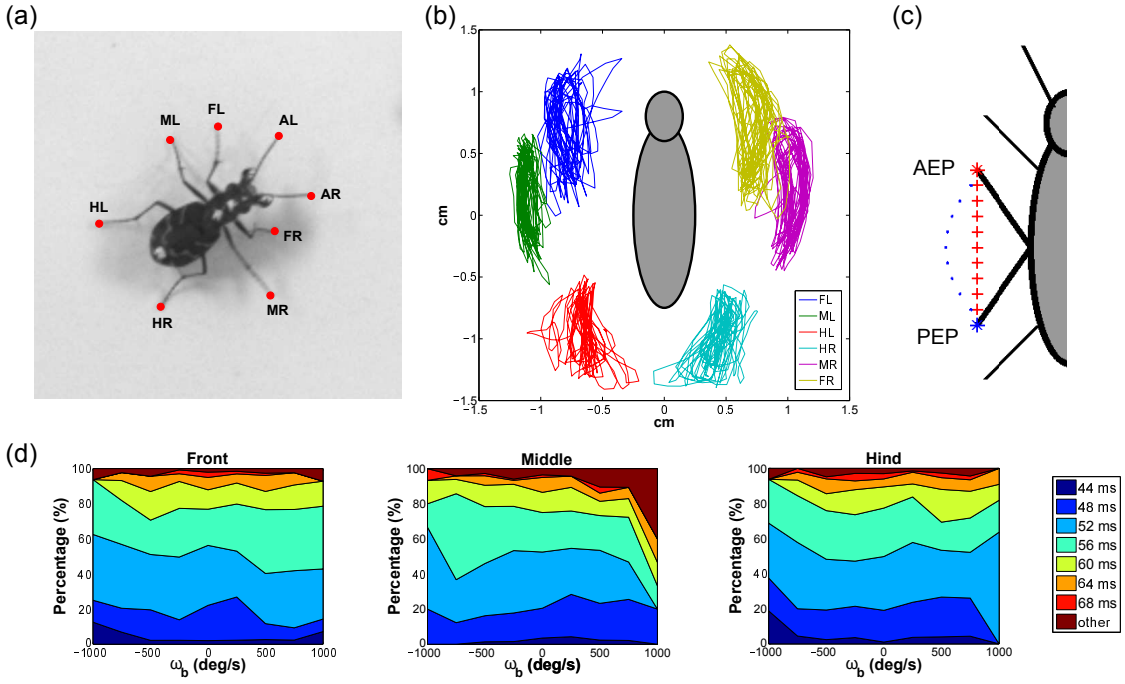

Figure 3.1: a) Naming convention for the legs of the tiger beetle. A = antenna, F = front, M = middle, H = hind, L = left and R = right. b) Tracking data for each of the feet during one example chase shown in the beetle's frame of reference. Grey sketch represents the beetle body with head indicated. c) Definition of anterior (AEP) and posterior (PEP) extremum position, here indicated for the left middle leg. During forward movement the leg is placed at the most anterior position, red star, after which it moves down the body during the stance phase (red pluses). The leg is lifted at the most posterior position, blue star, and then moved forward with respect to the body during the step phase (blue dots). (d) The gait cycle duration as a function of ω_b. Cycle duration is measured as time between two subsequent AEPs. Negative ω_b indicates turning towards the leg. It shows there is some variety in the cycle duration, but for all legs that variation is independent of the turning rate of the beetle.

3.1 Rhythmic stepping pattern

The previous discussed control laws for the torque and force must be implemented on the short time scale of the individual strides. In order to investigate that, the images from the tiger beetle chases are analyzed to track the individual feet. This analysis shows that the tiger beetle maintains a triangle between its feet with the placement of each tripod step.

The legs and antennae of the tiger beetle during its chase are tracked from the recorded greyscale images. Using the corner detection algorithm from Matlab the feet of the beetle can be located. A simple linear position predictor then allows to reliably connect the detected feet locations in adjacent video frames. Incorrectly marked feet are identified and corrected by the human eye.

The six legs of the beetle are labelled counterclockwise from the body axis, which the naming convention shown in figure 3.1a. The antennae (AL and AR) are ignored for this research. In figure 3.1b the result of the feet tracking is shown for an example chase. It shows that the front and middle feet are relatively close together. In fact, the middle leg is sometimes lifted over the front leg, after which the front leg has to be pulled out from under the middle leg to bring it forward again. The hind leg is further back and is not restricted by any nearby legs.

During each step two locations are of particular interest, namely when the leg is placed on the ground and when it is lifted off. These two locations are known as the AEP (anterior extremum position) and PEP (posterior extremum position) respectively [73]. In figure 3.1c the AEP and PEP are indicated for the middle leg in the beetle's frame of reference. In the body frame the AEP is the

furthest anterior point the leg reaches during a single step after which the leg moves down along the body axis, because it is placed on the ground. When the leg reaches its most posterior point, the PEP, it is lifted off the ground and starts moving up along the body axis again.

Tiger beetle's run using a tripod gait during straight movement and the gait cycle takes 56ms on average [9]. The temporal data confirms, in figure 3.1d, that this is also the case during turning. The graph shows the number of gait cycles of a given duration as percentage of the total number of gait cycles at the given ω_b. Here the gait duration is defined as the time between two AEPs. There is variation in the duration at all turning rates, but on average for all legs and all turning rates a full gait cycle takes 52-56ms. This indicates the stepping frequency is not influenced by the turning rate of the body.

Besides the temporal information, the tracking algorithm also provides the spacial positioning of each leg during the chase. Figure 3.2-3.3 show two examples of the feet pattern of the beetle during a chase. The blue triangles are the position of the HL, MR and FL feet at the AEP of the HL leg. Similarly the red dashed triangles are the positions of the HR, ML and FR feet at the AEP of the HR leg. Within each triangle the stick indicates the beetle's body orientation. The persistent pattern of triangles indicates the tripod gait is consistently executed throughout the chase and its various turns.

The insets of figure 3.2-3.3 support a repeating gait pattern, but also show that the triangular stepping pattern is not completely constant. The feet triangles are characterized using two angles and the triangle area. The angles are measured at the hind and middle leg. All these characteristics fluctuate by about 15% of the value at the start of the chase.

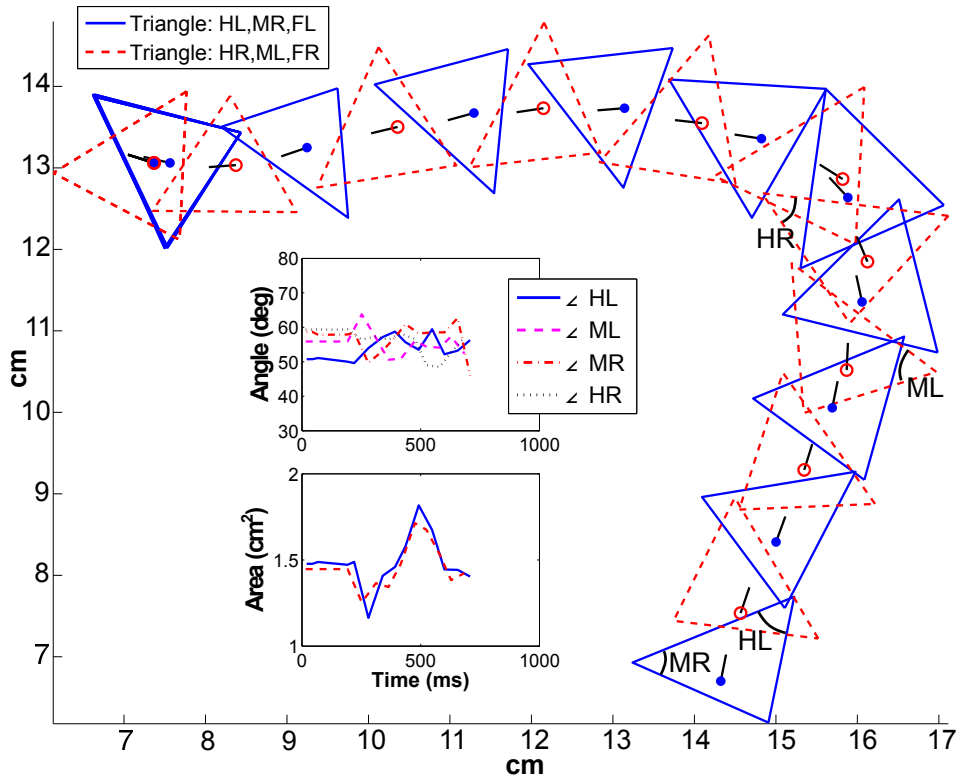

Figure 3.2: Example of the step pattern recorded during a chase. Triangles shown are at hind leg AEP, blue full line for the left hind leg, red dotted line for the right hind leg. Insets show the angles and area of the triangles during the chase. They indicate the beetle allows some fluctuations in its triangular stepping pattern.

These results suggest that the neural system of the tiger beetle can keep the overall positioning and timing characteristics of the leg motions fixed to a high degree. However, some variation in the pattern is visible and now we will study how those small adjustments are determined by the visual information.

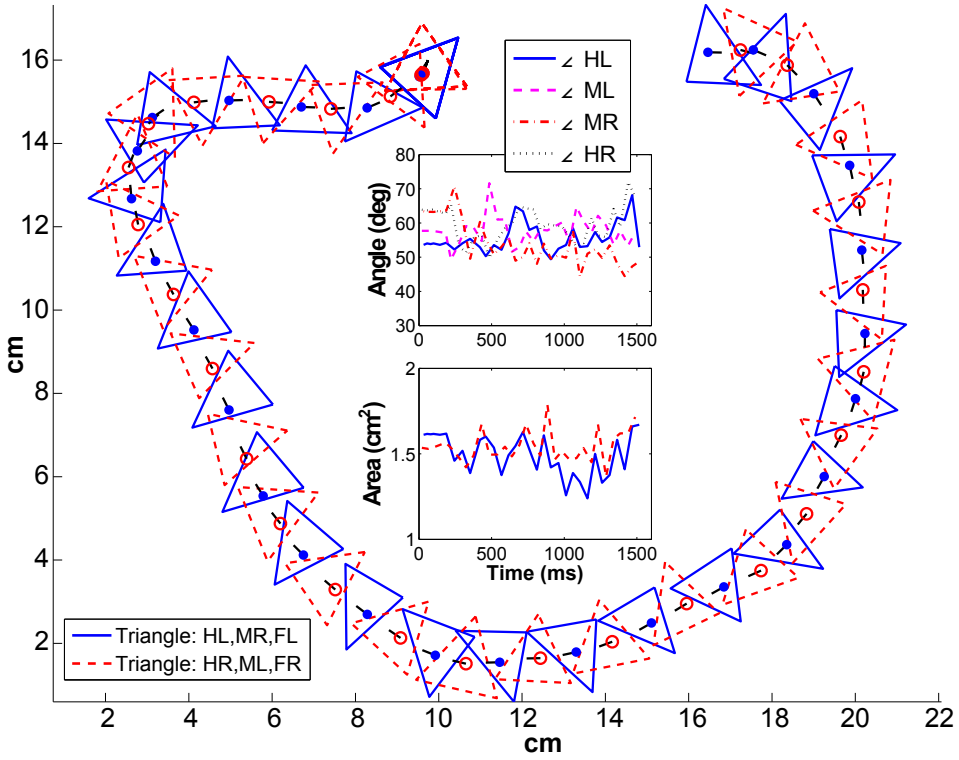

Figure 3.3: Second example of the step pattern recorded during chase. This chase had a significant longer duration. The triangle stance is maintained during sharp turns and straights. One can clearly see the triangle separate more (faster running) during straight segments.

3.2 Leg position dependence on visual information

In this section we investigate how the visual information and the beetle's own movement change the leg placement and step size. The body control laws indicate that the error angle θ_e is the important parameter for the beetle's control and it thus seems likely that the AEP will depend on θ_e. Figure 3.4a shows the AEP of each of the legs colored by the value of θ_e 28ms before placement occurred. The middle and front legs display a smooth color gradient, with the direction of the gradient inverted between left and right. The hind leg shows no such gradient and has a very localized AEP irrespective of θ_e.

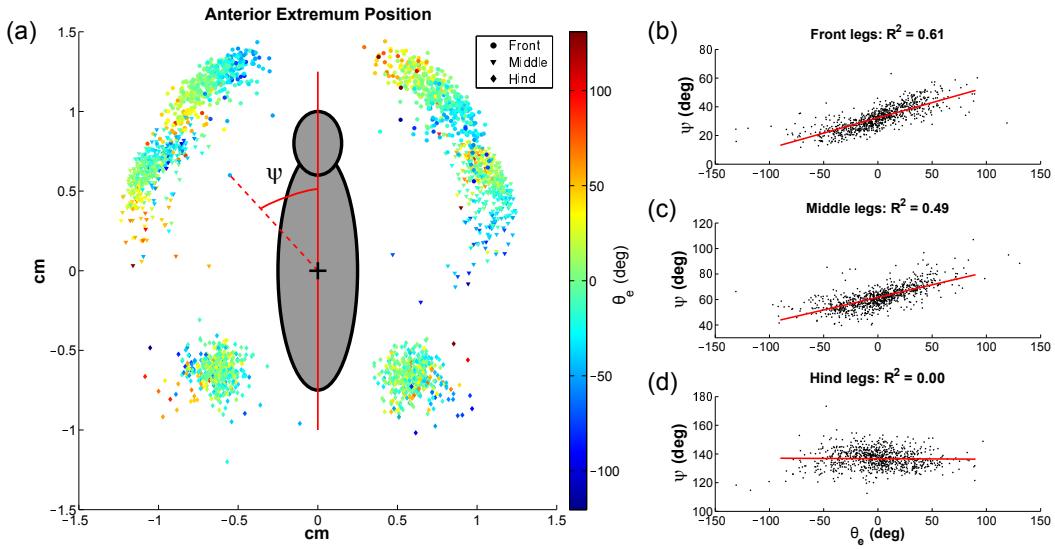

Figure 3.4: a) The AEP in the beetle body frame colored by the value of θ_e 28ms before placement occurred. The front and middle legs show a smooth color gradient, indicating a relationship between the placement position and θ_e. In contrast the hind legs have a very localized AEP. To formalize these results, I define the foot angle ψ as the angle of the location of the foot with respect to the body axis. (b-d) The foot angle ψ as a function of the error angle θ_e. The data is from the left and right leg together, where the right leg is mirrored to the left and has its θ_e-scale inverted.

These observations can be quantified by defining a foot angle ψ as the angle of the foot left of the body axis. The right legs are mirrored to the left by flipping the minus sign on both the x-coordinate and θ_e value. Figure 3.4b-d show the relationship between the foot angle ψ and the error angle θ_e for the front, middle and hind leg respectively. The R^2 values confirm the previous observations. The error angle best determines the AEP of the front leg, $R^2 = 0.61$. The error angle also has predictive power for the AEP of the middle leg, $R^2 = 0.49$. However, the AEP of the hind leg is not influenced by θ_e at all, $R^2 = 0.00$.

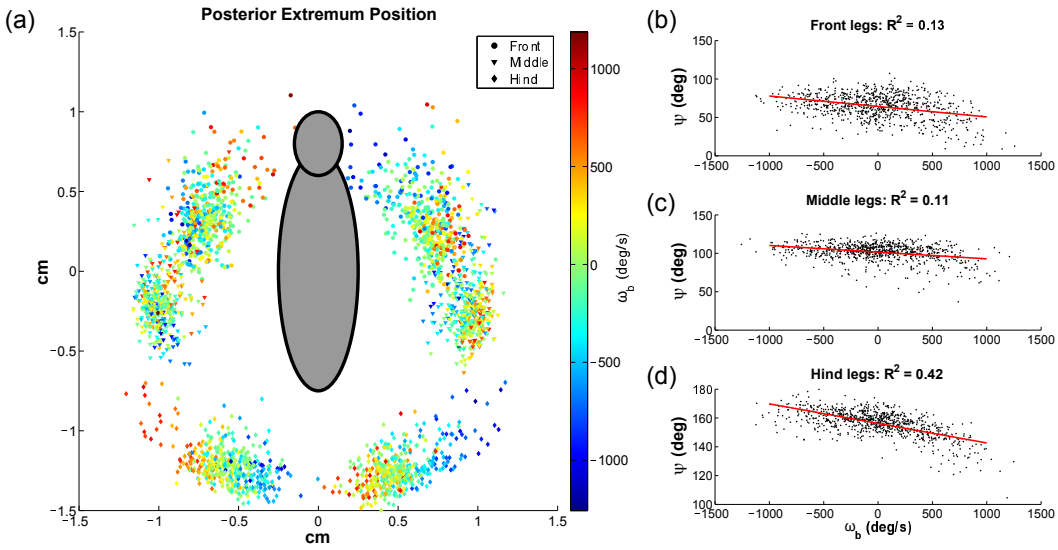

Figure 3.5: a) The PEP in the beetle body frame colored by the value of ω_b without a delay. The hind legs show a smooth color gradient while the front and middle legs are more complicated. (b-d) The foot angle ψ of the PEP as a function of ω_b formalizes visual indications. The R^2 values indicate the lift off position of the hind leg is better determined by ω_b than lift off positions of the front or middle leg.

While the AEP, as the leg placement position, provides insight into the active coordination among the legs, the PEP, as the lift-off position of the leg, provides insight into the passive effects on the legs. Figure 3.5a shows the PEP of each of the beetle's legs colored by ω_b. The front and middle legs show a complicated color pattern. There is a hint of a pattern in the dark red and dark blue points, i.e. most extreme θ_e values, but overall a clear structure seems to be missing. The hind legs on the other hand show a continuous color gradient.

Figure 3.5b-d shows the foot angle ψ at the PEP as a function of ω_b. This confirms the previous qualitative observations. The front and middle legs have a small coefficient of determination, $R^2 = 0.13$ and $R^2 = 0.11$ respectively. The

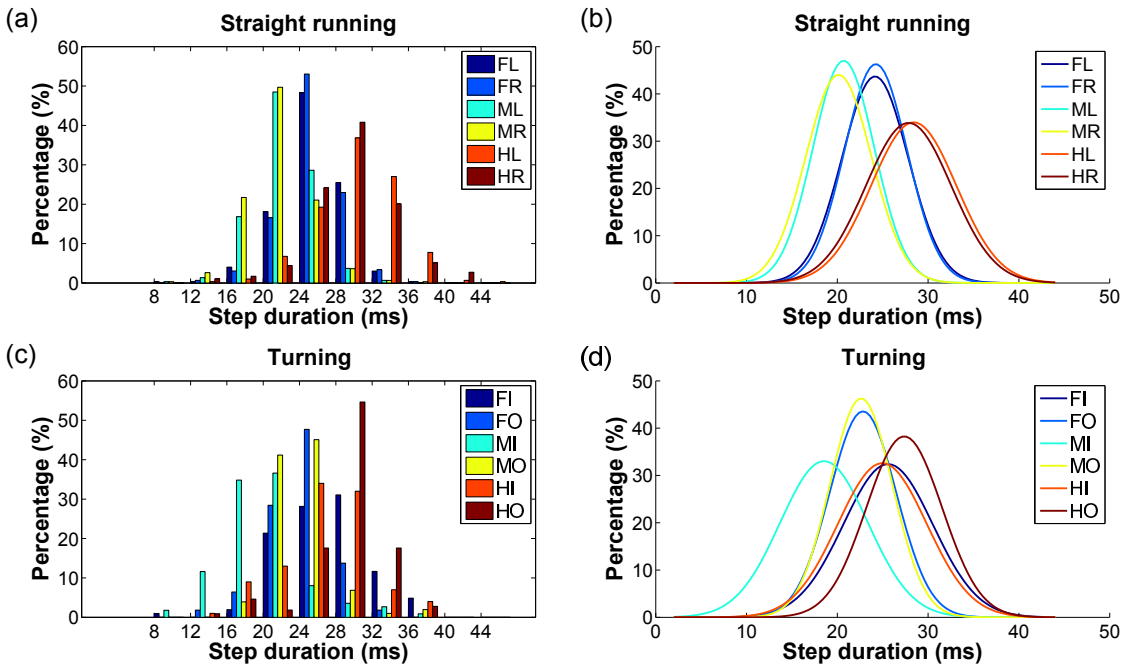

Figure 3.6: Distribution of step duration. Step duration is measured as the time between the PEP and the subsequent AEP. (a-b) Percentage of the total steps during straight running, $|\omega_b| < 500$deg/s. a) The discrete distribution for each of the legs of the beetle. The bin size is 4ms, corresponding to the frame rate of the recording. b) The fitted normal distributions to the distributions in a). We can see that the front, middle and hind leg all show different distribution means. (c-d) The same graphs for periods of turning, $|\omega_b| > 500$deg/s. For binning and coloring the data is now separated in inner (I) or outer (O) legs during the turn. We observe that the inner middle leg has a shorter mean step duration. In addition the outer front and middle take similar steps, just as the inner front and hind leg do. T-tests comparing the mean of the distributions at $p < 0.01$ level match all visual observations, see the text for details.

PEP of the hind legs on the other hand can be predicted relatively well by ω_b with $R^2 = 0.42$. The results for the variation in the AEP and PEP shown concern the position variation and only look at the period that the leg is on the ground.

Now we will look at the part of the gait cycle where the leg is airborne.

Figure 3.6 shows the distribution of the duration of the beetle's steps, which is measured as the time between a PEP and the next AEP. The graph compares the distributions during straight running, $|\omega_b| < 500\text{deg/s}$, and during turning behavior $|\omega_b| > 500\text{deg/s}$. Given the 250 Hz frame rate of the camera, the distributions are naturally discrete with 4ms bins. Figure 3.6b and d show fitted normal distributions to the discrete distribution to facilitate visual comparisons.

Note that the front, middle and hind legs all have different step duration means. The front legs take steps of 24ms, the middle legs 20ms and the hind legs 28ms on average. These results are statistically confirmed by t-test comparing the front, middle and hind step distributions, which all have different mean at $p < 0.01$ level. During turning, figure 3.6d, a large number of changes occur. The inner middle leg reduces its average step duration to 18ms ($p = 0.011$), while the outer middle leg increases its average duration to 22ms ($p < 0.01$). The average duration of a step by the outer front leg decreases ($p < 0.01$) and now takes the same time as for the outer middle leg, 22ms. At the same time the inner front and hind leg respectively increase and decrease the step duration, both at $p < 0.01$ compared to straight running. They pair up and take steps of 25ms on average. Finally the outer hind leg is not affected and still takes steps of 28ms on average.

Changing only the duration of steps on the inner and outer side of a turn would not be enough to rotate the body. There have to be changes in the distance travelled by the legs during a step as well. Figure 3.7 shows the step distance and its relation to ω_b for the front, middle and hind leg each. The minus sign on the ω_b value for the right leg was flipped before plotting, so that positive ω_b indicates turning the body away from the leg. The distribution of

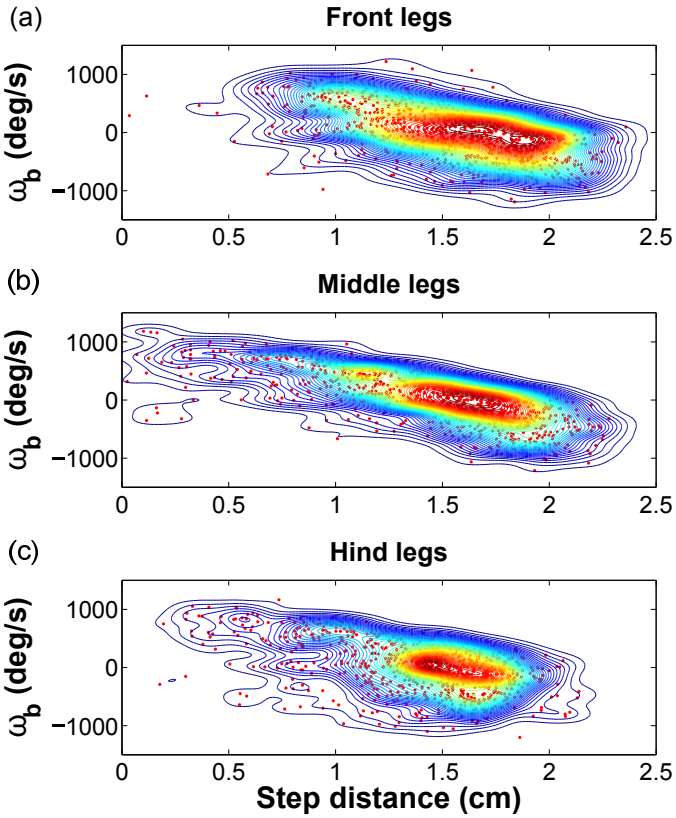

Figure 3.7: Step distance related to the angular body velocity ω_b. Step distance is measured as the spacial separation of a PEP and the next AEP. (a-c) Red dots indicate the data as recorded for each individual step. Left and right leg data is grouped together by mirroring ω_b for the right leg. The contour plot shows the density determined using kernel density estimation. Red is high probability, blue is low probability. a) The front legs always take steps of at least 0.5cm. b) The distribution of middle legs steps is the most elongated and goes all the way down near zero distance steps. c) The distribution for the hind legs seems to be more localized and is limited to step above 0.3cm. These graphs suggest that for sharp turns the beetle is rotating around a point near the inner middle foot.

points is smoothed using a kernel density estimate and the contour plot shows the density function.

Figure 3.7 corroborates the results from figure 3.6. The leg that can decrease its step distance the most is the middle leg, which matches with the observation that the inner middle leg reduces its step duration. The hind leg can decrease its step distance, but always makes steps larger than 3mm. This corresponds to the observation that the step duration for the inner hind leg was decreasing, but still significantly larger than for the inner middle leg even for sharp turns. Finally the front leg is restricted to steps above 5mm and also makes the largest steps of any leg. This inability for small steps matches with the inability for short steps that was observed before.

Taken together figure 3.4-3.7 show there is structure in the variation of the step pattern. In the next section, we will put all the results together and provide a simple picture that can explain the beetle's chase behavior.

3.3 Leg actuation and control law

This section puts together all the previous results and explains how the beetle could actuate its legs during a chase. First, we will look at the fairly consistent triangle formation for each of the tripod steps of the beetle. Afterwards the focus will be on the variations in the stepping pattern and each individual leg.

The beetle might vary the position, timing, and amount of force of each leg individually. The results obtained from the data of the feet movement provide insight into only the first two, position and timing. Measurements of the forces

of each individual leg is possible, but requires a different experimental setup [74]. However, information on the positioning and timing of the legs does allow for the formulation of hypotheses on what the forces on each leg are likely to be.

Consistent gait cycle

The gait cycle of the tiger beetle during straight running was quantified in [9]. The beetle uses an alternating tripod gait, where one tripod consists of the legs FL, MR and HL and the other of the legs FR, ML and HR. A full gait cycle takes on average 56ms. The results here confirm that this description is also valid for turning behavior. Both the temporal, figure 3.1d, and the spacial structure, Fig3.2-3.3, of the gait are well regulated throughout the chase. The full gait cycle takes 52-56ms on average for all legs and all turning rates. In addition the positioning of the legs maintains a regular triangular shape even during sharp turns.

The tiger beetle stepping pattern seems to closely resemble the gait of ants [75], who also maintain their tripod stance through turns. The distribution of step frequencies remains largely the same between the inner and outer legs during a turn, see figure 3.1d, ruling out that frequency modulations elicit the turning behavior [76, 77]. This leaves one other common turning strategy which requires the step length to shorten on the inside of the curve [75–80]. The tiger beetle does indeed use step length modulation to turn as shown in figure 3.7. These results suggest that the temporal structure of the full gait cycle is fairly rigid while the spatial coordination is not.

Front leg steering

If the temporal structure of the full gait cycle is set, this allows the tiger beetle to fluctuate the leg positioning and the temporal pattern within a cycle. First we shall study the fluctuation for the front legs, because figure 3.4 indicates that the positioning of the front legs is most strongly effected by the visual input. The AEP angle of the front legs can be well predicted given the error angle θ_e. In addition, Figure 3.4a shows that the AEP position forms an arc around the body, which indicates the angle ψ and the leg length fully determine the leg position.

In addition the outer front leg reduces its step duration while the inner front leg increases its step duration, as seen in figure 3.6. This means the outer leg remains in contact with the ground for a longer time giving it more time to push on the body. At the same time the inner leg has less contact with the ground, perhaps to avoid resistance on the inner side of the turn. This suggest that the front legs, in particular the outer one, is likely responsible for steering of the beetle body.

This corroborates a previous study of stick insects where it has been suggested that visual input drives the action of the front legs more than the other legs [81]. Additionally in a study of cockroach walking [74] it was noted that the front legs, in particular the outer one, are the main producers of the rotational torque required to rotate the body. The results for the tiger beetle's chase behavior fully support both observations.

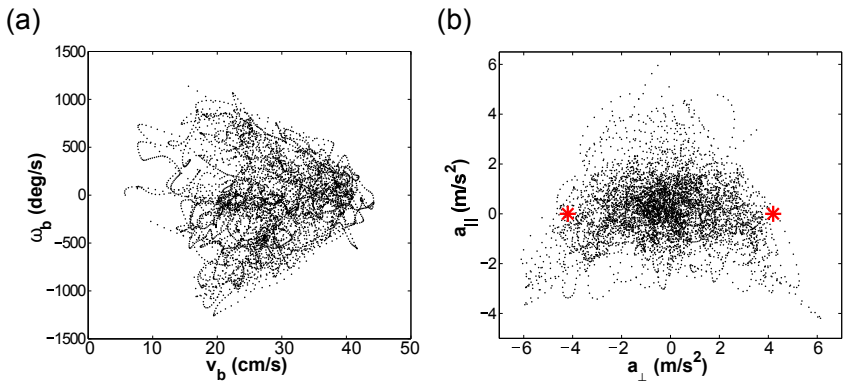

Figure 3.8: a) The beetle's angular rotation rate ω_b as a function of its forwards velocity v_b. The tiger beetle is capable of rotating at 1200deg/s, but that requires a forward velocity around 20 cm/s. A larger forward velocity means a smaller range of rotational velocities is accessible, which indicate a maximum sideways acceleration has been reached. b) The forward acceleration as a function of the perpendicular acceleration shows the limits of the beetle's capabilities. Both forward and sideways acceleration peak at 6m/s^2. The red asterisks indicate the points where the beetle is rotating around an anchored inner middle leg.

Rotating around the middle leg

The middle legs AEP position is also affected by the error angle, as evident in figure 3.4. Just as for the front legs, the middle leg AEP position forms a well-defined arc. The AEP foot angle ψ here is slightly less well predicted by the error angle θ_e, but the effect still shows up clearly. In particular, note that if the beetle is turning sharply towards one side, i.e. for the points in dark red on the left or dark blue on the right of the body, the AEP is almost at the same height as the center of the body. Figure 3.6 indicated that the inner middle leg decreases its step duration, while the outer one increases its step duration. At the same time figure 3.7 shows the step distance of the middle leg goes from essentially zero to over 2cm dependent on the angular rate of the body. Taken together these

results suggest that the inner middle leg becomes the center of rotation around which the beetle turns, especially for sharp turns.

Further estimates show that these results are consistent with this picture of the middle leg as the center of rotation. In figure 3.4, it shows that the middle feet are about 1cm away from the center of mass of the beetle. Given a maximum angular rate of $\omega_b = 1200\text{deg/s}$ and assuming the beetle rotates about the middle leg, a steady state velocity of $v_b = 21\text{cm/s}$ is expected. Figure 3.8a shows that at $\omega_b = 1200\text{deg/s}$ the beetle moves forward at about 20 cm/s, which matches this prediction.

Moreover, the maximal step size of the middle leg can be checked. If the beetle is rotating around the inner leg, the outer leg must move along a radius $r = 2\text{cm}$. This means that during a full stride of $t = 56\text{ms}$, if the beetle is rotating at its maximum rate $\omega_b = 1200\text{deg/s}$, the outer leg has to be moved by $rt\omega_b = 2.3\text{cm}$. This is exactly the maximum step size observed in figure 3.7b. Finally, if the beetle is to maintain this steady state rotation (forward acceleration $a_{\parallel} = 0$) around its inner middle leg, it would have to produce the perpendicular acceleration $a_{\perp} = \omega_v v_b \approx \omega_b v_b = 4.2\text{m/s}^2$. This point, about 0.5g, corresponds to the two asterisks indicated in figure 3.8b, which indeed indicate the maximum perpendicular acceleration on the body for zero forwards acceleration.

Passive hind leg

The remaining legs to be discussed are the hind legs. Their AEP is completely unaffected by θ_e as shown in figure 3.4. The AEP of the hind also appears very localized compared to the arc in the front or middle legs. At the same time the

PEP of the hind leg can be predicted using the angular velocity of the beetle, figure 3.5, while this is not as clear for the front and middle legs. Also observe in figure 3.6 that the hind legs are the legs that have the shortest contact with the ground.

This suggests that the hind leg is not part of an active control loop. The beetle simply pulls up its hind legs to the same location each step and perhaps keeps it airborne as much as possible to avoid unnecessary friction. This passive role of hind legs has been observed earlier [82]. The hind legs of stick insects were found to produce very little force and could even cause the insect to walk backwards and this could very well be the case for the tiger beetle too.

Actuation of the legs

The results here describe a fairly complicated pattern of leg movements that the tiger beetle does while chasing its prey. However, a simple (neural) control circuit might explain most observations. The first step is to give the control circuit a central pattern generator (CPG) which is responsible for maintaining the coordination of the each of the tripods and full gait cycle timing. These CPG are well known to exist in the central nervous system of walking animals [83–85], where they create a basic rhythm that activates the motor neurons of each of the legs. The results showing that the duration of the gait cycle and the tripod step pattern are maintained independently of the turning rate, support the notion of a reliably generated underlying neural pattern.

For the hind legs it seems likely that in the experiments the CPG is the only controller of its movement. The minimal variation of AEP location, figure 3.4,

suggests that there is no circuit actively modulating the placement position of the hind legs. At the same time the arc seen as the PEP location could indicate the hind foot is lifted when the leg is fully stretched. For the front and middle leg this has to be different.

As a second control step, the visual information about the prey is processed and the visual system sends a control signal that modulates the motor neuron output. This gives the motor neuron the information required to provide the correct force and torque to steer and rotate the beetle towards the prey. Producing the torque is likely to be the task of the legs on the outside of the turn as they are better located for that task. Letting the inner legs produce torque in the direction towards the prey would cause a backward force which would slow the beetle down while it is trying to reach the prey. Inner leg torque production could be used if additional rotation speed is required, but this would lead to a deceleration on the body. This might explain figure 3.8b, where the beetle can only reach its maximum sideways acceleration while slowing down.

If the beetle uses the outer leg mostly for torque production, it could then use the inner leg to control the perpendicular force. This is supported by the observation that the middle inner foot is sometimes barely moved forward, which means it is the center of the rotation for the beetle body and thus the point to which the turning force has to point. Figure 3.9 summarizes the results for each of the tiger beetle's legs.

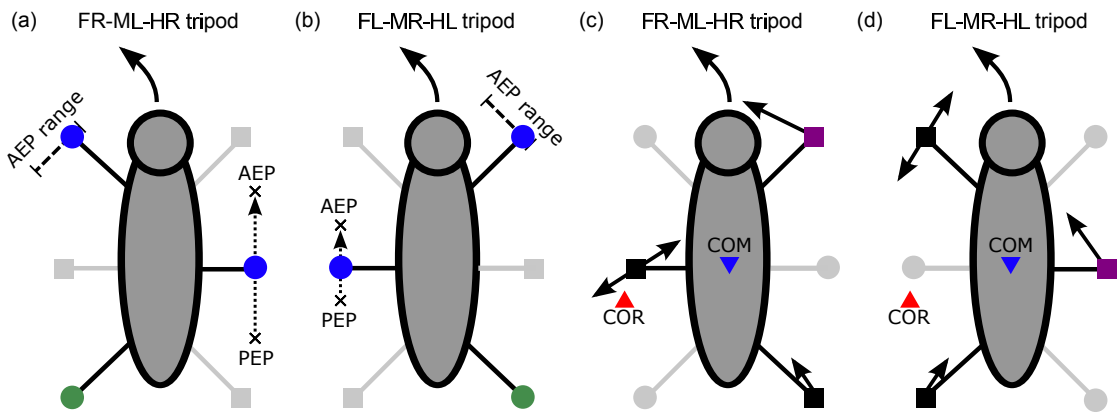

Figure 3.9: Summary of the results for each of the legs in the case where the beetle is rotating counterclockwise. Moving and stationary legs are indicated by circles and squares respectively. (a-b) Blue circles indicate the leg placement is under visual control. For the front legs the range of the AEP during a left turn is shown using a dashed line. For the middle leg the dotted arrow indicates the size of the step made by the leg from PEP to AEP. The green circles mean the leg is returned to a fixed base position with respect to the body. (c-d) Hypothesized forces of each leg on the body indicated by black arrows. Double arrows show the leg is well positioned to modulate the total force and torque on the beetle along the indicated direction. Approximate location for the center of mass (COM) is indicated by a blue triangle. Center of rotation (COR), red triangle, is the approximate point around which the heading vector rotates for extreme sharp turns. It moves outwards for shallower turns. Finally purple indicates the leg is most likely to produce the majority of the torque. To create the figures for the clockwise rotational case one should mirror all images along the body axis.

3.4 Discussion

This chapter studied the feet placement of tiger beetles during their pursuit of preys. The data indicate that the beetle legs could be connected by a CPG, similar to other walking insects. The gait period is mostly independent of the turning rate and the legs maintain a similar triangular placement pattern during the

complete chase. However, closer examination clearly shows modulation in the observed leg patterns.

The AEP of the front legs depends on the visual cues received about the prey direction. In addition, due to a better position compared to the other legs, the front legs are the most likely producers of the torque required to rotate the beetle body towards the prey. The AEP of the middle leg is also modulated by the visual information of the error angle. Moreover, during the sharpest turns, $|\omega_b| > 750\text{deg/s}$, the inner middle leg is only moved over a short distance, around 5mm instead of the normal 17mm. This indicates the center of rotation for the turn lies very close to the inner middle leg. As a result, it is likely that the perpendicular force required to steer the beetle trajectory towards the prey is produced largely by this inner middle leg.

Finally the rear legs show no relation to the visual cues and instead show the strongest correlation between the PEP and body turning rate, figure 3.5. This indicates the hind legs are repositioned in approximately the same location with respect to the body at each step. Therefore they play a small role in the forces and torques required for turning.

The leg actuation mechanism suggested here to explain the observations was also mentioned in [72] to explain leg behavior of a tethered stick insect [81]. It seems that turning behavior elicited in the tethered case by moving stripes and in this case by a moving beetle and prey have a common explanation. However, future experiment should also measure the force generated by the beetle legs in order to confirm how the proportional control law is implemented by the forces due to each leg.

3.5 Conclusion

These first two chapters described the body and leg control of a tiger beetle as it chases its prey. We found a proportional controller that describes how the beetle adjusts the body direction based on the visual input of the prey. This law is also visible in the placement of the front legs and allows the beetle to steer quickly towards the prey.

This proportional controller based on visual information is an example that shows the relatively simple behavior that can emerge out of a complex network of interconnected neurons. One could imagine trying to implement the controller using simple computational elements or groups of neurons. The first element would measure the error angle, by comparing the prey signal from the visual system to the body axis. In a second step the distance information from the eyes would be converted to a particular gain strength. These would be combined in a third element that computes the desired angular velocity. This information is then passed onto the motor neurons to implement. Experiments with live neural recordings during chases could find one or more of these elements in the nervous system [86, 87]. However, if the control spontaneously forms out of the complex network, it might be very hard or even impossible to pinpoint which part of the neural circuitry is responsible for each part of the implementation.

With these studies of insect locomotor control behind us, it is time to take to the skies and add a third degree of freedom to the insect's motion. For insect flight the focus will be on the optimization of the insect's morphology. Where the previous two chapters focused on neural systems, the next two chapters

will attempt to extract simple laws and guiding principles from the evolution of flying insects. For this task we will use the *Drosophila melanogaster* as a model organism.

CHAPTER 4

OPTIMIZING FRUIT FLY FLIGHT BY VARYING THE WING HINGE LOCATION [1]

Understanding Nature's design choices for flying insects appears a daunting task, however for building small flying drones it could be highly beneficial. Millions of years of evolution has likely resulted in optimized flyers, but *a priori* it is not clear what criterium has been optimized for [89–91]. Worse still, the morphological space of possible adaptations is enormous and there is little information to guide our search. Previous studies have mainly focused on the wing motion and on adaptations of the wing's shape and flexibility [25, 92–94]. In this chapter we zoom in on a previously ignored morphological feature: the position of the wing hinge relative to the insect center of mass.

During their evolution, flying insects have developed the ability to control their flight. To deal with the intrinsic instability of flapping flight, flies (order Diptera) use halteres, a pair of stalk-like organs that flap and act as gyroscopes, to sense body rotations [95–97]. Removing or disabling the halteres leads to uncontrolled flight through the growth of an unstable mode that results from the interplay of pitch and horizontal velocity oscillations [98]. However, the flight can be passively stabilized by attaching a string or some fibers to the posterior body segment of the fly [99,100]. These attachments introduce two effects: aerodynamic drag, which damps the motion, as well as a mechanical torque due to the shift between the center of the mass and the center of pressure. It is difficult to separate the drag from the effect of the hinge position in experiments, but in simulations this is possible.

[1] This work is submitted to the Journal of Fluid Mechanics [88].

For this study we use 3D computer simulations to determine how the fruit fly's steady state flight is affected by a shift in the hinge location, which is varied between 2 body lengths below and 8 body lengths above the center of mass (COM). The periodic flight orbits are found by a numerical optimization algorithm that minimizes the single wing beat periodic error for various choices of hinge location and wing stroke amplitude. In addition, perturbations to these steady states are studied using Floquet analysis. This allows to quantify the stability by computing the growth rate of the periodicity error between wing beats.

Our stability analysis of the model fly shows that the hinge position has a relative minor effect on the stability, as long as it is within the body length of a fly. Instead the nominal hinge location on a fly maximizes the ascending speed for a broad range of stroke amplitudes. This implies the hinge has evolved to maximize lift production. At this special hinge location, the coupled wing-body oscillations exhibit an antiresonance, which minimizes the body oscillation due to flapping wing motion. To understand this, we construct a simplified model of two coupled masses. The model indicates that at antiresonance the lift and inertial torques on the body cancel. The minimal oscillation on the body allows the wings to achieve their maximal velocity through the air, thereby generating the maximal lift force. Finally, an expression will be derived for the antiresonance hinge position that shows how it depends on the insect morphology.

4.1 The insect flight simulator

Here the 3D dynamical flight simulation is described, which is used to study the periodic orbits of insect flight and their stability. The simulation determines the time evolution of a flight given the initial conditions and a description of the wing motion. The majority of the model structure existed prior to this work [98], however I made significant improvements to the flexibility of the code and improved the computational speed by a factor of 20-40x. The full simulation model is discussed below. In addition, a completely new element to the analysis is the search for periodic orbits and their stability using Floquet analysis. To find periodic orbits the algorithm searches numerically for an initial flight state vector that returns to itself after a single wing beat simulation. Flight stability is computed using the eigenvalues of the linearized Poincaré map at this periodic initial state.

Three-dimensional dynamic flight simulation

The free 3D flight of a body with flapping wings is simulated by solving the Newton-Euler equations for the coupled wing-body system. The insect model consists of $(n + 1)$ rigid bodies, where n is the number of wings on the body. Each wing is modeled as an ellipsoid connected to the body, also an ellipsoid, through a ball joint that allows for three degrees of freedom in rotation. The body kinematics are given by its position $\vec{r}^b$, linear velocity $\vec{v}^b$, body orientation quaternion $\mathbf{q}^b$, and angular velocity $\vec{\omega}^b$.

Quaternions (in bold throughout this thesis) are four dimensional vectors,

$\mathbf{q} = w + a\hat{i} + b\hat{j} + c\hat{k}$ obeying $\hat{i}^2 = \hat{j}^2 = \hat{k}^2 = \hat{i}\hat{j}\hat{k} = -1$, and unit quaternions, $|\mathbf{q}| = 1$, are used internally in the simulator to represent rotations and orientations states. Their main advantage is that quaternions are not receptive to gimbal lock, while Euler angles are. Gimbal lock occurs when the pitch approaches 90° and the yaw and roll become ill-defined. A numerical simulation of a body using Euler angles will grind to a complete halt near gimbal lock, as infinite small steps are required to maintain the accuracy. The simulation can run into flies that topple over, thus passing through this gimbal lock point, and as such must use quaternions. Note that quaternions are a non-commutative algebra, i.e. the order in which multiplication is performed matters, and calculus is thus slightly complicated. Details on quaternion calculus are explained when they are needed.

The Newton-Euler equations governing the body dynamics are

$$m^b \vec{a}^b = m^b \vec{g} - \sum_{i=1}^{n} \vec{F}_i^c, \tag{4.1}$$

$$I^b \vec{\beta}^b = -\vec{\omega}^b \left(I^b \vec{\omega}^b \right) - \sum_{i=1}^{n} \vec{\tau}_i^c - \sum_{i=1}^{n} \vec{r}_i^b \times \vec{\tau}_i^c. \tag{4.2}$$

Similarly, the governing equations for the i-th wing are

$$m_i^w \vec{a}_i^w = m_i^w \vec{g} + \vec{F}_i^c + \vec{F}_i^a, \tag{4.3}$$

$$I_i^w \vec{\beta}_i^w = -\vec{\omega}_i^w \left(I_i^w \vec{\omega}_i^w \right) + \vec{\tau}_i^c + \vec{r}_i^w \times \vec{\tau}_i^c + \vec{\tau}_i^a. \tag{4.4}$$

Here b denotes body, w denotes wing, m is mass, I is the moment of inertia tensor, $\vec{a}$ is the linear acceleration, $\vec{\beta}$ is the angular acceleration, $\vec{g}$ is the gravitational constant, $\vec{\omega}$ is the angular velocity, $\vec{F}^a$ and $\vec{\tau}^a$ are the aerodynamic force and torque on the wing, $\vec{F}_i^c$ and $\vec{\tau}_i^c$ are the internal force and torque to be determined, $\vec{r}_i^b$ is the position of the i-th wing root relative to the body COM, and $\vec{r}_i^w$ is the position of the i-th wing root relative to the COM of the i-th wing.

Because we have introduced unknown variables in the form of the internal forces, $\vec{F}^c$, and torques, $\vec{\tau}^c$, at the joints, additional equations must be specified. These equations are two kinematic constraints applied at each wing joint. The first is on the angular acceleration of the wing relative to the body,

$$\vec{\beta}_i^r = \vec{\beta}_i^w - \vec{\beta}^b \tag{4.5}$$

which states that the wing acceleration relative to the body must be the prescribed acceleration. The second constraint is the matching condition for the linear acceleration of the wing hinge. The hinge can only have one acceleration whether you describe it in the body coordinates or in the wing coordinates:

$$\vec{a}^b + \vec{\beta}^b \times \vec{r}_i^b + \vec{\omega}^b \times \left(\vec{\omega}^b \times \vec{r}_i^b\right) = \vec{a}^w + \vec{\beta}^w \times \vec{r}_i^w + \vec{\omega}^w \times (\vec{\omega}^w \times \vec{r}_i^w) \tag{4.6}$$

At each instance in time, the coupled dynamic equations 4.1-4.4 together with the constraint equations 4.5 and 4.6 can be cast into a linear system, $Ax = B$, where the vector $x = [\vec{a}^b, \vec{\beta}^b, \vec{a}_i^w, \vec{\beta}_i^w, \vec{F}_i^c, \vec{\tau}_i^c]$, the matrix A contains m_i and I_i, and the vector B contains the known variables with $\vec{\omega}_i$, $\vec{F}_i^a$, and $\vec{\tau}_i^a$ evaluated at that instance in time. We solve this system of equations by inverting the matrix A, using standard lower-upper (LU) decomposition, to find the body accelerations.

Once the body accelerations $\vec{a}^b$ and $\vec{\beta}^b$ are obtained, the body kinematic state evolves in time according to

$$\dot{\vec{r}}^b = \mathbf{q}^b(\vec{v}^b) \tag{4.7}$$

$$\dot{\vec{v}}^b = \vec{a}^b - \vec{\omega}^b \times \vec{v}^b \tag{4.8}$$

$$\dot{\mathbf{q}}^b = \frac{1}{2}\mathbf{q}^b \cdot \omega^b \tag{4.9}$$

$$\dot{\vec{\omega}}^b = \vec{\beta}^b \tag{4.10}$$

Here equation 4.7 rotates the velocity vector from the body frame to the lab frame by the quaternion encoding the body orientation. This quaternion rota-

tion of a vector can be written out in normal vector products by separating the real part, q_0, and complex part, $\vec{q}$, of the quaternion as $\mathbf{q} = (q_0, \vec{q})$. Equation 4.7 becomes:

$$\dot{\vec{r}}^b = \vec{v}^b + 2\vec{q}^b \times (\vec{q}^b \times \vec{v}^b + q_0^b \vec{v}^b) \tag{4.11}$$

In equation 4.9 the operator is quaternion multiplication, which is possible after promoting $\vec{\omega}^b$ to a quaternion by adding a zero real part, i.e. $\omega^b = (0, \vec{\omega}^b)$. This set of nonlinear ordinary differential equations is solved using an adaptive order Adams-Bashforth-Moulton algorithm that ensures the quaternion $\mathbf{q}^b$ remains unitary and thus a representation of the body orientation [101].

The whole simulation model is coded into C++ and compiled as a mex-function library. Mex-function libraries are pre-compiled code that can easily be called from Matlab and this provides a simple framework to interface with the simulator. It allows the C++ code to be highly optimized for fast computation, while also facilitating easy changes to input parameters, analysis of the output, and visualization using Matlab's build-in functions. Significant speed increases for the simulation were possible by using multiple threads to compute the forces $\vec{F}_i^c$ and torques $\vec{\tau}_i^c$ of each wing simultaneously.

Wing motion

The flapping wings move back and forth along a horizontal stroke plane following a pattern similar to that observed in fruit flies, see figure 4.1a. The description of the periodic wing motion is based on a previous study [25]. While internally the simulator uses quaternions, the input and output are described in terms of Euler angles, as they are easier to understand. The time dependence

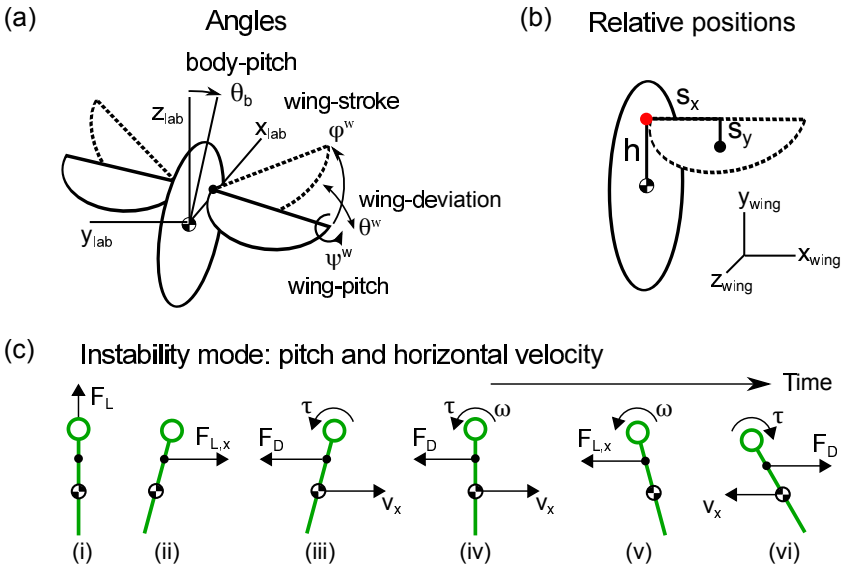

Figure 4.1: (a) Oscillation cycle showing the growth of the main flight instability. An initial deviation in the pitch to the front leads to a forward velocity. The drag due to this velocity causes an even greater pitch deviation backwards, which then leads to a backward velocity. (b) Fruit fly model. The orientation of the body, b, and the wing, w, is each described by a quaternion in the simulations. Each wing is connected to the body through a ball joint. Wings flap symmetrically and thereby restrict the body rotation to the pitch θ_b direction. The stroke amplitude is denoted by ϕ^w. (c) Body and wing parameters. h denotes the height that the wing attachment point (black dot) is located above the body center of mass (COM, a half-filled circle). s_x and s_y are the distances of the wing COM to the wing attachment point along respectively the span and chord direction.

of the three wing angles $\phi^w(t)$, the stroke angle, $\theta^w(t)$, the deviation angle, and $\psi^w(t)$, the wing-pitch angle are given by

$$\phi^w(t) = \phi_0 + \phi_m \frac{\arcsin(K \sin(2\pi f t))}{\arcsin(K)} \tag{4.12}$$

$$\theta^w(t) = \theta_0 + \theta_m \cos(N \cdot 2\pi f t + \delta_\theta) \tag{4.13}$$

$$\psi^w(t) = \psi_0 + \psi_m \frac{\tanh(C \sin(2\pi f t + \delta_\psi))}{\tanh(C)}, \tag{4.14}$$

where ϕ_0, θ_0 and ψ_0 set the mean; ϕ_m, θ_m and ψ_m are amplitudes; f is the wingbeat frequency; δ_θ and δ_ψ are phase shifts; $N = 1$ or 2, $0 < K < 1$ and $C > 0$ are

waveform control parameters. $N = 1$ corresponds to one vertical oscillation per stroke, and $N = 2$ corresponds to a figure-eight motion. ϕ^w becomes sinusoidal when K is close to 0 and triangular when K is close to 1. ψ^w becomes sinusoidal at small C and a step function at large C.

Aerodynamic force model on the wing

The above model, in particular equations 4.1-4.4, require the aerodynamic force and torque on the wings to be specified. The modeling of aerodynamic force on a flapping wing at intermediate Reynolds numbers is a complex subject in itself [102]. Here, just as in [98], a quasi-steady force model is used that takes into account the main unsteady effects, including the dynamic stall, the coupling between wing translation and rotation, and the added mass term. The specific form of the circulation and drag on each blade element is deduced from experiments and numerical simulations of a free falling plate in fluid [103, 104].

The forces on the wings consist of three components coming from circulation, damping and added mass, i.e. $\vec{F}_i^a = \vec{F}_{circ} + \vec{F}_{damp} + \vec{F}_{added}$. For the circulation and damping term, the wing is divided into infinitesimal wing blades along the span and each force is then computed by integrating a force density along the span direction, $\vec{F} = \int \vec{f}(s)ds$, with s the coordinate along the span. For the circulation the force density is given by:

$$\vec{f}_{circ}(s) = -\rho_{fluid}\vec{\Gamma}(s) \times \vec{v}(s) \tag{4.15}$$

with the circulation $\vec{\Gamma}(s) = \frac{c(s)}{2}\left(C_T v(s)\sin(2\alpha(s)) - C_R c(s)\omega_x\right)\hat{s}$. Here $\hat{s}$ is the outward unit vector along the span, ρ_{fluid} is the fluid density, C_T and C_R are coefficients determining the lift dependence on α, $c(s)$ is the local chord length, ω_x

is the x-component of the angular velocity, and $v(s)$ is the absolute value of the local wing velocity. α denotes the angle of attack of the wing, which is the angle that the wing chord makes with the velocity vector. Similarly the damping force density is given by:

$$\vec{f}_{damp} = -\rho_{fluid} k(s) \vec{v}(s) \tag{4.16}$$

with $k(s) = \frac{1}{2} c(s) v(s) (A - B\cos(2\alpha(s)))$ and A and B are coefficients specifying the drag dependence on α.

The last force component is due to added inertia, which stems from the fluid that the wings need to accelerate as they move in their wing beat. This force can be calculated directly using the added mass coefficients:

$$\vec{F}_{added} = \begin{pmatrix} -m_{33} v_z \omega_y \\ m_{33} v_z \omega_x \\ -m_{33} \dot{v}_z \end{pmatrix} \tag{4.17}$$

Here v and ω are the velocity and angular velocity at the center of mass of the wing. m_{33} is an added mass coefficient. The added mass coefficients, m_{33}, m_{44}, and m_{55}, are computed using ellipsoid formulas from [105]. Using the definition $r = 1 - (y/x)^2$, with x the semi-major axis (half span) and y the semi-minor axis (half chord), the added mass coefficients are:

$$m_{33} = \frac{\pi}{6} \cdot \frac{xy^2}{E(r)} \rho_{fluid} \tag{4.18}$$

$$m_{44} = \frac{\pi}{120} \cdot \frac{xy^4(x^2 - y^2)}{(2x^2 - y^2)K(r) - y^2 E(r)} \rho_{fluid} \tag{4.19}$$

$$m_{55} = \frac{\pi}{120} \cdot \frac{x^3 y^2 (x^2 - y^2)}{(x^2 - 2y^2)K(r) + y^2 E(r)} \rho_{fluid} \tag{4.20}$$

with $K(r)$ and $E(r)$ the elliptic integrals of the first and second kind respectively.

The wing torques can also be divided in the same three components: $\vec{\tau}_i^a = \vec{\tau}_{circ} + \vec{\tau}_{damp} + \vec{\tau}_{added}$. The first two are computed by integration of the torque

Table 4.1: Summary of the default fruit fly morphological parameters.

Fruit fly morphology					
m_{body}:	1.1 mg	m_{wing}:	0.0036 mg	h:	1 mm
Body length:	2.4 mm	Wing span:	2 mm	s_x:	0.866 mm
Body width:	1.2 mm	Wing chord:	1 mm	s_y:	0.25 mm

density along the blade elements $\vec{\tau} = \int \vec{s} \times \vec{f}(s) ds$, with the force densities given previously. Finally, the added mass torque is computed directly using:

$$\vec{\tau}_{added} = \begin{pmatrix} -m_{44}\dot{\omega}_x + m_{55}\omega_y\omega_z - m_{33}v_y v_z \\ -m_{55}\dot{\omega}_y - m_{44}\omega_x\omega_z + m_{33}v_x v_z \\ (m_{44} - m_{55})\omega_x\omega_y \end{pmatrix} \tag{4.21}$$

Model parameters

The morphological parameters are set similar to those measured on real fruit flies, *Drosophila melanogaster*, which allows for comparisons with related studies [98], see table 4.1. The fly has body weight m_{body} = 1.1 mg, length = 2.4 mm, width = 1.2 mm; wing weight m_{wing} = 3.6×10^{-3} mg, span = 2 mm, maximal chord = 1 mm, and maximal thickness = 0.1 mm. The wings are attached h = 0.96 mm above and 0.36 mm to the side of the body COM, with the COM of the wing s_x = 0.866 mm along the span and s_y = 0.25 mm along the chord direction from the hinge location, see figure 4.1b. The aerodynamic force parameters are fixed at C_T = 1.5, $C_R = \pi$, A = 1.4, B = 1 and ρ_{fluid} = 1.293 g/L.

For modeling the wing the following parameter values are used: f = 250Hz, $\phi_m = 70°$, $\phi_0 = 0°$, K = 0.7, $\theta_m = \theta_0 = 0°$, $\psi_m = 53°$, $\psi_0 = 90°$, $\delta_\psi = 72.4°$, and C = 2.4. They are summarized in table 4.2. For simplicity, the deviation θ from the main

Table 4.2: Summary of the default fruit fly wing motion

Fruit fly wing motion			
Frequency f:	250 Hz	Wing pitch ψ_0	90°
Stroke ϕ_m:	70°	Wing pitch ϕ_m	53°
Shape parameter K:	0.7	Wing pitch δ_ψ	-72.4°
Shape parameter C:	2.4	$\theta^w(t)$:	0

stroke plane is neglected, and the phase shift δ_ψ in $\psi^w(t)$ is such that the wing pitches in advance of the wing stroke reversal. The listed values here and in the tables are the fruit fly defaults and when a parameter is varied for the study it is clearly indicated in the relevant figure.

4.2 Periodic flight search and Floquet stability computation

The stability of periodic flights of model flies is studied using Floquet analysis. First, these special flight states need to be identified by using the simulator to search for closed paths through the flight parameter space with a period of 1 wing beat. A longitudinal flight state is fully specified by the initial state vector $\vec{s} = [v_x, v_z, \theta_b, \omega_y]$ with the horizontal velocity v_x, the vertical velocity v_z, the body pitch θ_b and the angular velocity in the pitch direction ω_y. A search algorithm, written in Matlab, finds a periodic flight state by adjusting the initial state $\vec{s}_0$ until it minimizes the periodicity error $\epsilon = ||M(t, \vec{s}_0) - \vec{s}_0||$. Here M is the function that simulates a single wing beat using the flight model, thus $\vec{s}(t+T) = M(t, \vec{s}(t))$, with T the wing beat period. The search algorithm consists of a series of executions of the simplex minimum optimization function, where each cycle combines the

previous best periodic state with periodic states of nearby model parameters to seed a new minimum search. The resulting flights have a typical periodicity error of $\epsilon = 10^{-6}$, but an occasional outlier of $\epsilon = 10^{-3}$ remained.

The function M defines a Poincaré map on the flight state space, see figure 4.2a, and periodic flight states correspond to fixed points of the map M. This allows for the model to be phrased in terms of Floquet theory, by defining a function f, which describes the instantaneous change to the flight state: $\dot{\vec{s}}(t) = f(t, \vec{s}(t)) = \frac{dM(t,\vec{s}(t))}{dt}$. A periodic flight $\vec{s}(t)$, which starts at the initial state $\vec{s}_0$, is also a solution to this differential equation. The stability of the solution is determined by examining how the difference with a nearby state $\vec{s}_\delta(t)$, which started on $\vec{s}_0 + \vec{\delta}$ evolves over time. The difference of the two solutions $\vec{z}(t) = \vec{s}_\delta(t) - \vec{s}(t)$ evolves according to the differential equation:

$$\dot{\vec{z}}(t) = f(t, \vec{s}(t) + \vec{z}(t)) - f(t, \vec{s}(t)) \tag{4.22}$$

$z(t)$ is assumed to be small as it is a difference of two nearby solutions. Following [106], equation 4.22 is then linearized around zero:

$$\dot{\vec{z}}(t) = A(t)\vec{z} + o(|z|) \approx \left.\frac{\partial f}{\partial \vec{s}}\right|_{t,s(t)} \vec{z}(t) \tag{4.23}$$

The linear term $A(t)$ is the Jacobian of f with respect to the flight state $\vec{s}$. In this linearized regime the solutions can be written as $\vec{z}(t) = P(t)\vec{y}(t)$. Here $P(t)$ is a periodic matrix and $\vec{y}(t)$ is a solution to the simpler equation $\dot{\vec{y}}(t) = D\vec{y}(t)$ with D a constant matrix. D is the Jacobian of the finite difference over a full period of our model M.

$$D = \left.\frac{\partial}{\partial \vec{s}}\left(\frac{M(T, \vec{s}) - \vec{s}}{T}\right)\right|_{s=s_0} \tag{4.24}$$

This method essentially splits the time evolution of $\vec{z}(t)$ in an intra-cycle component, $P(t)$, and an inter-cycle component, $\vec{y}$. This removes any periodic effects

on the change in state and allows us to observe if the deviation $\vec{z}(t)$ is growing or decreasing over times larger than a wing beat. The solutions for $\vec{y}(t)$ are of the form $\vec{y}(t) = \vec{y}_0 \exp(\lambda t)$, with λ the eigenvalues of D known as Lyapunov exponents. If $\max(\mathrm{Re}(\lambda)) < 0$ the inter-cycle deviations decrease in size and the original solution $\vec{s}(t)$ is stable. Otherwise the largest real part of the set of Lyapunov exponents will indicate the timescale to instability, since after $1/\lambda$ the instability will have grown by a factor of e.

Moreover, the associated eigenvector of D will indicate which deviations lead to instability. The main mode of instability for a longitudinal flight is the pitch instability [98, 100, 107], due to the dynamic coupling between the body pitch and forward motion. (figure 4.1c) For this instability, an initial deviation in the pitch directs the lift force forward. This causes a forward velocity, which then pitches the body back the opposite way due to drag on the wings. This results in a backward velocity and thus rocks the body back and forth with increasing body pitch angle. If this mode is unstable, the fly eventually tumbles out of control.

For ease of interpretation, the eigenvalues $\alpha = \exp(\lambda T)$ of the linearized map M are used to indicate the stability of the flight [106]. The α_i are the multiplicative factors by which deviations away from the periodic state grow after a single wing beat. If all $|\alpha_i| < 1$, then all deviations shrink in size and the flight is stable. However, if there is at least one $|\alpha_i| > 1$ then the flight is unstable.

Figure 4.2b-d show three examples of periodic initial flight states for different stroke amplitudes with the computed eigenvalue for each listed on the graph. For $\phi_m = 65°$ (b) the flight is started at a pitch deviation of 20° away from the periodic solution and we observe the slow decay towards the periodic solu-

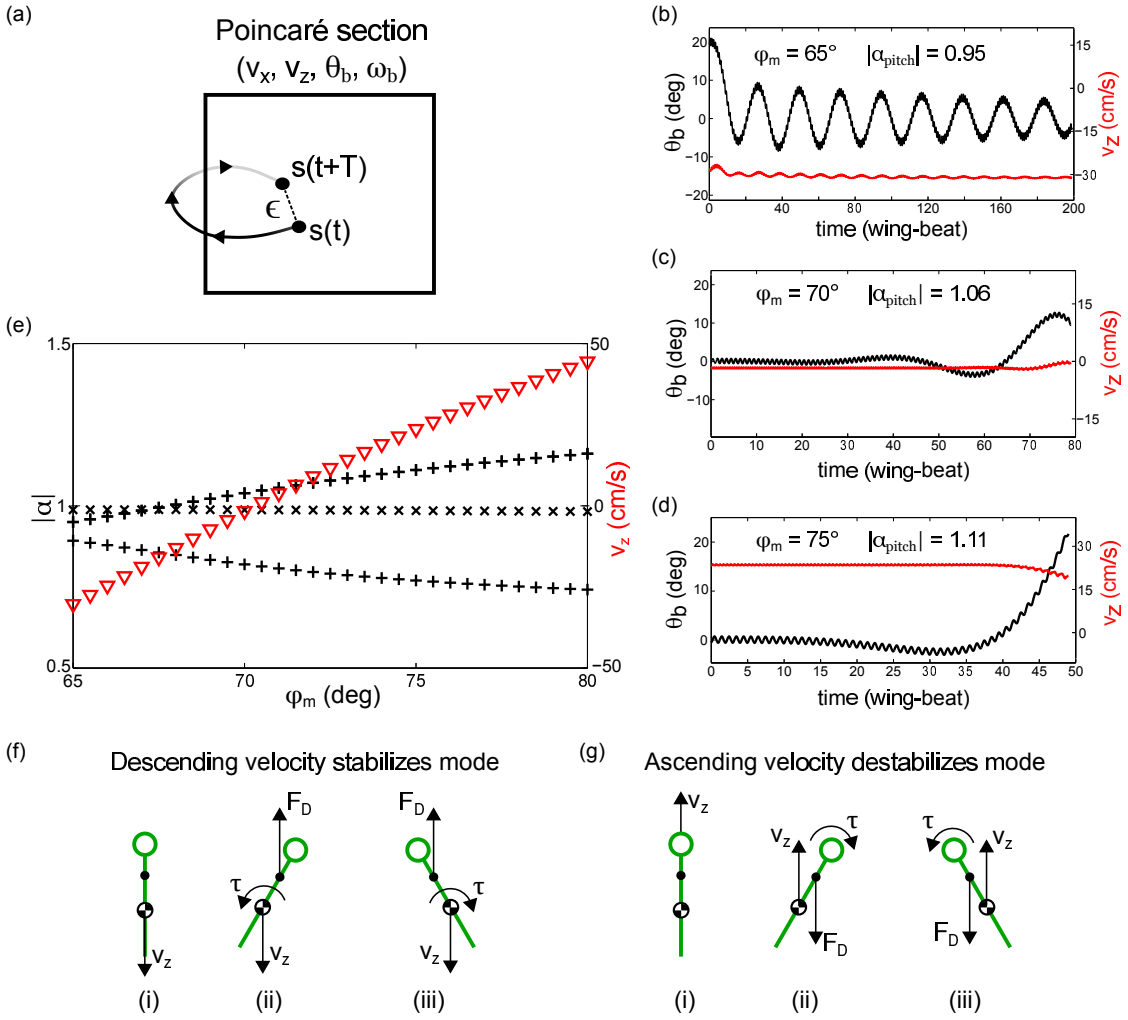

Figure 4.2: (a) The one wing beat forward integration of the flight model defines a Poincaré map. Steady state flights correspond to fixed points of this map. (b-d) Examples of periodic flights started out of equilibrium. Graphs show the body pitch, θ_b, and vertical velocity, v_z, for stroke amplitudes, ϕ_m, corresponding to descending (b), hovering (c) and ascending flight (d). (e) Norm of the eigenvalues and the vertical velocity as a function of the stroke amplitude. $\times$ indicates the eigenvalue associated with vertical velocity deviations, + indicates eigenvalues associated with pitch deviations. We observe that ascending flight is unstable, while descending flight is stable. (f) The descending velocity creates a torque that aims to keep the fly upright, thereby stabilizing the flight. (g) Ascending velocity instead creates a torque that increases any pitch deviation making the flight unstable.

tion since the flight is stable. However, for $\phi_m = 70°$ and $75°$ (c-d) the flight is unstable and the initial deviation of $0.1°$ in the pitch grows through the typical pitch instability mechanism. The graphs indicate that the method is successful in finding periodic flights and that their stability properties match with the computation based on the linearized Poincaré map.

4.3 Simulation results for changes to the wing hinge location

Descending flight is stable

The Floquet analysis of periodic flight states leads to the finding that descending flight is stable. Figure 4.2e shows how the stability and vertical velocity change over the full range of stroke amplitudes in the study, $\phi_m \in [65°, 80°]$. The figure only displays three eigenvalues over the whole range, because one represents a complex pair. The eigenvalue, indicated by $\times$, that remains at $\alpha_i = 0.99$ is associated with deviations in the vertical velocity. The other eigenvalues, denoted by +, are associated with the pitch. The one that crosses the $|\alpha| = 1$ line is also the complex pair. Note that the flight is stable only for small stroke amplitude where there is a significant descending velocity.

The reason why descending flights become stable is that the velocity creates a stabilizing torque that restores the body in the upright position, see figure 4.2f. When there is a deviation in the pitch of the descending fly, the drag from falling creates an upward force, see (ii). This force creates a torque that aims to upright the body irrespective of the initial pitch deviation, see (iii). However, as shown in figure 4.2g, an ascending velocity always leads to a drag in the

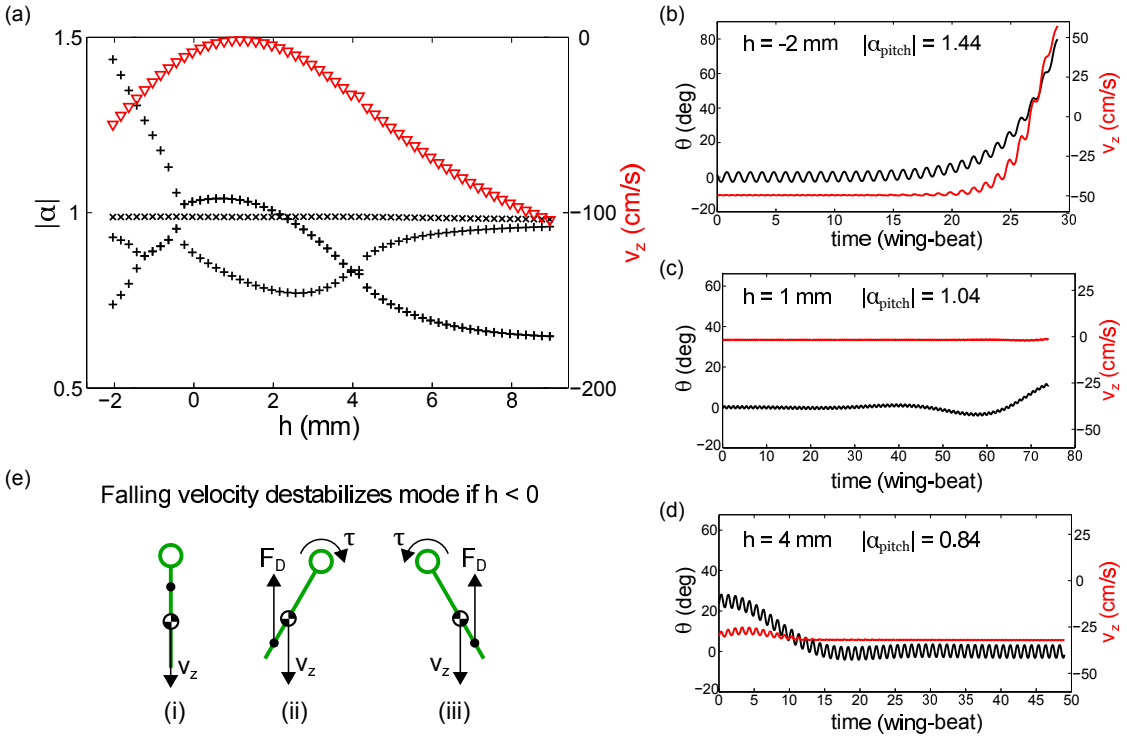

Figure 4.3: (a) Norm of the eigenvalues and the vertical velocity as a function of hinge location, h. Markers as in figure 4.2. Note that raising the wing hinges stabilizes the flight. In addition, observe that a hinge below the COM is highly unstable. The small artifact at $h = 4.2mm$ is due to bad numerical convergence of the periodic state. (b-d) Examples of periodic flights started out of equilibrium. Graphs show the body pitch, θ_b, and vertical velocity, v_z, for hinge positions below (b), at (c), and above (d) the location observed in real fruit flies. (e) In contrast to figure 4.2f, if $h < 0$ the descending velocity creates a torque that aims to increase the pitch deviation, thereby destabilizing the flight.

opposite direction and thus in a torque that increases any pitch deviations. The result is that descend leads to stable flight, while hovering and ascending flight are unstable.

Raising the hinge leads to stable, but descending flight

In the introduction it was suggested that raising the wing hinges with respect to the fly COM might suppress the unstable mode, based on experiments with flies that had their active feedback control disabled [99,100]. Here we study this idea. Figure 4.3a shows how the stability eigenvalues α and the steady state vertical velocity, v_z, are affected by changes in the hinge location h. Similar to the case of stroke amplitude changes, there is a single $|\alpha_i|$ that remains constant at 0.99 which is associated with deviations in vertical velocity, indicated by $\times$. The other three eigenvalues, indicated by +, are associated with the interplay between pitch and horizontal velocity.

Increasing h does indeed lead to stability, as for $h > 2$mm all $|\alpha_i| < 1$, which confirms the hypothesis. Note that in the case that the wings are below the COM ($h < 0$) the fly becomes increasingly unstable. Example flights are shown in figure 4.3b-d for the hinge located below the COM (b), at the normal position (c), and significantly above the normal position (d). Looking at the vertical velocity, we see that both raising the hinge for stability and lowering the hinge below the COM lead to a descending steady state flight.

Raising the hinge location thus leads to stability because it leads to descending flight which then stabilizes the flight through the mechanism of figure 4.2f. However two questions remain: why does raising or lowering the hinge effect the vertical velocity of steady state flight, and why does a negative hinge location lead to highly unstable flight. The first question will be addressed later, but the answer to the second one can be quickly provided by figure 4.3e. By moving the hinge below the COM the drag force resulting from the falling velocity no longer creates a torque that rotates the fly to the upright position. Instead the

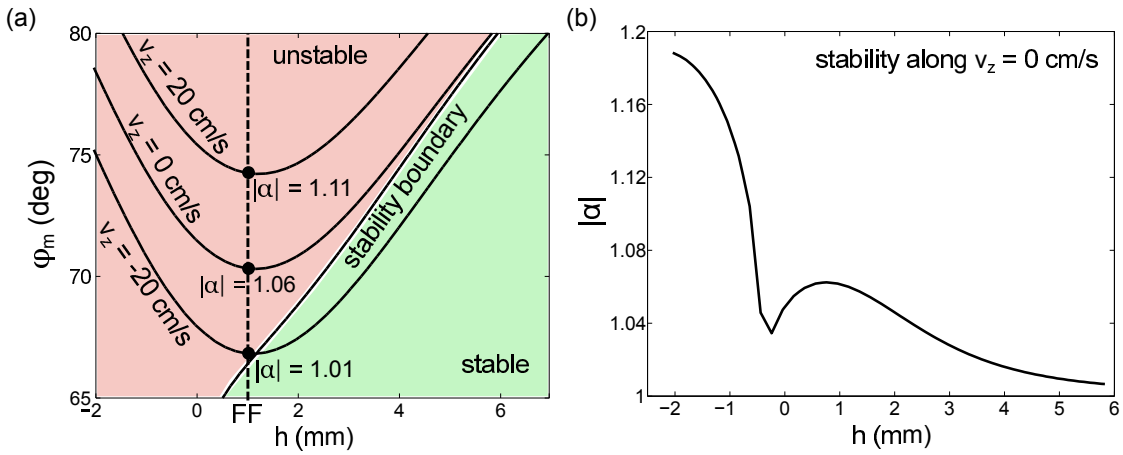

Figure 4.4: (a) Contour plot showing how vertical velocity and stability depend on both stroke amplitude and hinge location. The stability boundary labels the line where $|\alpha| = 1$. The velocity contours indicate how hinge and stroke amplitude should be adjusted to maintain the same periodic vertical velocity. (b) The norm of the largest stability eigenvalue along the hovering contour. It shows that hovering flight is not stable for any hinge location studied. It does appear that in the limit for large h the flight approaches stability.

torque has switched direction and will now destabilize the flight.

Hovering and ascending flight is unstable

Previously the results showed that changes to the hinge location not only changed the stability, but also the steady state velocity. In order to eliminate this velocity effect and study the stability of hovering flight, we must vary stroke amplitude and hinge location simultaneously, as is done in figure 4.4a.

It shows that hovering and ascending flight does not become stable by increasing h, because the 0 and 20cm/s velocity contours never cross the stability boundary. Moreover, the fruit fly's natural hinge location h = 1mm does not

appear to have special stability properties. Figure 4.4a clearly shows that the stability boundary does not lie along the fruit fly's hinge (dashed) line. Figure 4.4b shows the largest eigenvalue $|\alpha|$ along the hovering contour of figure 4.4a. Increasing h above 1mm reduces the instability and the eigenvalue approaches the stability boundary in the limit of large h. However, figure 4.4 makes it clear that hovering and ascending flight cannot be stabilized by changes to the hinge location.

Previously it was shown that a descending velocity creates a stabilizing torque, see figure 4.2. Since this mechanism does not work for hovering or ascending flight, one could have expected those flights to remain unstable. Note that raising the hinge will still increase the rotational damping torque and thereby reduce the rotational velocity. However, this can only slow down a pitch deviation and does not bring the fruit fly back upright, and as a result this effect only reduces the instability, but cannot actually create stable flight.

h = 1mm maximizes v_z

We will now study the periodic flight states themselves and make the striking discovery that the vertical velocity is maximal for the fruit fly's natural hinge position. Figure 4.5 shows how the fly's upward velocity changes as the vertical hinge position is varied between -2 and 8mm, for various stroke amplitudes between 65° and 80°. The figure clearly indicates there exists a special hinge location h_0 that leads to a maximum in the vertical steady state velocity, independent of the stroke amplitude. In the figure each contour of constant stroke amplitude achieves its maximal velocity at h_0 = 1mm, the natural hinge location

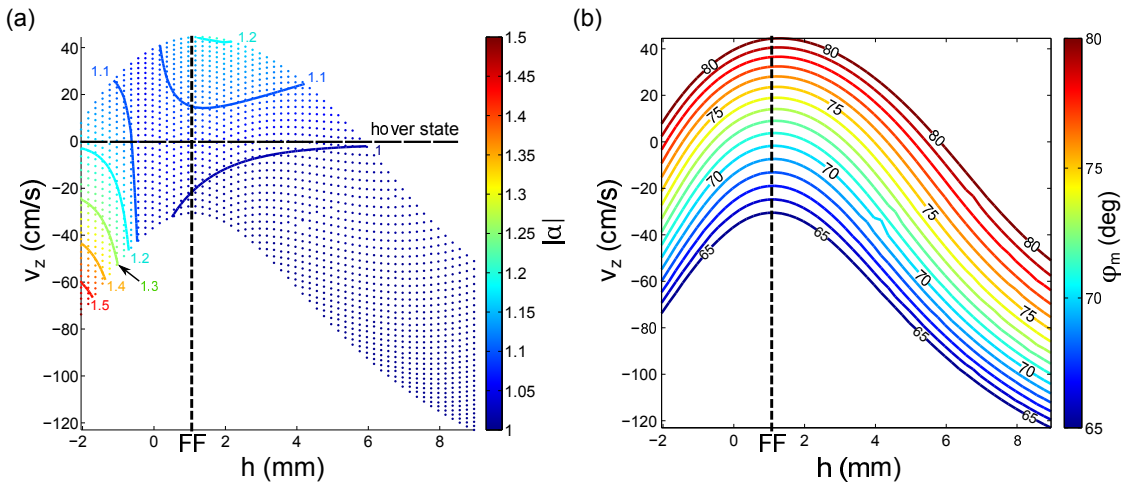

Figure 4.5: (a) The effect of hinge location and vertical velocity on flight stability. The dashed line at $h = 1$mm indicates the hinge location of the unaltered fruit fly. We can observe all the previously shown effects: ascending velocity leads to instability, descending velocity for $h < 0$ leads to instability, and descending velocity for $h > 0$ leads to stability. The graph also indicates that for $h = 1$mm the periodic flights achieve a maximum vertical velocity. (b) Constant stroke amplitude contours show that given any stroke amplitude the maximum steady state vertical velocity is achieved at $h = 1$mm. Because all flights are in steady state, the maximum in v_z corresponds to a maximum in lift generated by the fly.

of the fruit fly. Therefore the fly's natural hinge location maximizes v_z.

The remainder of this chapter explains this result. Firstly, because we study periodic flights, the maximum in v_z implies a maximum in lift production. Secondly, the maximum in lift production comes about through a maximum in wing velocity relative to the air, which is possible due to an antiresonance in the wing-body system leading to a minimal body oscillation. Finally, a reduced model will be constructed to study this antiresonance and it will indicate that at antiresonance the inertial and lift torques on the body cancel out and thereby reduce the sway of the body pitch.

First, we argue that at h_0 the fly must have a maximum in lift production. In steady state the vertical acceleration after one wing beat is zero and thus the upward lift and downward drag must cancel each other out. Since the drag $F_D \propto v_z$, this implies that the maximum in the v_z corresponds to a maximum in upward force generation. Moreover, it implies a maximum in lift force, because the fruit fly has a horizontal stroke plane and during the flight the body pitch oscillates only by about one degree, see figure 4.6a. Thus h_0 is the hinge location that maximizes the lift generated by the fruit fly.

Antiresonance leads to maximum lift

The lift maximum at h_0 should be understood in terms of the body pitch oscillation, because an oscillating body tends to reduce the lift. When the body oscillates, the wing hinge attains a velocity, $v_h = \omega_y h$. Irrespective of h this hinge velocity reduces the effective wing velocity relative to the air, v_w. Since the lift $F_L \propto v_w^2$, a reduced wing velocity implies reduced lift. The change in angle of attack also will effect the lift, but this is a smaller effect. As a result a minimum body pitch oscillation is expected with the hinge at h_0.

Looking at the fruit fly as a coupled model of the body, an inverted pendulum, driven by the wings allows the body pitch oscillation to be analyzed. Figure 4.6a-b shows the amplitude and phase delay of the body pitch, as a function of the hinge location, when the body is driven by the wings. The combination of a minimum in oscillation amplitude and a phase jump indicates an antiresonance that occurs when the hinge is at $h^* = 0.5$mm. The inset of figure 4.6a shows the definition of the amplitude A_b and phase delay $\Delta\Phi$. Since the body

pitch is a nearly linear response to the driving oscillation of the wing, the response can be described in terms of the amplitude and phase delay. A phase delay of 0°, or 90°, occurs when the body is pitched maximally forward at the instant the wings are respectively at their front most position, or at the middle of the stroke and moving forward. The main graph of figure 4.6a shows that irrespective of the stroke amplitude, the body oscillation amplitude is least at h^*. At the same hinge position the phase delay jumps by 180°, as indicated in figure 4.6b. Together these effects provide evidence for an antiresonance occuring when $h = h^*$.

A new reduced model reproduces the antiresonance

To further understand the antiresonance in the body pitch and possibly predict the value of h^*, we will construct a reduced model. First, we define the model, which treats the wings as point masses that experience simplified lift and drag forces, and show that it reproduces the antiresonance. Next special limits of the model will be studied, where it can be shown that antiresonance occurs when the lift and inertial torques cancel. Finally, a formula is derived that can be used to predict the value of h^* for other flyers.

The reduced model defines the wings as point masses, positioned at the original wing COM, which experience three forces: inertial, vertical lift, and horizontal drag, see figure 4.6c. The lift force on both wings is constant in time and together equal to the total weight, $F_L = m_t g$. Here the total mass $m_t = m_b + 2m_w$ is the sum of body and wing masses. For periodic flights this assumption must be reasonably accurate, because the periodicity in v_z enforces the average accel-

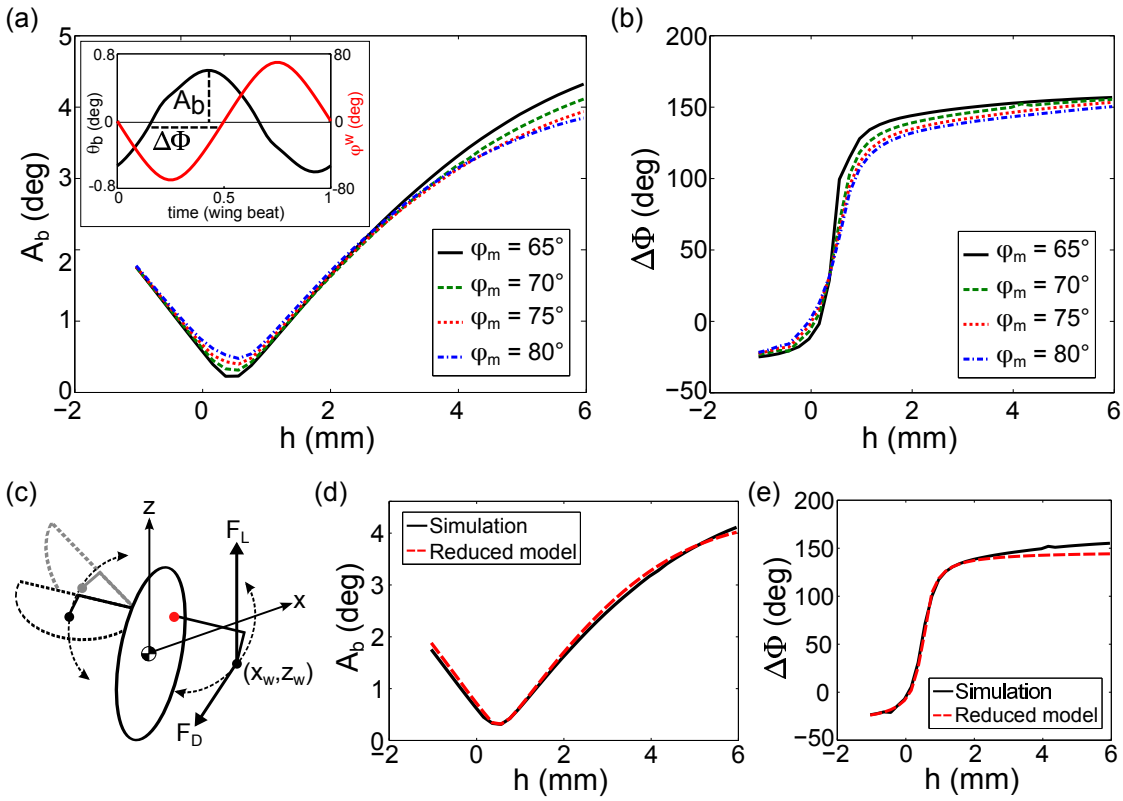

Figure 4.6: (a) Amplitude of the body pitch oscillation as a function of the wing hinge. The body oscillates least for $h = 0.5$mm irrespective of the stroke amplitude. Inset shows that the intra wing beat oscillation of the body pitch θ_b is approximately a linear response to the driving stroke amplitude ϕ^w. This allows us to definite an oscillation amplitude A_b and phase shift $\Delta\Phi$. (b) The phase shift as a function of wing hinge position jumps up by 180° around the same $h = 0.5$mm, independent of stroke amplitude. These graphs indicate that altering the hinge position can lead to an antiresonance in the body pitch response. (c) The reduced model treats the wings as point masses (black dots) at the original COM. In addition lift F_L and drag F_D are simplified. See text for details. (d-e) The model can reproduce the antiresonance, as it is in excellent agreement with the results of (a) and (b).

eration to be zero and therefore the average upward force must equal $m_t g$.

For the drag, assume a constant lift-to-drag ratio of $r_{L/D} = 1.2$. This is accurate around hovering, which most of the flights are, with an angle of attack of about 37°. The total forces, including an inertial term due to the wings, and torque on the body is then given by equations 4.25-4.27.

$$F_x(t) = -m_w \ddot{x}_w(t) - \text{sgn}(\dot{\phi}^w(t)) \frac{m_t g}{2 r_{L/D}} \cos(\phi^w(t)) \tag{4.25}$$

$$F_z(t) = -m_w \ddot{z}_w(t) + \frac{m_t g}{2}, \tag{4.26}$$

$$\tau_y(t) = 2\left(1 - \frac{2m_w}{m_t}\right)(z_w F_x - x_w F_z) \tag{4.27}$$

Parameter are defined in figure 4.1a-b and figure 4.6c. Note that the total force in the y-direction is zero due to the symmetric stroke, ϕ^w, which is specified in equation 4.12. The mass fraction in the torque equation takes into account that the insect COM is affected by the weight of the wings. Finally x_w and z_w describe the wing COM during the wing beat and can thus be expressed as

$$x_w(t) = s_x \sin(\phi^w(t)) - s_y \cos(\psi^w(t)) \cos(\phi^w(t)) \tag{4.28}$$

$$z_w(t) = h - s_y \sin(\psi^w(t)). \tag{4.29}$$

The body pitch oscillation is found by solving for θ_b from $I\ddot{\theta}_b = \tau_y$, where the moment of inertia $I = I^b + 2m_w \left(1 - \frac{2m_w}{m_t}\right)^2 h^2 + m_b \left(\frac{2m_w}{m_t}\right)^2 h^2$. Once θ_b is computed, the amplitude A_b and phase $\Delta\Phi$ are determined exactly as for the full simulation, see figure 4.6a.

The reduced model should be compared to the simulations by again examining the body oscillation as h is varied. Figure 4.6d-e show that the reduced model accurately reproduces the antiresonance. The reduced model, red dashed line, matches with the full simulation, black line, for both the amplitude and

phase shift. The location of the antiresonance in the model is also the same, with the minimum amplitude and phase jump occurring at $h^* = 0.5$mm. This allows us to study the more tractable reduced model in order to understand the origin of the body pitch antiresonance.

Prediction of h*

Here the newly constructed reduced model is used to study the antiresonance for simple limits and a prediction for h^* will be derived. We start by separating the pitch torque by its three components, inertia τ_I, lift τ_L and drag τ_D:

$$\tau_I = -2m_w\left(z_w\ddot{x}_w - x_w\ddot{z}_w\right)\left(1 - \frac{2m_w}{m_t}\right) \tag{4.30}$$

$$\tau_L = -x_w m_t g\left(1 - \frac{2m_w}{m_t}\right) \tag{4.31}$$

$$\tau_D = -\mathrm{sgn}(\dot{\phi}^w) z_w \frac{m_t g}{r_{L/D}} \cos(\phi^w)\left(1 - \frac{2m_w}{m_t}\right) \quad \propto \quad \cos(\phi^w) \tag{4.32}$$

Note that the drag torque is proportional to the cosine of the stroke angle. If the body oscillation is only driven by drag, one would expect to see a phase delay $\Delta\Phi = 90^\circ$ between body and wing, exactly the phase found in figure 4.6d at the minimum oscillation. Thus, this minimum occurs when all terms in phase with a sine cancel out.

During the majority of the stroke the contribution coming from the inertial and lift torques are proportional to sine functions, which is most easily seen in the case where wing reversal is ignored. We can do this by taking $s_y = 0$ and using the stroke $\phi^w(t) = \omega t$, with $\omega = 2\pi f$. In this limit the inertial and lift torque simplify to:

$$\tau_I = 2m_w h\omega^2 s_x \sin(\omega t)\left(1 - \tfrac{2m_w}{m_t}\right) \quad \propto \quad +\sin(\phi^w) \tag{4.33}$$

$$\tau_L = \quad -m_t g s_x \sin(\omega t)\left(1 - \tfrac{2m_w}{m_t}\right) \quad \propto \quad -\sin(\phi^w) \tag{4.34}$$

These equations make it clear that there exists a hinge location that allows the inertial and lift torques to cancel and drag to dominate the body oscillation. This hinge location is given by

$$\frac{h^*}{L} = \frac{m_t}{2m_w} \cdot \left(\frac{\omega_0}{\omega}\right)^2 \tag{4.35}$$

Here L is the length of the fly's body and $\omega_0^2 = g/L$. It implies the ratio of the hinge height over the body length is set by the ratio of total fly mass over the total wing mass and the ratio of the natural body frequency over the wing frequency. Plugging in the fruit fly parameters this hinge location is $h^* \approx 0.61$mm, which is close to the observed h^* in the simulations. The difference is likely due to ignoring wing reversal.

Given the finding that at $h = h^*$ the lift and inertial torques will cancel, the different limits of figure 4.6b can be understood. For the case where $h > h^*$ inertial torque will dominate the lift torque and the phase shift is higher $\Delta\Phi > 90°$. Note that the limiting value for $h \to \infty$ is not necessarily 180°, because the drag torque is also proportional to h. Similarly for $h^* > h > 0$ the lift torque will dominate the inertial torque and the phase shift is lower $\Delta\Phi < 90°$. For the case where $h \ll 0$ the inertia can come to dominate again, but it will no longer cancel and instead strengthen the oscillation due to lift. The phase there is thus well below 90°.

Finally, more details on the accuracy of the model can be provided and the prediction made in equation 4.35 can be checked. Figure 4.7a-b compares the forces and torques of the reduced model, equations 4.25-4.27, with those extracted from the full simulation. There is an excellent agreement between the simulation and the model. The sinusoidal oscillation in F_z and τ are due to the

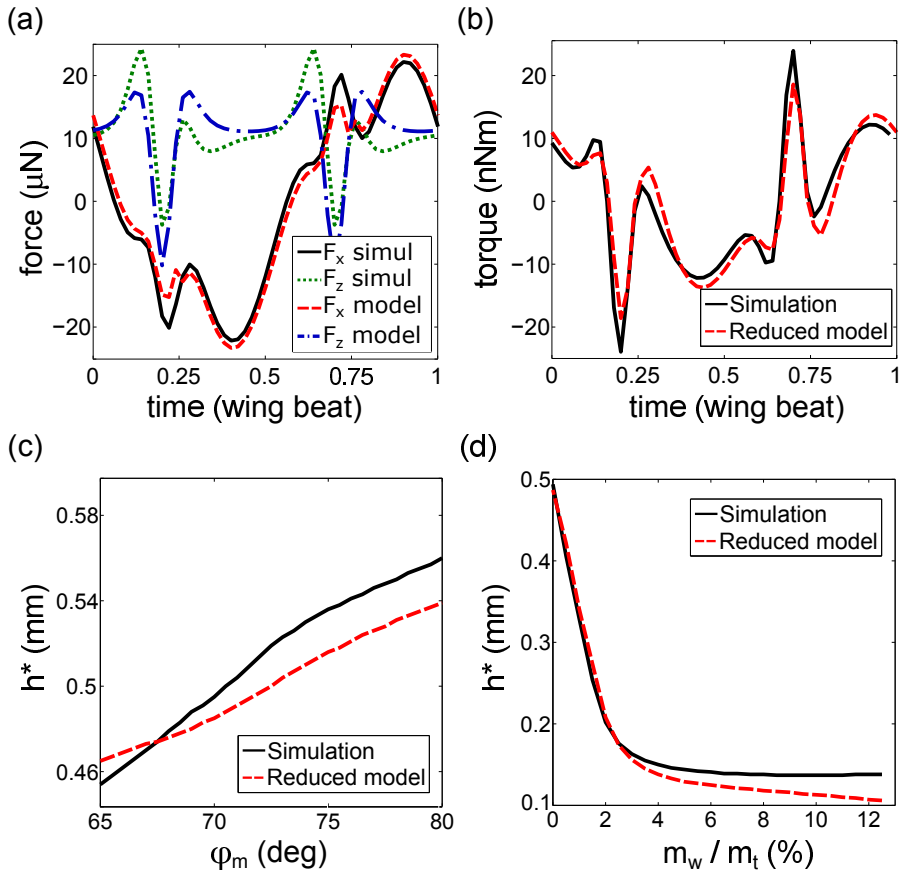

Figure 4.7: Comparing the simulation and reduced model. (a-b) Despite assuming a constant lift and drag force, the new model accurately reproduces the force and torque profile on the fly during a single wing beat. (c) From the simulations we see that the hinge location that minimizes the amplitude increases slightly as a function of stroke amplitude. The reduced model also contains this feature. (d) The model predicts, equation 4.35, that the hinge location for the minimum amplitude should decrease sharply with increasing wing mass. Subsequent full simulations confirm this prediction.

main stroke of the wing, while the sharp spikes at 1/4 and 3/4 of a wing beat are due to wing pitch inversion. Figure 4.7c shows the exact hinge location of the minimum amplitude A_b. The reduced model reproduces the simulator results with an error of about 5% on h^*. The final check on the model is to test the prediction of equation 4.35 that h^* should decrease, if the ratio of the wing mass to the total mass is increased. The results of additional simulations, shown in figure 4.7d, validate the model prediction. The hinge location that minimizes the amplitude does indeed drop significantly as predicted with increasing wing mass.

Wing reversal shifts optimal hinge for lift

One open end that is still left is the question of why the antiresonance occurs at $h = 0.5$mm, while the maximal lift hinge is located at $h = 1.0$mm. It turns out that the difference is due to the detailed effects of the wing reversal as figure 4.8 shows.

We compare a periodic flight with the hinge located near antiresonance, $h = 0.6$mm, with a hinge far out of resonance, $h = 2.6$mm. The difference in velocity and force are displayed in figure 4.8a. The main effect is that due to the antiresonance the wing velocity during the main stroke (white region) is much greater for $h = 0.6$mm than it is for $h = 2.6$mm. The direct effect is that the lift force $F \propto v^2$ is also much larger. Even during wing reversal the wing velocity of the $h = 0.6$mm fly is greater. As a result the fly's vertical velocity will be much larger for $h = 0.6$mm than it is for $h = 2.6$mm.

However, when comparing a flight at antiresonance to a flight with $h =$

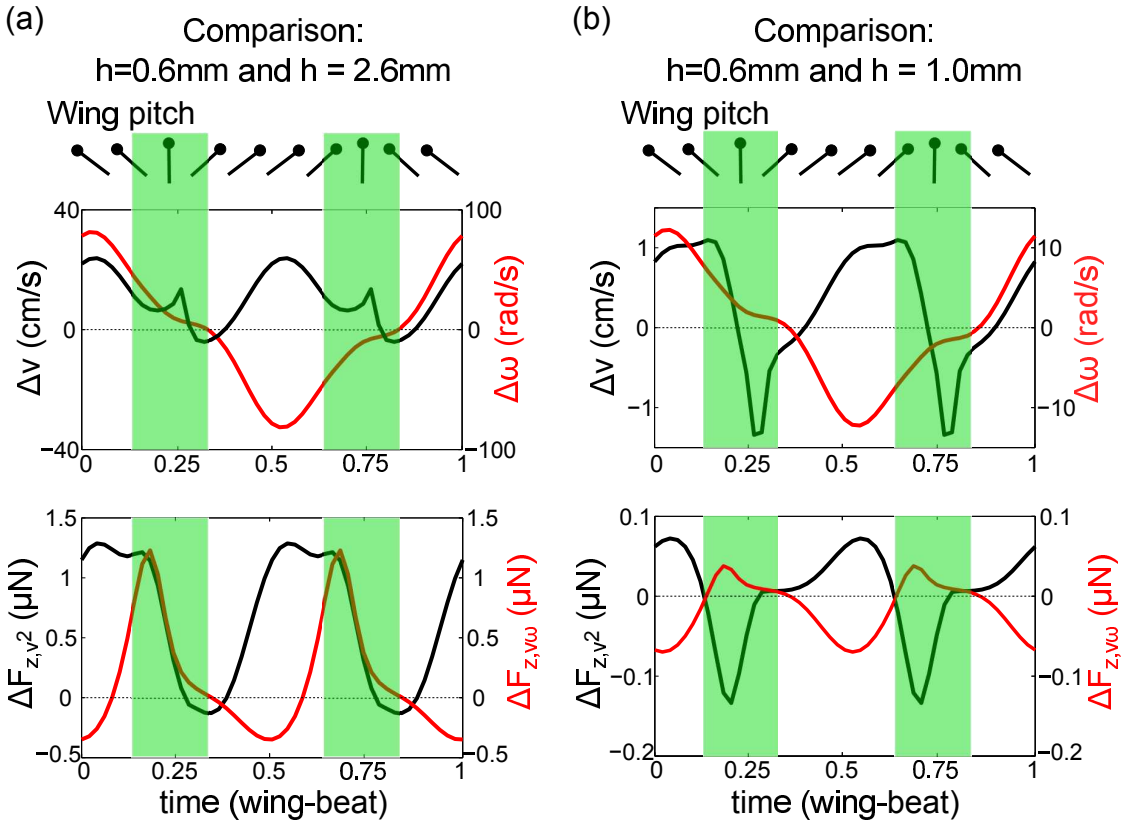

Figure 4.8: Top: detailed difference in wing translational Δv and rotational $\Delta\omega$ velocity during the periodic wing beat. Bottom: the difference in direct lift ΔF_{v^2} and rotational lift $\Delta F_{v\omega}$. Green indicates time of pitch reversal with wing pitch angle indicated above the graphs. (a) Comparing antiresonance h = 0.6mm with far out of resonance h = 2.6mm. The wing velocity is greater at antiresonance during the complete wing beat. As a result h = 0.6mm generates more lift than h = 2.6mm. (b) Comparing antiresonance h = 0.6mm to the maximal lift hinge h = 1.0mm. During the main stroke (white) the velocity is still higher for h = 0.6mm as the antiresonance dictates it should. However, during wing reversal the h = 1mm flight does not have the higher velocity. The forces graph shows that the additional lift during main stroke in F_{v^2} is cancelled by the extra rotational lift in $F_{v\omega}$. At wing reversal the h = 1.0mm flight clearly produces more lift, thus indicating that the maximal vertical velocity should be obtained with h = 1.0mm.

1.0mm a different picture emerges, as displayed in figure 4.8b. It is still true that during the main stroke (white region) the body oscillation reduces the wing velocity and thus Δv is positive. However during wing reversal (green region) the difference is equally great in the opposite direction. Looking at the force graph, the additional lift F_{v^2} of the $h = 0.6$mm fly during main stroke is cancelled out by the additional rotational lift $F_{v\omega}$ of the $h = 1.0$mm fly. Moreover, at wing reversal (green region) the $h = 1.0$mm fly clearly produces additional lift compared to the $h = 0.6$mm fly. Therefore the maximal lift occurs with a wing hinge of $h = 1.0$mm.

In summary, the antiresonance is the main effect that sets the hinge location of the maximal lift. Any oscillation on the body causes a reduction in wing velocity, which means a drop in the lift force $F \propto v^2$. However, near antiresonance a small correction becomes relevant as well. The wing reversal, where the lift force is $F \propto v\omega$, moves the optimal hinge for lift production slightly up to $h = 1.0$mm, the nominal hinge location of a fruit fly.

4.4 Discussion

This chapter examined how the wing hinge location affects the periodic flight state and its stability using 3D flight simulations of the fruit fly. It led to the discovery that the fruit fly achieves the maximal vertical velocity in its periodic flight for the hinge at its natural position, $h_0 = 1$mm. This implies the hinge is located to maximize lift generation. When studying lift generation previous studies focused on the wing shape, flexibility or kinematics [25, 92, 93, 108, 109]. This is the first analysis of the effect of the wing hinge location on insect flight

and it shows that various optimizations that make insect flight possible might still be largely unknown. This result can also be relevant for the design of micro aerial vehicles (MAV's) that rely on flapping wings to remain aloft. To test my results experimentally, one could build various MAV's with different separations between the hinge and COM or it might even be possible to genetically alter fruit fly's, similar to [94], to vary their hinge position.

The maximum lift hinge location is due to an antiresonance in the body pitch oscillation at $h^* = 0.5$mm, see figure 4.6. The body oscillation reduces the wing velocity relative to the air during the majority of the wing stroke. As a result the lift is reduced if the hinge is not located at h^*. The difference between the maximum lift position h_0 and the antiresonance location h^* is due to the complex lift profile generated at wing reversal, see figure 4.7a-b. It appears that for the hinge at h_0 the wing reversal produces additional lift that can compensate for the loss of lift during the main stroke, but the precise mechanism will be the subject of future research.

The new reduced model shows that the antiresonance is the result of a cancellation of the lift and inertial torques on the body. Ellington already observed the body oscillation of various insects [110]. For a crane-fly the body amplitude was large enough that the phase with the wing could be studied and he used that to determine that the crane-fly body oscillation must be predominantly driven by the lift force. One interpretation of this, based on the results here, suggests that the hinge position of this crane-fly is too close to the COM to achieve the highest possible lift. However, that assessment assumes that the recorded flight was a hovering flight, because if the flight was accelerating upwards the additional lift would increase the numerator in equation 4.35, and

thus drive the body oscillation in phase with the lift.

At antiresonance the phase delay between the body and wing is 90° and, interestingly, this particular delay can also be useful for the insect's body pitch control by holding the wings still. Previously a control algorithm for the body pitch was suggested which adjusted the mean of the stroke to correct any deviations [98]. However another possibility would be to hold the wings still and let the natural body sway due to the wing beat correct any mean body pitch deviations. This control scheme would be most effective if the stroke reversal occurs at the same instant as a maximum of the body angular velocity. In that case the fly could achieve any correction to the mean pitch in the shortest amount of time and thus minimize the time when no lift is produced. This control method would thus work well with $\Delta\Phi = 90°$.

The final result of this chapter is the formula for the antiresonance hinge location, equation 4.35, in the reduced model. This result should hold for other species as well, as long as the assumptions on the wing motion and other wing parameters are met. From Greenewalt [111, 112] we know that $m_w\omega^2$ represents the wing muscle force and should be nearly constant across most species. Based on the formula the hinge location is thus expected to scale with the body mass. However, it is impossible to check this, since the data for the separation between wing hinge and COM is not readily available for a range of species. Future research should attempt to document the location of the wing hinge relative to the COM, such that this prediction for the wing hinge position can be empirically tested.

CHAPTER 5

EVOLUTION FROM FOUR- TO TWO-WINGED FLIGHT REDUCES POWER USAGE [1]

Two winged insects are believed to have developed from four-winged flyers during their evolution [27]. The four-winged dragonfly (Odonata) is one of the oldest flying insects [26, 113] and during its flight the body is horizontal and the wings stroke asymmetrically along an inclined plane [114, 115]. In contrast, later developed insects generally have two wings [116] and fly with their body pitched up vertically, while the wings move symmetrically along a horizontal stroke plane [117]. Although fossil records and genetic studies can provide clues about this evolutionary process, very little is known about the flight kinematics during the transition. In this chapter we will show that during the evolutionary transition to two wings the flight style naturally switches from horizontal to vertical. This change must be combined with a switch from an asymmetric to a symmetric wing stroke in order to maintain flight. Moreover, both changes occur during a sharp transition directly after switching from hind wing to front wing adjustments.

The evolution of two-winged flight likely proceeded through a reduction of the size of the hind wings. An example is the mayfly, which is closely related to the dragonfly and has significantly smaller hind wings [118]. Moreover, genetic studies of Diptera indicate that a mutation on the Ubx gene leads to the development of an additional wing pair below the main wings [119,120]. Initially, the reduced hind wing area likely led to increases in the hind amplitude in order to compensate [121], however when the wings become too small this will fail. The

[1] A manuscript is in preparation.

front wing must at that point take over and adjust for any further loss of hind wing lift. This will be the the evolutionary scenario discussed here.

For this study we use the 3D computer flight simulator from the previous chapter again, after adding an additional set of wings. The four-winged flyer model has a morphology based on a dragonfly and to simulate the evolution the hind wing area is systematically reduced. The required adjustments to the wing motion are determined by an optimization algorithm that fixes the steady state velocity as the hind wing is trimmed. The Floquet analysis of the steady states is expanded and, besides stability, the power consumption is also computed. Our results indicate that the evolution of two-winged flight was likely a sudden development that required a significant adjustment of the front wing muscles. In addition, the driver behind the transition was likely the advantage of increased energy efficiency.

5.1 Modeling four-winged flight

The 3D flight simulation model, explained in the previous chapter, can also be used for studying the evolutionary process from four- to two-winged flight. The model was already defined using a variable number of wings, thus we only need to specify additional parameters for the extra wings. To model the evolutionary process, the size of the hind wings can be reduced step by step. Once the hind wings have a span just 10% of the original length, the model effectively only has two wings left. The periodic flight state and its stability are determined using Floquet analysis exactly as before. A new element to the analysis is the computation of the power usage during flight. First, the parameters will be

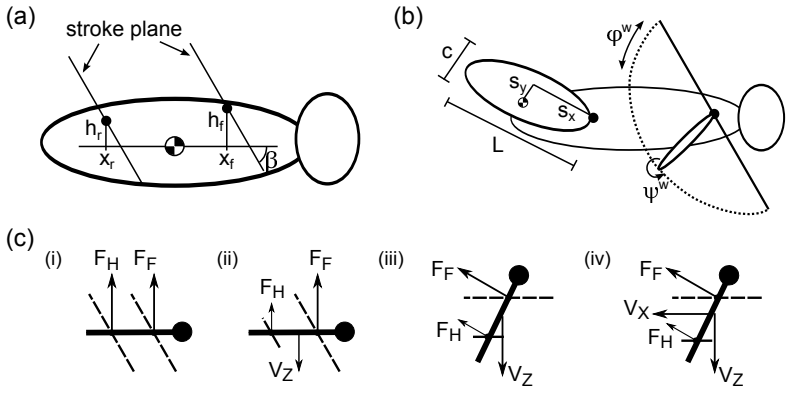

Figure 5.1: (a) Wing hinge locations on the dragonfly body. Front wing is located x_f ahead of the body COM and h_f above it. Similarly the hinge wing is positioned x_r before and h_r above the COM. The wings move along a stroke plane that is tilted by an angle β with respect to the horizontal. (b) The wings have a span length L and chord length c. The wing COM is located at s_x along the span and s_y along the chord away from the hinge. Finally the stroke angle ϕ^w along the stroke plane and the wing pitch angle ψ^w are indicated. Values for each parameter are given in the text. (c) Schematic of flyer forces. (i) Normal flight has the front and hind wing producing balanced lift keeping the body horizontal. (ii) A smaller hind wing reduces the hind lift, leading to a falling flyer. This can be compensated by increasing the hind amplitude. (iii) Barring any compensation, the falling velocity causes drag on the wings. The larger front wings experience more drag and rotate the body pitch up. (iv) The rotated body directs the lift force behind the fly causing horizontal acceleration. At this point the correction requires wing pitch rotation, rotating the lift force back up against gravity, and an increase in front stroke amplitude to mitigate the falling velocity.

listed and then the power computation will be explained.

Parameters of the flyer model with four wings

The four-winged model parameters are based on measurement of a dragonfly [122], see table 5.1. Figure 5.1 shows a sketch indicating each parameter, with

Table 5.1: Summary of the default (Δ = 100%) dragonfly morphological parameters. Δ is the scale parameter that sets the size of the hind wings during modeled evolution to two-winged flight. Altering Δ changes the hind wing span and chord, as well as the hind s_x and s_y.

Dragonfly morphology					
m_{body}:	340 mg	Front m_{wing}:	3.5 mg	Front h:	4 mm
Body length:	36 mm	Front wing span:	32 mm	Front s_x:	16 mm
Body width:	5.2 mm	Front wing chord:	8 mm	Front s_y:	2.4 mm
Front wing x:	5.5 mm	Hind m_{wing}:	3.6 mg	Hind h:	2 mm
Wing separation:	5.9 mm	Hind wing span:	33 mm	Hind s_x:	16 mm
Stroke plane β:	51°	Hind wing chord:	11 mm	Hind s_y:	5.6 mm

body length 36mm, body width 5.2mm, body height 7.3mm and body mass 340mg. The front wings are located at x_f = 11mm and h_f = 4mm, and have dimension L_f = 32mm and c_f = 8mm. The rear wings can be found at x_r = 3.2mm and h_r = 2mm, and for Δ = 100% are L_r = 33mm long and c_r = 11mm wide. Δ is the scale parameter that sets the size of the hind wings. When Δ = 50% both L_r and c_r are half their original size, thus making the wing area a quarter of its original. The vector from hinge to wing COM is given by s_x = 16mm and s_y = 2.4mm for the front and s_x = 16mm and s_y = 5.6mm for the rear. When changing Δ, s_x and s_y of the hind wing are also altered. This ensures Δ sets the size of the hind span, while the wing retains its aspect ratio and connection point with the body.

The wing motion of the front and hind wings can be described using the same equation as for the fruit fly, see equations 4.12-4.14. However, there are some notable differences. All wings move along a rotated stroke plane, with

Table 5.2: Summary of the default dragonfly wing motion parameters. Note that the front and hind stroke are 180° out of phase and move along an stroke plane inclined at 51° with respect to the longitudinal body axis.

Dragonfly wing motion					
Frequency :	40 Hz	Wing pitch ψ_0	120°	Shape parameter K	1e-16
Front stroke ϕ_m:	30°	Wing pitch ψ_m	50°	Shape parameter C	1e-16
Hind stroke ϕ_m:	32°	Wing pitch ψ_δ:	90°	$\theta^w(t)$	0

$\beta = 51°$ the angle between the body longitudinal axis and the stroke direction. Moreover, the front wing stroke ϕ^w has a phase difference of 180° with respect to the hind wings. The full list of wing motion parameters is given in table 5.2. The wings flap at a frequency of 40Hz and have an amplitude of 30° or 32° for the front and hind wings respectively. The wing pitch is also different from the fruit fly, at $\psi_0 = 120°$ for both wings.

Power usage during flight

The power consumption during flight is computed through integration of the drag losses, adding the change in potential energy and averaging the sum over a single wing beat. Any mention of power P implicitly refers to the wing beat averaged power $< P >= \frac{\int_0^T P(t)dt}{T}$, with T the wing beat period. The first step in the power computation is to integrate the drag losses on the wings. The drag force $\vec{F}_d$ and torque $\vec{\tau}_d$ are determined in the simulation from equation 4.16. The power losses due to drag are then given by:

$$< P_{loss} >= \frac{\int_0^T \left(\vec{F}_d \cdot \vec{v} + \vec{\tau}_d \cdot \vec{\omega}\right) dt}{T}. \tag{5.1}$$

In this equation $\vec{v}$ and $\vec{\omega}$ are the wing velocity and angular velocity respectively. On top of this the fly is moving in the gravitation potential of earth, which means it loses or gains potential energy

$$< P_{grav} >= m_t g \frac{z(T) - z(0)}{T}. \tag{5.2}$$

Here m_t is the total mass and the fraction denotes the average change in vertical position during the wing beat. Note that, due to the use of periodic flights, the kinetic energy does not change. Therefore the total power consumption of the flyer is the sum of these two terms $P = P_{loss} + P_{grav}$.

Required wing adjustments

During the transition, when the hind wings are diminished, adjustments to the wing strokes are required to maintain flight. The effects of smaller hind wing area are explained in figure 5.1c. During normal flight before the transition (i) the front and hind wings are producing balanced lift, which keep the body of the dragonfly horizontal. Initially when the hind wings are reduced (ii), the lesser hind lift leads to a falling flyer. This can be compensated by increasing the hind amplitude. Balancing the hind lift against gravity, provides the first adjustment option.

The other option requires adjustments to the front wing. If the hind wing is not or cannot be adjusted (iii), the flyer starts falling. This downward velocity causes drag on the wings. The larger front wings experience more drag and rotate the body pitch up towards vertical. At this point (iv), the rotated body directs the lift force behind the fly. This leads to horizontal acceleration. To correct this requires a front wing pitch rotation, thereby rotating the lift force back up

against gravity. Finally, an increase in front stroke amplitude can mitigate the falling velocity and the same initial flight velocity can be maintained.

5.2 Simulation of the evolutionary transition

In the simulation we initially maintain a constant vertical flight velocity v_z by increasing the hind wing amplitude ϕ_{hind}, see figure 5.2 red region. While $\Delta = 100 - 70\%$ the steady state flight has the body horizontal, resembling dragonfly flight with body pitch $\theta \approx 10°$. At $\Delta = 70\%$ the required hind amplitude has increased to 90° at which point it is unrealistic to increase the stroke amplitude further as the wings now touch at the top and bottom of the stroke. For each Δ the hind amplitude was found using an optimization algorithm that changed ϕ_{hind} to minimize changes to v_z.

The next stage of the evolution to reduce the hind wings involves changes to the front wing pitch and stroke amplitude (blue region). Interestingly the flight style changes rapidly between $\Delta = 70 - 60\%$, as the body pitches up and the stroke plane becomes horizontal. With the rotation of the stroke plane the wing pitch ψ must be counter-rotated by 40° to keep the lift force directed upwards. The stick plots in figure 5.2 show the wing pitch as it changes from asymmetric for the inclined plane to symmetric for the horizontal plane. Again, at each Δ an optimization algorithm found the ψ and ϕ_{front} that minimized changes to the periodic state velocity v.

During the transition from four to two wings the power P required to sustain flight is reduced. During the initial phase $\Delta > 70\%$ of increasing hind wing amplitude the power consumption increases, but after the transition to front

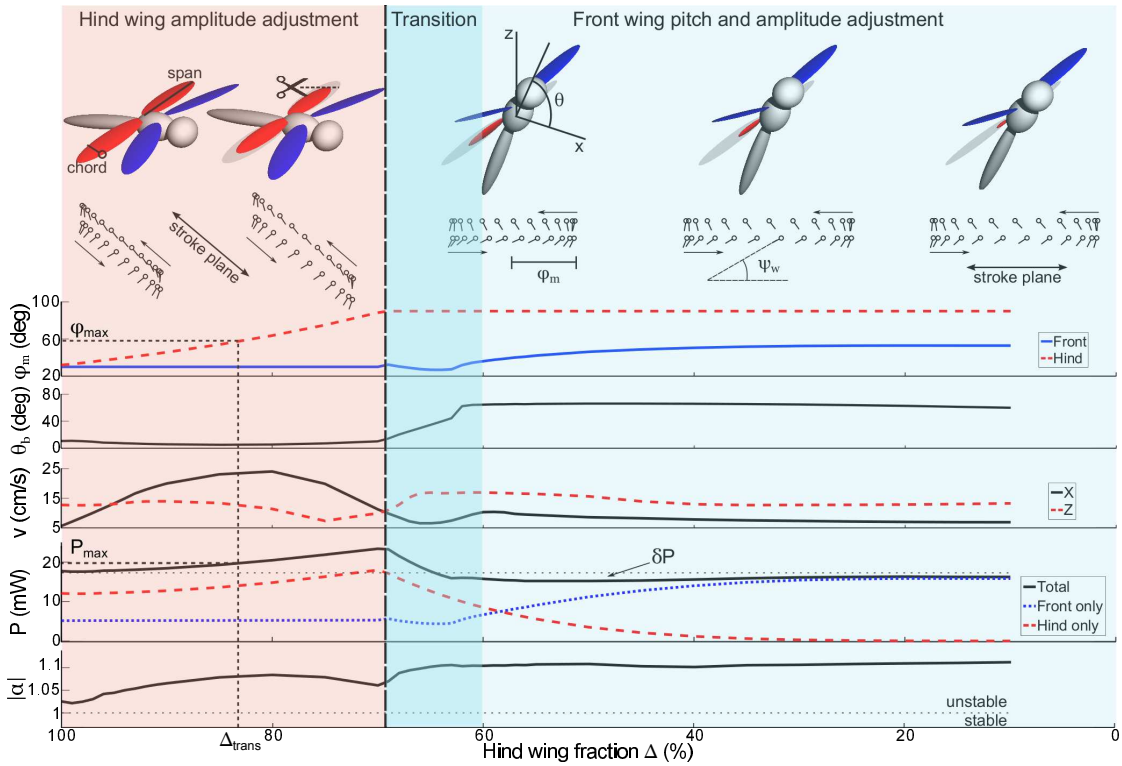

Figure 5.2: Evolution of two-winged flight by reducing the fractional size Δ of the hind wings (red) of a four-winged flyer. Initially, for $\Delta > 70\%$, the hind wing stroke amplitude ϕ_{hind} can increase to compensate the loss in wing area. The body pitch θ remains horizontal and the stroke plane remains inclined in this phase. The next phase (blue) the front wing pitch and amplitude are adjusted to maintain similar flight velocities v. A quick transition (dark blue) occurs at $\Delta = 70 - 60\%$, when the body pitches up and the stroke plane becomes horizontal. At this point the wing pitch ψ must be rotated to counter the stroke plane rotation. During the transition the power usage P drops, indicating two-winged flight increases energy efficiency. During the remaining hind wing reduction, $\Delta < 60\%$ the front amplitude must be increased slightly, but the flight style and power usage remains nearly the same. The stability $|\alpha|$ of the steady state flights changes only slightly during the evolution, becoming more unstable as Δ decreases.

wing stroke adaptations the power drops quickly. Power loss at the individual front and hind wings follows their respective stroke amplitude. Once the hind stroke no longer increases the power loss for them drops rapidly, since power is proportional to the wing area. The total power, initially at 17.7mW, drops by $\delta P = 1.5$mW for small hind wings. This drop in power consumption is likely the driver behind the evolution from four- to two-winged flight.

The flight stability is only slightly changed during the transition and remains in the unstable regime throughout. The initial dragonfly-based flyer is passively unstable $|\alpha| > 1$. $|\alpha|$ indicates the multiplicative growth factor per wing beat of deviations from periodic flight. Transitioning to two-wings leads to an increase in $|\alpha|$, thus making the flight somewhat more unstable and facilitate faster turning. It seems likely that the control circuitry capable of stabilizing four-winged flight could be tuned to also deal with the unstable two-winged flight. Changes to flight stability are thus unlikely to significantly effect the transition process.

The point of the transition from hind to front wing adjustments can be at a Δ higher than 70% without significantly effecting the results. The hind wing muscle might have a lower amplitude limit ϕ_{max} than 90°, or the power usage might be limited P_{max}. In both cases a reduced hind wing could be initially compensated by increased hind amplitude, allowing the flight style and front wing muscle to remain the same, creating a robust flyer. However, once the amplitude or power limit is reached the front wing would have to adapt to further reduction of the hind wing area. At that point the flight style will still quickly change from a horizontal to a vertical body, shifting the transition in figure 5.2 (dark blue region) to a higher Δ value, while maintaining its defining characteristics.

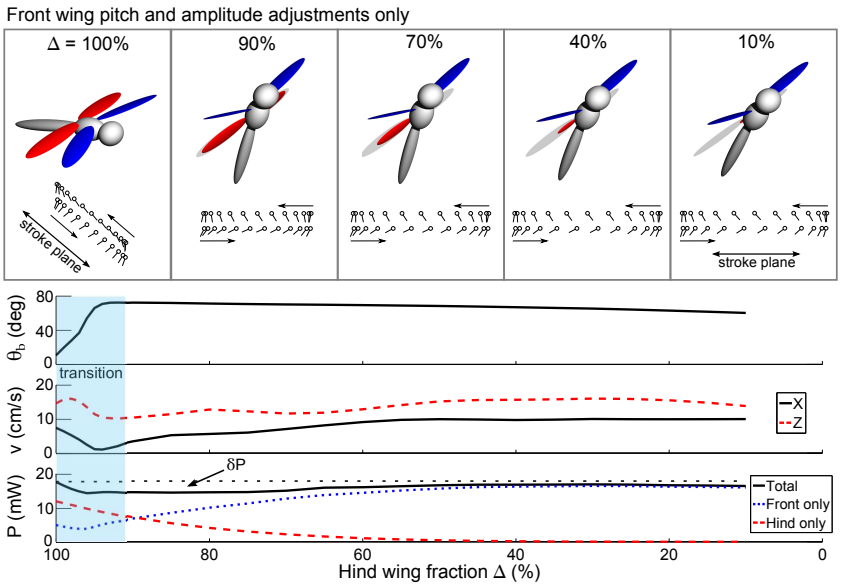

Figure 5.3: Transitioning to front wing adjustments at $\Delta = 100\%$. The body pitches up rapidly between $\Delta = 100-90\%$. The stroke plane becomes horizontal and the wing pitch is rotated to keep the lift directed against gravity. The power consumption also drops similar to the case with hind wing adjustments. The large degree of similarity between the two transitions suggests that the hind wing adjustments can only change the Δ value at which the transition occurs, not its characteristics. Below $\Delta = 90\%$ the only change to the wing stroke is the increase in front amplitude to compensate for the lost hind wing area. The adjustments to front wing pitch and amplitude were found by optimizing for a constant velocity.

Figure 5.3 shows the limiting case where the transition to front wing adjustments starts immediately at $\Delta = 100\%$. The body pitch shoots up and the power required to maintain the steady state flights drops. The pictures of the fly confirm that the body becomes vertical and the stroke plane horizontal. The wing pitch needs to be adjusted similarly to the previous case and counter the stroke plane rotation. Overall the same shift in flight style occurs, but at a higher Δ. Therefore adjustments to the hind wing amplitude can delay the change in flight style, but they cannot stop it from happening.

5.3 Conclusion

The results presented here indicate that the evolution from four- to two-winged insect flight was likely a sudden development, as indicated by the rapid transition between flight styles. By changing Δ just 10% the body pitch changes from horizontal to near vertical, the stroke plane rotates from inclined to horizontal and the wing pitch becomes symmetrical. These are significant changes to the front wing and they likely required a mutation on the muscle to make possible. We noted that, once this mutation occurs and the flight style is altered, the flyer's power usage is reduced. This lower power consumption during flight likely provides an evolutionary advantage, since it reduces the amount of food that needs to be captured to sustain flight. However, the importance of this reduction in power is still somewhat puzzling, since four-winged dragonflies have not gone extinct and live alongside a majority of two-winged flying insects.

The exact moment the transition occurred can be altered by extending the use of hind wing adjustments to compensate for lost wing area. This provides the dragonfly with a robust design. If the hind wing area is reduced due to injury or natural variation it can recover by altering the wing stroke. However, this does come with the expense of additional power consumption. However, there is a clear limit to how long this can be sustained. Assuming no power restrictions that limit is $\Delta = 70\%$. This provides a clear prediction for Nature's flyers: if the hind wings of a four-winged flyer are smaller than 70% of the front wings, than its natural flight style should have the body pitched vertically.

The previous two chapters looked at the effect of evolutionary optimization

on insect flight. The focus was first on the location of the wing hinge relative to the flyer's COM. This parameter was tuned to a wing-body antiresonance, with the result of maximizing ascending speed. Here we found that the transition to two wings reduces the power consumption of the flyer. Both are examples of simple rules that emerge out the evolutionary process of random genetic variation.

In addition, this chapter 5 shows that the evolution of different features of an organism are closely connected. Reducing the wing size cannot be done without significant consequences on other body parts. In order to maintain flight, corrections to the front wing pitch and amplitude are required. It is likely that other changes to the insect are also needed. For example, when the body suddenly pitches from horizontal to vertical the location of the eyes on the head will also need to be adjusted. All these adjustments show the complexity of the system and make it remarkable that increasing ascending speed or lowering power usage are possible through genetic optimization.

The final chapter of this thesis will combine all the previous chapters and study how control laws develop for stabilizing insect flight. We will study whether a human can learn how to control insect flight and whether they develop the same laws that already exist in an insect brain. To do this, the first step is to build a real-time interface that allows a person to control the simulated insect.

CHAPTER 6

HUMAN CONTROL OF SIMULATED INSECT FLIGHT

The ancient story of Icarus tells us that humans have for ages looked at birds and insects and wondered if perhaps they too could soar the skies by flapping wings, however all attempts so far have resulted in failure [123]. Scientific research into flapping flight has laid bare the intricacies involved in producing the required lift [102,108,124] and controlling the stability [100,125,126]. Now, using human controlled computer simulations, we can safely break up the problem of learning how to fly and discover if humans are able to learn how to stabilize flapping flight. This chapter will describe the attempt to construct an intuitive interface for controlling the simulated insect. The initial results show it is indeed possible to learn to generate lift and stabilize flight in a realistic insect flight simulator by flapping a wing controller.

Many experiments have been performed to understand motor learning in humans [127,128]. These experiments show the flexibility of the human mind to learn new tasks and it thus seems likely that we should also be able to master the skill of controlling insect flight. In my experiments the test subjects will have to rely on visual information alone for their learning feedback [129,130]. The available information to determine the needed corrections thus differs slightly from flying insects which can have highly tuned sensors to measure their stability, such as the halteres on a fruit fly [95,97].

The difficulty of the control task can likely be set based on the stability of the particular insect. One question of interest is what technique a human develops to stabilize insect flight and whether it is similar to the actual methods used by those same insects [98,100]. Based on the results from the previous two chapters,

it would be possible to help with the flight control, for example, by raising the wing hinges or by using a stable dragonfly instead of the unstable fruit fly.

This chapter will first explain how to construct the interface for the control of the insect flight simulator, where a human can move a model wing to provide the insects wing motion and receive fast visual feedback on the resulting flight. Afterwards, the initial system test will be discussed, which show that the setup is working properly and that it is possible to learn how to fly as a fruit fly. Next, the first experiments can be described, which focused on controlling the flights of dragonflies with rear wings of various sizes. The similarity with the simulations of chapter 5 allow for a comparison of the results. We will close with an outlook on possible future experiments that can be performed with this new system.

6.1 Building an interactive flight simulator

The construction of the interactive flight simulator is the culmination of several projects in Jane Wang's group by various people. The basis of the simulator is the insect flight model explained in chapter 4, developed over many years and first coded into C++ by Song Chang. As previously mentioned, I substantially improved the speed of this code. In addition, I connected it to Matlab and built a GUI for controlling the experiments. The input for the flight simulator is provided by a physical wing controller, tracked using Vicon infrared cameras (Vicon Motion Systems, Oxford, UK). Adam Sorrin was the first student to connect the Vicon system to our lab computers and extracted raw data from its pipeline using C#. The Vicon system was first used by another student, Kevin

Chen, to test the real-time conversion of tracked motion from the physical controller to the computer. He used this to study a simple 1D hoverer. I expanded his work to three dimensions, added noise smoothing, and combined all these components into the human controlled insect flight simulator.

Here we will describe each of the pieces that went into the development of the interactive flight simulator. First, we discuss the construction of the wing model and provide details on how its orientation is determined by the Vicon camera system. A sequence of these orientations is recorded as a quaternion time series. The next step of the process smooths the noise out of the time series and takes derivatives to determine the angular velocity and acceleration of the wing model. This provides the required input for the wing motion in the 3D flight simulator. Finally, the problem of different time scales will be addressed, because a human cannot comfortable flap their arm at normal insect wing beat frequencies. After putting it all together, the end result can best be described as a physically realistic video game, where the player can fly any insect he wants by flapping around a controller to provide the input wing motion.

Tracking the wings

The motion of the wings is recorded from a left and a right model wing, constructed using TinkerToy (K'Nex, Hatfield, PA, US). The basis of each model wing is an orthogonal frame with infrared markers attached to the end of each of the three axis, see figure 6.1a. The markers are tracked using 3 Vicon MX3+ cameras, which operate at 50Hz. The Vicon software reconstructs the physical marker location from the images and passes these resolved positions through

a TCP/IP pipeline on to a home-written algorithm. This algorithm has to go through a number of steps before the data is ready to be used in our flight simulation.

The locations of the three markers, $\vec{x}$, $\vec{y}$ and $\vec{z}$, define an orthonormal matrix $O(t)$ which encodes the orientation of the model wing at time t. This matrix is created by taking the difference vectors between the markers, $\vec{u} = \vec{x} - \vec{y}$, $\vec{v} = \vec{x} - \vec{z}$, $\vec{w} = \vec{y} - \vec{z}$, and using the cross product to create orthonormal vectors, $O(t) = \left(\frac{\vec{u}}{|u|}, \frac{\vec{u}\times\vec{v}}{|u||v|}, \frac{\vec{u}\times\vec{w}}{|u||w|}\right)$. This matrix encodes the instantaneous orientation of the wing in the Cartesian coordinate system used by the Vicon software, which is determined when the cameras are calibrated.

In order to make the control of the wings feel intuitive the orientation of the wing in the lab should match the wing on the screen. This is achieved by presenting an image of an upright insect with the wings in a known position before the start of the simulation. The human participant is asked to match the position shown on screen, which is used to align the wings. This records $O(t)$ of the aligned wings at $t = 0$. At any future time t, the rotation from the aligned position to the current position is now given by the product $O(t)O^{-1}(0)$.

Simultaneously the algorithm ensures the rotation axis in the simulator are aligned with the model wing axis. For this the first three markers on the wing are attached along the span, chord and upward direction. The locations of the three markers give, using trilateration [131], the origin of the orthogonal frame. The three vectors from the origin to each of the marker position define an orthonormal matrix P, which is recorded at wing alignment. Finally, the rotation matrix R of the wing at time t with respect to its aligned position, specified in

the coordinate system of the wing, is given as

$$R(t) = P^{-1}O(t)O^{-1}(t = 0)P. \tag{6.1}$$

One advantage of this method is that it allows for easy addition of markers to the model wing, which helps to avoid occlusion problems. To define the matrix P a single set of three markers must be positioned on the rotation axis of the model, but only at $t = 0$. However, $O(t)$ can be defined using a different set of markers. As long as the $O(t = 0)$ matrix is recorded for each combination of three markers and at least three markers are visible at any one point, it is possible to reconstruct the rotation state of the wing at any time t. The wing model used in the lab has 5 markers, which was enough redundancy to make for smooth wing tracking.

The final step in the tracking algorithm converts rotation matrix $R(t)$ into a quaternion. If multiple sets of three markers are visible, a quaternion for each is computed and then averaged to reduce noise in the measured wing quaternion. Quaternion averaging is done by converting the quaternions to axis-angle representation and adding the axis vectors weighted by the angles. After wing alignment, which defines $t = 0$, the algorithm produces a discrete time series of quaternions $\mathbf{q}_{raw}(t_i)$ at the camera rate of 50Hz.

Quaternion smoothing

The numeric integration routine in the flight simulator requires a continuous evaluation of the wing orientation and its derivatives, thus the previous discrete set $\mathbf{Q}(t_i)$ is insufficient. However, before interpolating and differentiating, it is

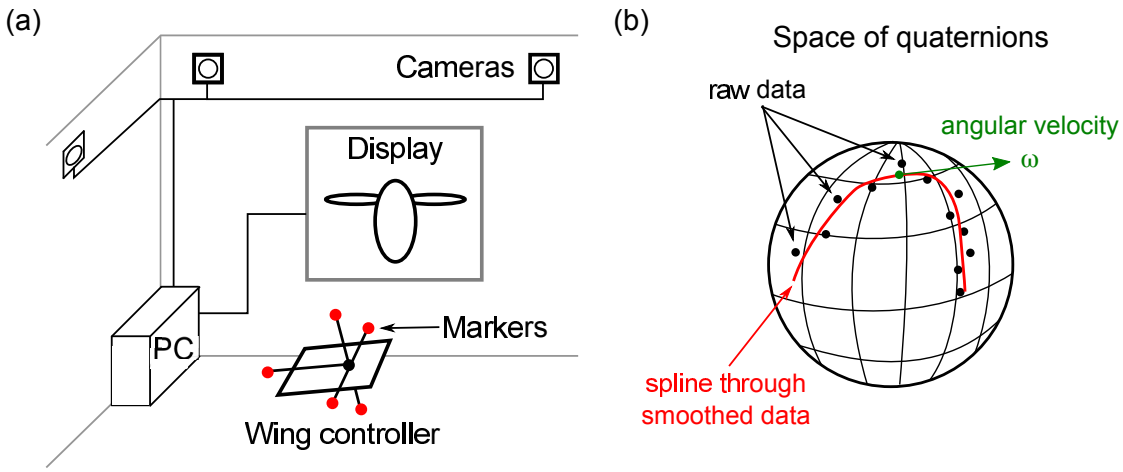

Figure 6.1: (a) Schematic setup for the human controlled insect flight experiments. The wing controller is a cardboard sheet with an orthogonal frame attached to it. Each end of the frame has a infrared marker (red dots) on it. The location of the infrared markers are recorded using three Vicon cameras hanging on the wall and the data is passed onto the PC. After processing the flight is displayed on a screen as feedback to the test subject. (b) Processing of the wing model input occurs in the space of quaternions, here represented as a sphere to indicate the curvature. Raw data (black dots) indicating the current wing orientation is computed at each recorded camera frame using each set of three orthogonal markers. Through the data a smoothed spline (red line) is fitted. Along this line it is possible to determine the local wing angular velocity (green arrow) as the tangent vector to the spline. This information is passed on to the insect flight simulator, described in chapter 4, to determine the effect of the wing motion on the flight. See text for details.

prudent to ensure noise is removed and the time series is smooth. (figure 6.1b) For this the last $N = 15$ recorded frames of the time series are smoothed using a technique described in [132].

The smoothing filter is a gradient descent algorithm that minimizes the en-

ergy function

$$F(\mathbf{q}_{raw}) = \sum_{i=1}^{N} \| \log(\mathbf{q}_i^{-1}\mathbf{q}_{raw}(t_i))\|^2 + \alpha \sum_{i=1}^{N-1} \| \log(\mathbf{q}_i^{-1}\mathbf{q}_{i+1}) - \log(\mathbf{q}_{i-1}^{-1}\mathbf{q}_i)\|^2 \tag{6.2}$$

Here the quaternions $\mathbf{q_i}$ are to be varied by the gradient descent algorithm in order to minimize F. Also note that all products in this and the next section are between quaternions and thus noncommutative. The first term is a measure for the distance between the raw data and the smoothed points. The second term measures the smoothness of the quaternion curve. The coefficient $\alpha = 0.5$ allows us to set the relative importance of each term. The time series of filtered quaternions that minimize F will be denoted by $\mathbf{Q}(t_i)$.

A delay of two frames was introduced here since smoothing on the interior of the interval is more accurate than on the boundary. When a new orientation is recorded by the cameras it is added at the end of the 15 frame buffer. However after the noise filter, the quaternion used to indicate the wing position on screen for the human participant is at position 13. This provides a smoother wing motion on screen at the cost of a 40ms delay. This delay does not appear to be noticeable.

Quaternion interpolation and differentiation

At this point the algorithm has determined a smoothed but discrete time series of quaternions $\mathbf{Q}(t_i)$. However the simulation, in particular the ODE solver, requires the evaluation of the wing motion at any time slice within the integration interval. Therefore interpolation of the quaternion time series is needed. The interpolation must be based on very general B-spline functions, because the human input cannot easily be restricted to any given set of functions. The

algorithm explained in [133] is used and extended to include calculation of the first and second derivatives.

Before it is possible to discuss quaternion interpolation, the exponential and logarithmic function for quaternions must be explained. The following explanation will assume some understanding of differential geometry. The quaternions represent rotations in space, and thus in mathematical terms form the manifold $SO(3)$. The logarithmic and exponential functions are defined as maps to and from the tangent space as is common in differential geometry. The tangent space of $SO(3)$ is $\mathbb{R}^3$, which is the space of local angular momentum vectors $\vec{\omega}$. It thus follows that $\vec{\omega} = \log(\mathbf{q})$ and $\mathbf{q} = \exp(\vec{\omega})$, where $\vec{\omega}$ should be considered as the angular velocity that after unit time leads to a rotation about $\mathbf{q}$. This makes it possible to define the arbitrary power of a quaternion $\mathbf{q}^x = \exp(x \log(\mathbf{q}))$.

Quaternion interpolation is an extension of the regular cubic B-spline interpolation to the curved quaternion space. The B-spline quaternion curve $\mathbf{q}(t)$ is defined by

$$\mathbf{q}(t) = \mathbf{q}_{-1}^{\tilde{B}_0(t)} \prod_{i=0}^{N+1} \left(\mathbf{q}_{i-1}^{-1}\mathbf{q}_i\right)^{\tilde{B}_i(t)} \tag{6.3}$$

where

$$\tilde{B}_i(t) = \sum_{j=i}^{N+1} B_j(t) \tag{6.4}$$

with B_i the 4th order basis functions of regular cubic B-splines. The $\mathbf{q}_i$ are the quaternion spline control points which are, just as in the regular B-spline case, determine by solving a set of equations

$$\mathbf{Q}(t_i) = \mathbf{q}_{i-1}\left(\mathbf{q}_{i-1}^{-1}\mathbf{q}_i\right)^{\frac{5}{6}}\left(\mathbf{q}_i^{-1}\mathbf{q}_{i+1}\right)^{\frac{1}{6}}, \tag{6.5}$$

with the boundary condition taken as a natural spline, which means

$$\mathbf{q}_{-1} = \mathbf{q}_0\left(\mathbf{q}_0^{-1}\mathbf{q}_1\right)^{-1} \quad \text{and} \quad \mathbf{q}_{N+1} = \mathbf{q}_N\left(\mathbf{q}_{N-1}^{-1}\mathbf{q}_N\right). \tag{6.6}$$

Due to the curvature of the quaternion space, i.e. multiplication is noncommutative, the control points in Eqs.6.5 and 6.6 must be found using a recursive solver. The algorithm uses 10 iterations of recursive solving, which provided a fast and accurate determination of the control points. This matches the convergence results mentioned in [133].

The resulting function $\mathbf{q}(t)$ provides a smooth quaternion curve which passed through the recorded wing orientations and can be evaluated at any time within the first and last recording. The angular velocity and acceleration of each wing are related to the time derivatives of $\mathbf{q}(t)$. After deriving $\dot{\mathbf{q}}(t)$ and $\ddot{\mathbf{q}}(t)$ from equation 6.3, the angular velocity and acceleration of the wing relative to the body are given by

$$\omega^r = 2\mathbf{q}^{-1}\dot{\mathbf{q}} \quad \text{and} \quad \beta^r = 2\mathbf{q}^{-1}\ddot{\mathbf{q}} \tag{6.7}$$

At this point the angular velocity and acceleration vector can be extracted from their respective quaternions by taking the imaginary part. The algorithm now produces continuous functions for the orientation, $\mathbf{q}(t)$, angular velocity, $\vec{\omega}^r(t)$, and angular acceleration, $\vec{\beta}^r(t)$, for each of the wings relative to the body. This information is passed into the flight simulator which can determine how the wing motion is affecting the body.

Running the simulation in real-time

The wing model tracking algorithm can be combined with the 3D flight simulator of chapter 4 to create a real-time flight simulator with an intuitive interface for human control of the flight. The input wing motion can be any motion that

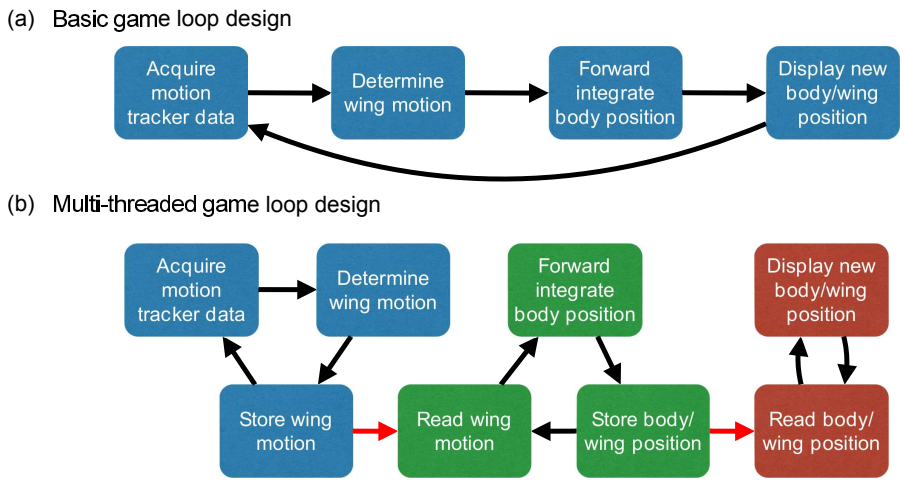

Figure 6.2: Flowchart for the algorithm for the human controlled insect flight experiments. Black arrows indicate execution and data flow, red arrows indicate only data flow. (a) The basic idea of the game loop design setup, which is repeated as long as the experiment is running. Problems arise because it is unclear how much time has passed when the loop returns to acquire new tracking data. (b) Improved loop design using three different execution threads (different colored boxes). This design avoids skipping a frame of tracker data if the flight simulator had not finished computing yet. The first (blue) thread is short and will buffer frames if subsequent code is not ready yet. New data, when recorded by the cameras is immediately time-stamped and it is now known how long it takes until the data is displayed. This allows the code to guarantee no frames from the Vicon cameras are skipped and that the delay between recording and display is between 60 and 80ms.

can be performed in the lab. The flight model then determines how the insect body is affected by this wing motion. To complete the feedback cycle, a display in the lab shows the tracked wing position and computed body position in a 3D simulation of the insect. With this feedback the human participant can evaluate his or her own flying ability and attempt to correct deviations from the intended flight.

For intuitive control the system has to respond fast to the provided wing mo-

tion and therefore the flight model has to compute fast to avoid any perceived lag. Since the camera system is running at 50Hz, it provides new wing motion data each 20 ms. The flight model should return the result of a new frame of the motion before the next data becomes available 20 ms later, while maintaining reasonable simulation accuracy. To achieve this the code, written in C++ and compiled as a mex-library, was setup in a similar style to the code design for video games, see figure 6.2a. As long as the simulation is active a game loop is running, first it request the user input, then it performs the simulation update and finally it passes the result on to the display function. The display function is handled by Matlab, which also makes it easy to save and analyze the data.

The basic game loop design is not sufficient for our experiments, since it is impossible to guarantee that each data frame recorded by the Vicon system will be used. If the simulator or the display function required too much time a frame might be overwritten and lost. To circumvent this problem an improved multi-threaded game loop design is used, see figure 6.2b. Three separate threads are responsible for the wing motion, flight simulator and display. With this design no data frames are skipped, because the first loop is guaranteed to execute in less than 10ms. Moreover, the data is instantly time-stamped and the delay can be computed when the updated insect is shown on screen to check the delay is acceptable. The last improvement required is in the plotting routine of Matlab, which normally goes through a Java implementation layer. This is too slow for our purpose and the display function is configured such that it directly interfaces with the video card. With these optimization the total delay between moving a wing and seeing the result on screen is around 70 ms, 40 ms of which we introduced to improve the wing motion smoothing, 20 ms to compute the flight model and 10 ms for updating the displayed graphics.

Required time dilation for comfortable arm movement

Finally, there is the problem that a human subject cannot move their arm at the frequency at which insects are flapping their wings. For comfortable movements, the arm is limited to back and forth flapping with a frequency around 0.5Hz, perhaps reaching 0.8Hz. For fruit flies the wing beat frequency is around 250Hz, while for dragonflies 40Hz. In addition, for the fruit flies the stroke amplitude is on the order of 70 degrees and humans cannot comfortably move their arms by 140 degrees. The solution is to introduce a time dilation factor between the lab and the simulation. This time dilation factor is set prior to the experiment and can be based on the particular insect currently simulated.

Experimentally it turns out that for the fruit fly a time dilation factor of 600 works well. Similarly for the dragonfly a time dilation factor of 100 is used. This time dilation is implemented by slowing down the speed at which time progresses inside the flight simulation. As a result, time series from each experiment can be viewed on two time axis, the human lab time or the insect simulator time, see 6.3. With this last feature the construction of the human controlled insect flight simulator is complete and can be used to collect data.

6.2 Successful recordings of human flight data

We collected the first human flight data using the completed interactive insect flight simulator. The initial data provides a confirmation of the correct functioning of the equipment and code. We will look at the raw data of the wing beat that the human is performing and the response to it by the fruit fly. In the

15 recorded fruit fly trials, I was the test subject performing the flight. Various (prospective) undergraduate group members also tried to fly using the machine. These trials were not recorded, but they provided some clues as to the kind of wing beats and flights to expect during full trials.

Later, the system is used to study the human control of a dragonfly with rear wings of various sizes, similar to the simulations described in chapter 5. From our previous results, we expect that the flight style, i.e. horizontal or vertical body, should change abruptly as the hind wings are reduced in size. Here 109 trials were recorded, as performed by my advisor Jane Wang. These human flights showed similar results for the change in flight style even though the wing motion varies highly from stroke to stroke.

Initial system test

Figure 6.3 reports the first data recorded using the real-time insect flight simulator. This first recording used a fruit fly as the model, with parameters as in table 4.1, which was free to move in the x,z and pitch directions. To clarify the effect of the time dilation, each graph includes two time axis. The bottom axis is time in the flight simulator, named 'insect time', and the top axis is time in the lab, named 'human time'. The insect time passes 600 times slower than human time.

The observed wing motion during this trial is similar to the wing motion described in [98]. (figure 6.3a-b) This is because I was personally flying and to test the machine I was attempting to reproduce the flight of that paper. It can be expected that most other human participants, who are not aware of how

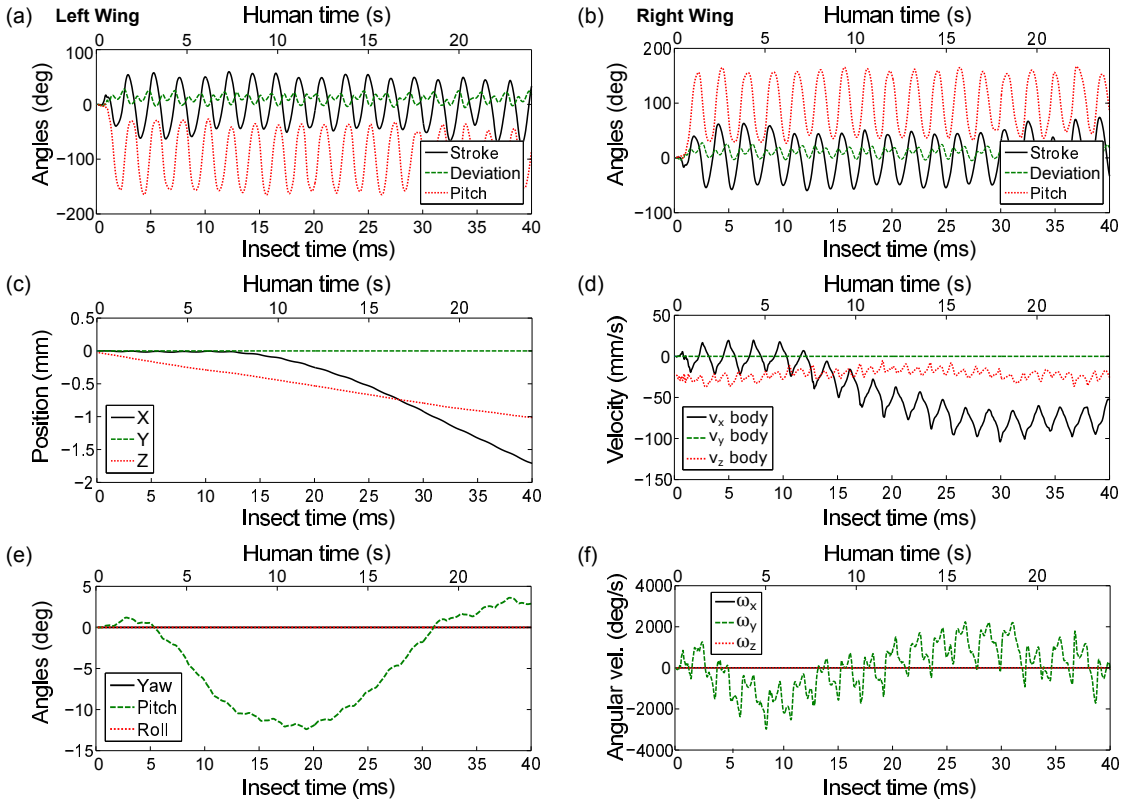

Figure 6.3: Initial data recorded from a single flight using our simulator. All data is from the same trial and provided with two aligned time axes. The bottom horizontal axis in each graph is insect time, which is the time in the simulated flight model. The upper horizontal axis is the human time, which indicates the time in the trial as measured on a watch in the lab. (a-b) Tracked orientation of the model left and right wing. Orientation is represented using stroke, deviation and pitch Euler angles. Angles are measured relative to the initial alignment position. (c-d) Body position and velocity of the fruit fly computed by the flight model. Velocity is given in body frame coordinates. (e-f) Orientation and angular velocity of the fruit fly body. Orientation is indicated by the Euler angles yaw, pitch and roll. In this trial only the right wing motion was recorded and mirrored to the left wing. This creates a left-right symmetry and ensures only x, z and pitch of the fruit fly body can change.

flies move their wings, will attempt very different wing motions. One likely case is flapping the wings up and down, which would mean the main oscillation would be observed in the deviation angle. It could be interesting to see if radically different wing motion can also be used to control the fly.

The data in figure 6.3 was recorded by tracking only the right wing and mirroring the data to the left wing. This enforces a left-right symmetry on the fruit fly body. The results is that only the x, z and body pitch variables can change during flight. This helps the control by our human participants as it keeps the fly pointing forward and stops it from drifting off sideways.

The result of the wing motion is shown in figure 6.3c-f. The vertical position is linearly decreasing, which means not enough vertical force was generated to overcome gravity. On average during this trial the generated lift force was around 0.87g and the drag due to the descending velocity helped to keep the velocity constant. A small increase in frequency or stroke amplitude in subsequent trials should be enough to maintain hovering for the fly.

The horizontal position remains stable at first, but starts to increase rapidly halfway through the trial. The reason for the sudden increase in horizontal velocity can be found in the pitch. Maintaining a stable pitch is difficult, see chapter 4, and it can be controlled through changes to the mean of the stroke [98]. Figure 6.3a-b shows clearly that the stroke on each wing beat is not identical. The mean is changing by a few degrees every time and this will cause deviations to the pitch of the fruit fly. This means this first trial data shows the start of the pitch instability described in detail earlier in figure 4.1c.

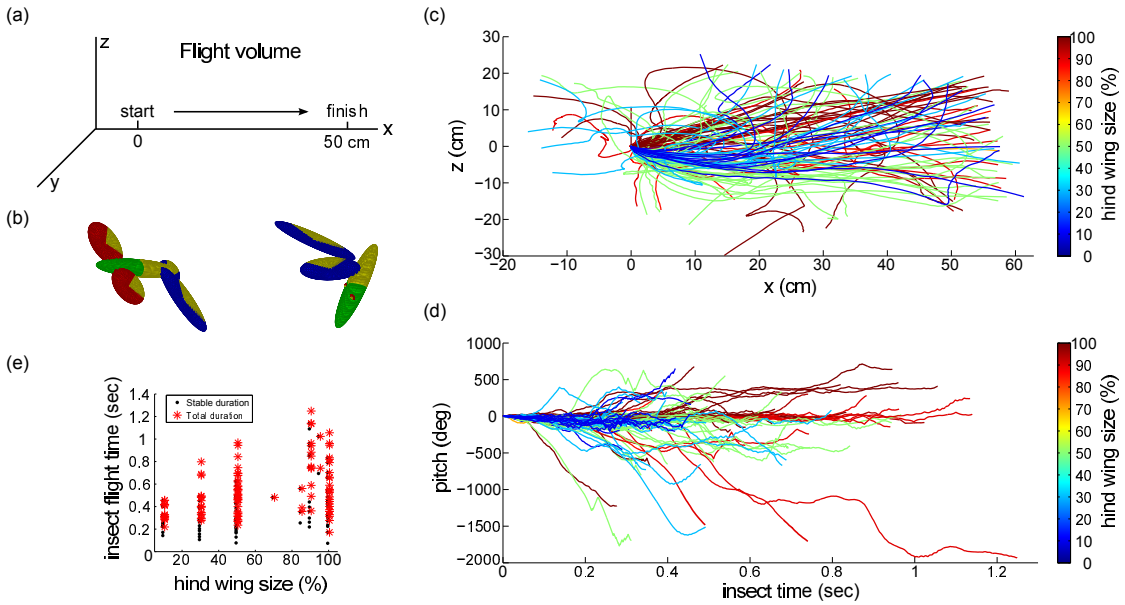

Figure 6.4: Human control of horizontal dragonfly flight. (a) 3D flight area setup. The objective was to fly from left to right on screen, corresponding to a distance of 50cm for the dragonfly. (b) Two frames captured from different trials. Yellow color indicates front of the body (green) or wings (red is hind, blue is front). Left: a dragonfly flying with the body horizontal with full sized hind wings. Right: the hind wings are reduced to 10% the original size. The human controlled flight pitches the body up. The test subject controlled the front wings, the hind wings were driven at 0.4Hz on screen (40Hz insect time). (c) Flight trajectories for all 109 performed runs, colored by the hind wing size. Most flights reach the 50cm target. It appears that for 100% hind wings (red) the trajectories end up higher than for smaller hind wings (blue/green). (d) Body pitch during flights as a function of insect time. Controlled flights will have a stable pitch over time. Large hind wing flights (red) appear to be longer and more stable. (e) Flight duration increases with hind wing size. Stable duration was measured from start to the first moment pitch reached ±180° or end of flight.

Controlling horizontal flight

The first experiments performed with the new system asked if a human could control a dragonfly well enough to fly a horizontal distance of 50cm. Given the

results from chapter 5, the stability of the dragonfly can be altered by changing the size of the hind wing to possibly vary the control task difficulty. For the simulation small hind wings resulted in unstable fruitfly-like flight, with the body pitched vertically. Each of these effects appears in the human controlled flights as well.

These experiments used the four-winged flyer based on the dragonfly, where the hind wings were driven at 0.4Hz (40Hz insect time), with parameters as in table 5.2, and the front wings were under human control. The dragonfly parameters are as described in table 5.1, with one change to the wing hinge location. The wing separation was increased from 5.94mm to 14.15mm, which makes the full hind wing flyer passively stable [122]. As the hind wing size is reduced the flyer becomes passively unstable. This was expected to create a large difference between the control difficulty for dragonfly-like flight compared to fruitfly-like flight.

Initial analysis of the results indicate that indeed the human control is affected by the hind wing size, see figure 6.4. The flight volume was setup to show a horizontal track of 50cm long and the objective was to fly from one end to the other. Figure 6.4b shows two still frames from the trials. On the left the flight is dragonfly-like with full hind wings and the body is horizontal. On the right it is fruitfly-like with small hind wings and the body has pitched up. These examples are representative for all the 109 performed trials and show that the flight style changed significantly similar to the simulation results from chapter 5.

Overall the success rate for the horizontal flying task was relatively high, as can be seen from the flight trajectories of all trials shown in figure 6.4c. Most

tracks, independent of hind wing size, reach the end of the flight volume. It seems large wing size flights (red) end up higher than the flights with smaller hind wings (green/blue). The initial direction at the starting point already seems to depend strongly on hind wing size. In addition small hind wing flights (blue) tend to drop at first and then curve upward out of the flight volume. Each of these observations can be studied to understand how the human controller was implemented.

One measure of how well the flight is controlled is the size of deviation in the body pitch during the flight, see figure 6.4d. The flights show a large amount of tumbles (rotations of 360° or more) for each size of hind wings. However the longest stable flights are clearly with large hind wings. It also seems that large hind wings are related to successful recovery from a tumble, which can be seen as a long section of pitch near an integer multiple of 360°. To quantify this further, figure 6.4e shows the total and stable duration for each flight as a function of hind wing size. Stable duration is measured as the time between start and the first time the pitch reaches 180° or the end of the flight. It seems that as the hind wings are reduced, the control is more difficult and the stable flight duration decreases. This matches with the increases in α determined in the simulation.

Many of these results will need to be investigated further and can likely be developed further. However, it is good to see qualitative agreement between the computer simulated flights and the flights performed during human trials. It shows the machine is operating as expected and can be used to study the human control of flight in great detail.

6.3 Outlook

The two tests of the human-controlled insect flight simulator indicate that a human can indeed perform the task of controlling insect flight. These experiments were so far performed by either myself or my advisor Jane Wang and thus by people well aware of how insect are controlling their flight. When trying out the system on new students, they do struggle to generate sufficient lift to counter gravity, but a short explanation of the idea of insect flight usually helps to guide them in the right direction. Controlling the stability seems to be more complicated, but a number of thorough experiments would need to be conducted to investigate the learning process and whether or not some explanations are needed.

The successful completion of the system allows for a wide variety of future studies. For example a careful study of how a human controls for the pitch instability in the fruit fly would be really interesting. Up to this point the experiments have restricted the wings to be left-right symmetric, thereby removing any roll instabilities, but this could be lifted with an additional wing model. It would allow for experiments that look at the control of the roll stability. Finally it appears that the system is good for developing an intuitive idea of the effect of different wing strokes on the flight of an insect. It is now possible to quickly try out a certain wing stroke, directly see the effect, think about an improvement and then try out the new stroke to see if it indeed has the desired result.

At the same time our flight simulator might allow for interesting experiments on human learning. For example what wing motions do people try in an attempt to learn how to fly? How many different strokes do they have to try

before they are successful? Do they all find the same stroke or are there different good solutions? And is there a structure to the learning process? Each of these questions can be investigated with the newly constructed system.

CHAPTER 7

CONCLUSION

In this thesis we gained various new insights into emergent phenomena for insect locomotion. The first two chapters covered the control algorithm of a tiger beetle as it chases its prey. A simple proportional controller relates the visual error angle to the rate of the beetle's body rotation, where the gain is proportional to the distance to the prey. The value of the controller's gain is optimized to reduce the time the body needs to align towards the prey. In addition, this control law is visible in the positioning of each of the front legs during the chase.

The second part of this thesis was concerned with insect flight and found that the wing hinge of a fruit fly is placed optimally for generating the maximum ascending speed. Moreover, this optimal design is achieved by tuning the coupled body-wing oscillations to an antiresonance. These results show the evolutionary optimization inherent in the fruit fly morphology, which maximizes lift generation, while leaving stability to be handled by an active controller through the neural system [98,100]. The nominal hinge position of the fruit fly allows for the achievement of any vertical velocity with the minimal stroke amplitude. It thus provides the widest flight velocity range, given physical limitation on the wing amplitude. The ability to achieve a large range of velocities is likely useful when escaping predators and could thus be the evolutionary advantage that helped bring the wing hinge to its current position.

Another study looked at the transition from four- to two-winged flight, by starting with the morphology of a dragonfly and systematically reducing the hind wings. A rapid transition between horizontal and vertical body flight styles naturally arose. This switch occurred as soon as the front wings started

to adjust for the loss of hind lift. Using hind wing adjustments could delay the transition, but ultimately not stop it from happening. Crucially, going from a horizontal to a vertical body pitch resulted in reduced power consumption during flight. The advantage of moving to two-winged flight could thus be the need to reduce the required food intake of the insect.

These two examples show that simple guiding principles for insect locomotion can emerge out of complex systems with very different temporal and spacial dimensions. In the case of the tiger beetle the complex system comprises the fast interactions in the neural circuitry of a single beetle, while for insect flight it is the slow evolutionary process of whole species. Interestingly, in both cases an optimization criterion emerged that could explain the morphological parameters. This optimal design appears more often in biological systems in general [134]. Moreover, this result validates the idea behind using neural nets or genetic algorithms for machine learning. Mimicking these natural complex systems in optimization algorithms could lead to improved results.

Optimal emergent phenomena can likely also be found in other areas of insect locomotion. Examples could include movement patterns for discovering new spaces that minimize energy consumption or escape reactions that maximize the chance of survival. One particular intriguing area where emergent principles could appear is in the learning process for developing new skills. If an optimal criterion exists here, it will likely be the fastest possible learning rate given some unknown restrictions. To study this idea the final chapter of this thesis described the construction of an interactive flight simulation that allowed a human to learn to fly as an insect.

The initial results from the interactive flight simulation show that it is indeed possible for a human to produce the required lift and stabilize the flight for both fruit flies and dragonflies. With this newly constructed machine, it is possible to perform experiments that investigate how the human control strategies are implemented and how those develop over time. Hopefully these experiments will discover new emergent principles in the learning process for the control of locomotion.

More broadly, emergence can be a good mechanism to understand the biological complexity of Nature and searching for simple laws arising from this complexity could lead to practical results. One particular area where I hope this approach can be helpful is in advancing the understanding our own human brain. Knowing the physics and chemistry of individual neurons is not enough to understand how the nervous system of an organism will behave. The network of interconnected neurons will play an essential role in the formation of behavior. While insect's brains are already hard enough to understand, the much more advanced human brain will provide an even greater challenge.

However, even in the human brain some tasks are likely easier to understand than others. Brain activity related to locomotion will probably be understood first as it might be similar to other animals or insects. These tasks had to be solved early on during evolution and the circuitry can thus be expected to show large similarities between species. Next, the formations of individual emotions should be investigated, as they appear to be a natural step up in complexity after locomotor functions. Emotional responses probably also arise naturally out a sufficiently large network of neurons. Finally, the most intriguing and complex question would be whether we can understanding the formation of

consciousness. It seems unlikely that we find consciousness in a single neuron. Instead it will have to emerge out of the nervous system, or even the body, as a whole. Yet, it is completely unknown what the required network complexity is, or what other elements are needed.

In summary, when it comes to understanding complex systems, a reductionist approach might not always work and it is important to study the system as a whole. The whole is simply greater than the sum of its parts.

BIBLIOGRAPHY

[1] E. Von Holst. Relations between the central nervous system and the peripheral organs. *Anim. Behav.*, 2(3):89–94, 1954.

[2] N. Tinbergen. On war and peace in animals and man. *Science*, 160(3835):1411–1418, 1968.

[3] B.F. Skinner. *The behavior of organisms: An experimental analysis*. BF Skinner Foundation, 1990.

[4] E.A. Smith and B. Winterhalder. *Evolutionary ecology and human behavior*. Transaction Publishers, 1992.

[5] M.K. McBeath, D.M. Shaffer, and M.K. Kaiser. How baseball outfielders determine where to run to catch fly balls. *Science*, 268(5210):569–573, 1995.

[6] G. Gigerenzer and D.G. Goldstein. Reasoning the fast and frugal way: models of bounded rationality. *Psychol. Rev.*, 103(4):650, 1996.

[7] R.M. Alexander. *Principles of animal locomotion*. Princeton University Press, 2003.

[8] S. Vogel. *Comparative biomechanics: life's physical world*. Princeton University Press, 2013.

[9] A.F. Haselsteiner, C. Gilbert, and Z.J. Wang. Tiger beetles pursue prey using a proportional control law with a delay of one half-stride. *J. R. Soc. Interface*, 11(95):20140216, 2014.

[10] D.A. Levitis, W.Z. Lidicker, and G. Freund. Behavioural biologists do not agree on what constitutes behaviour. *Anim. Behav.*, 78(1):103–110, 2009.

[11] R. Shadmehr and S.P. Wise. *The computational neurobiology of reaching and pointing: a foundation for motor learning*. MIT press, 2005.

[12] P.W. Anderson. More is different. *Science*, 177(4047):393–396, 1972.

[13] R.B. Laughlin and D. Pines. The theory of everything. *Proc. Natl. Acad. Sci. U.S.A.*, 97(1):28–31, 2000.

[14] J. Kwapień and S. Drożdż. Physical approach to complex systems. *Phys. Rep.*, 515(3):115–226, 2012.

[15] G.P. Shpenkov. *Friction surface phenomena*, volume 29. Elsevier, 1995.

[16] H.E. Stanley. *Introduction to Phase Transitions and Critical Phenomena*. Oxford University Press, 1971.

[17] F. Cucker and S. Smale. Emergent behavior in flocks. *IEEE Trans. Autom. Control*, 52(5):852–862, 2007.

[18] Y. Katz, K. Tunstrøm, C.C. Ioannou, C. Huepe, and I.D. Couzin. Inferring the structure and dynamics of interactions in schooling fish. *Proc. Natl. Acad. Sci. U.S.A.*, 108(46):18720–18725, 2011.

[19] S.W. Hawking. Particle creation by black holes. *Commun. Math. Phys.*, 43(3):199–220, 1975.

[20] Nathan Seiberg. Emergent spacetime. *arXiv preprint hep-th/0601234*, 2006.

[21] E. Verlinde. On the origin of gravity and the laws of newton. *J. High Energy Phys.*, 2011(4):1–27, 2011.

[22] J.B.S. Haldane. *The causes of evolution*. Princeton University Press, 1990.

[23] G.A. Parker, J.M. Smith, et al. Optimality theory in evolutionary biology. *Nature*, 348(6296):27–33, 1990.

[24] R.M.N. Alexander. *Optima for animals*. Princeton University Press, 1996.

[25] G.J. Berman and Z.J. Wang. Energy-minimizing kinematics in hovering insect flight. *J. Fluid Mech.*, 582:153–168, 2007.

[26] D. Grimaldi and M.S. Engel. *Evolution of the Insects*. Cambridge University Press, 2005.

[27] A.K. Brodsky. *The evolution of insect flight*. Oxford University Press Inc., New York, 1996.

[28] R.M. Noest and Z Jane Wang. A tiger beetles pursuit of prey depends on distance. *Phys. Biol.*, 14(2):026004, 2017.

[29] M.F. Land and T.S. Collett. Chasing behaviour of houseflies (fannia canicularis). *J. Comp. Physiol.*, 89(4):331–357, 1974.

[30] T.S. Collett and M.F. Land. Visual control of flight behavior in the hoverfly, *syritta pipiens l. J. Comp. Physiol.*, 99:1–66, 1975.

[31] T.S. Collett and M.F. Land. How hoverflies compute interception courses. *J. Comp. Physiol.*, 125(3):191–204, 1978.

[32] C. Gilbert. Visual control of cursorial prey pursuit by tiger beetles (cicindelidae). *J. Comp. Physiol. A*, 181(3):217–230, 1997.

[33] K. Ghose, T.K. Horiuchi, P.S. Krishnaprasad, and C.F. Moss. Echolocating bats use a nearly time-optimal strategy to intercept prey. *PLoS Biol.*, 4(5):e108, 2006.

[34] R.M. Olberg. Visual control of prey-capture flight in dragonflies. *Curr. Opin. Neurobiol.*, 22(2):267–271, 2012.

[35] D.B. Zurek, M.Q. Perkins, and C. Gilbert. Dynamic visual cues induce jaw opening and closing by tiger beetles during pursuit of prey. *Biol. Lett.*, 10(11):20140760, 2014.

[36] M. Mischiati, H.-T. Lin, P. Herold, E. Imler, R. Olberg, and A. Leonardo. Internal models direct dragonfly interception steering. *Nature*, 517(7534):333–338, 2015.

[37] M. Egelhaaf, K. Hausen, W. Reichardt, and C. Wehrhahn. Visual course control in flies relies on neuronal computation of object and background motion. *Trends Neurosci.*, 11(8):351–358, 1988.

[38] M.V. Srinivasan and S. Zhang. Visual motor computations in insects. *Annu. Rev. Neurosci.*, 27(1):679–696, 2004.

[39] E.D. Tytell, P. Holmes, and A.H. Cohen. Spikes alone do not behavior make: why neuroscience needs biomechanics. *Curr. Opin. Neurobiol.*, 21(5):816–822, 2011.

[40] M. Egelhaaf, R. Kern, and J.P. Lindemann. Motion as a source of environmental information: a fresh view on biological motion computation by insect brains. *Front. Neural. Circuits*, 8:127, 2014.

[41] N.J. Cowan, M.M. Ankarali, J.P. Dyhr, M.S. Madhav, E. Roth, S. Sefati, S. Sponberg, S.A. Stamper, E.S. Fortune, and T.L. Daniel. Feedback control as a framework for understanding tradeoffs in biology. *Integr. Comp. Biol.*, 54(2):223–237, 2014.

[42] J.-M. Mongeau, S.N. Sponberg, J.P. Miller, and R.J. Full. Sensory processing within cockroach antenna enables rapid implementation of feedback control for high-speed running maneuvers. *J. Exp. Biol.*, 218(15):2344–2354, 2015.

[43] A. Cloarec. Distance and size discrimination in a water stick insect, ranatra linearis (heteroptera). *J. Exp. Biol.*, 120(1):59–77, 1986.

[44] W.M. Farina, D. Varjú, and Y. Zhou. The regulation of distance to dummy flowers during hovering flight in the hawk moth macroglossum stellatarum. *J. Comp. Physiol. A*, 174(2):239–247, 1994.

[45] A. Mizutani and Y. Toh. Behavioral analysis of two distinct visual responses in the larva of the tiger beetle (cicindela chinensis). *J. Comp. Physiol. A*, 182(3):277–286, 1998.

[46] R.M. Olberg, A.H. Worthington, J.L. Fox, C.E. Bessette, and M.P. Loosemore. Prey size selection and distance estimation in foraging adult dragonflies. *J. Comp. Physiol. A*, 191(9):791–797, 2005.

[47] Z.J. Wang. On the instability and critical damping conditions, $k\tau = 1/e$ and $k\ tau = \pi/2$ of the equation $\dot{\theta} = -k\theta(t - \tau)$. *arXiv preprint:1404.4763*, 2014.

[48] J.J. Gibson. Visually controlled locomotion and visual orientation in animals. *Br. J. Psychol.*, 49(3):182–194, 1958.

[49] D.N Lee. A theory of visual control of braking based on information about time-to-collision. *Perception*, 5(4):437–459, 1976.

[50] H. Wagner. Flow-field variables trigger landing in flies. *Nature*, 297(5862):147–148, 1982.

[51] H. Sun and B.J. Frost. Computation of different optical variables of looming objects in pigeon nucleus rotundus neurons. *Nat. Neurosci.*, 1(4):296–303, 1998.

[52] N. Hatsopoulos, F. Gabbiani, and G. Laurent. Elementary computation of object approach by a wide-field visual neuron. *Science*, 270(5238):1000–1003, 1995.

[53] M.V. Srinivasan, M. Poteser, and K. Kral. Motion detection in insect orientation and navigation. *Vision Res.*, 39(16):2749–2766, 1999.

[54] J.J. Gibson. *The perception of the visual world*. Houghton Mifflin, 1950.

[55] T.S. Collett. Short communication: Peering-a locust behaviour pattern for obtaining motion parallax information. *J. Exp. Biol.*, 76(1):237–241, 1978.

[56] E.S. Eriksson. Movement parallax and distance perception in the grasshopper (phaulacridium vittatum (sjöstedt)): Short communications. *J. Exp. Biol.*, 86(1):337–340, 1980.

[57] E.C. Sobel. The locust's use of motion parallax to measure distance. *J. Comp. Physiol. A*, 167(5):579–588, 1990.

[58] M.V. Srinivasan, M. Lehrer, S.W. Zhang, and G.A. Horridge. How honeybees measure their distance from objects of unknown size. *J. Comp. Physiol. A*, 165(5):605–613, 1989.

[59] K. Kral. Behavioural–analytical studies of the role of head movements in depth perception in insects, birds and mammals. *Behav. Processes*, 64(1):1–12, 2003.

[60] F. van Breugel, K. Morgansen, and M.H. Dickinson. Monocular distance estimation from optic flow during active landing maneuvers. *Bioinspir. Biomim.*, 9(2):025002, 2014.

[61] G.K. Wallace. Visual scanning in the desert locust schistocerca gregaria forskl. *J. Exp. Biol.*, 36(3):512–525, 1959.

[62] Y. Toh, J.-Y. Okamura, and Y. Takeda. Distance and size estimation in the tiger beetle larva: Behavioral, morphological, and electrophysiological approaches. In *The Neural Basis of Early Vision*, pages 80–85. Springer-Verlag, 2003.

[63] J.E. Layne, P.W. Chen, and C. Gilbert. The role of target elevation in prey selection by tiger beetles (carabidae: Cicindela spp.). *J. Exp. Biol.*, 209(21):4295–4303, 2006.

[64] J.E. Kuster and W.G. Evans. Visual fields of the compound eyes of four species of cicindelidae (coleoptera). *Can. J. Zool.*, 58(3):326–336, 1980.

[65] G.A. Horridge. Insects which turn and look. *Endeavour*, 1:7–17, 1977.

[66] T.S. Collett and J. Zeil. Flights of learning. *Curr. Dir. Psychol. Sci.*, 5(5):149–155, 1996.

[67] M.H. Dickinson, C.T. Farley, R.J. Full, M.A.R. Koehl, R. Kram, and S. Lehman. How animals move: An integrative view. *Science*, 288(5463):100–106, 2000.

[68] S. Rossignol, R. Dubuc, and J.-P. Gossard. Dynamic sensorimotor interactions in locomotion. *Physiol. Rev.*, 86(1):89–154, 2005.

[69] R.E. Ritzmann and A. Büschges. Adaptive motor behavior in insects. *Curr. Opin. Neurobiol.*, 17(6):629–636, 2007.

[70] A. Büschges, T. Akay, J.P. Gabriel, and J. Schmidt. Organizing network action for locomotion: Insights from studying insect walking. *Brain Res. Rev.*, 57(1):162–171, 2008.

[71] A. Ayali, E. Couzin-Fuchs, I. David, O. Gal, P. Holmes, and D. Knebel. Sensory feedback in cockroach locomotion: current knowledge and open questions. *J. Comp. Physiol. A*, 201(9):841–850, 2015.

[72] T. Buschmann, A. Ewald, A. von Twickel, and A. Büschges. Controlling legs for locomotion - insights from robotics and neurobiology. *Bioinspir. Biomim.*, 10(4):041001, 2015.

[73] H. Cruse. The function of the legs in the free walking stick insect, *carausius morosus*. *J. Comp. Physiol.*, 112(2):235–262, 1976.

[74] D.L. Jindrich and R.J. Full. Many-legged maneuverability: dynamics of turning in hexapods. *J. Exp. Biol.*, 202(12):1603–1623, 1999.

[75] C. Zollikofer. Stepping patterns in ants - influence of speed and curvature. *J. Exp. Biol.*, 192(1):95–106, 1994.

[76] D. Graham. A behavioural analysis of the temporal organisation of walking movements in the 1st instar and adult stick insect (carausius morosus). *J. Comp. Physiol.*, 81(1):23–52, 1972.

[77] V. Zolotov, L. Frantsevich, and E.-M. Falk. Kinematik der phototaktischen drehung bei der honigbieneapis mellifera l. *J. Comp. Physiol.*, 97(4):339–353, 1975.

[78] R. Franklin, W.J. Bell, and R. Jander. Rotational locomotion by the cockroach blattella germanica. *J. Insect Physiol.*, 27(4):249–255, 1981.

[79] L.I. Frantsevich and P.A. Mokrushov. Turning and righting ingeotrupes (coleoptera, scarabaeidae). *J. Comp. Physiol.*, 136(4):279–289, 1980.

[80] J.P. Jander. Mechanical stability in stick insects when walking straight and around curves. In M. Gewecke and G. Wendler, editors, *Insect locomotion*. Berlin: Parey, 1985.

[81] V. Dürr and W. Ebeling. The behavioural transition from straight to curve walking: kinetics of leg movement parameters and the initiation of turning. *J. Exp. Biol.*, 208(12):2237–2252, 2005.

[82] H. Cruse. Which parameters control the leg movement of a walking insect? I. Velocity control during the stance phase. *J. Exp. Biol.*, 116(1):343–355, 1985.

[83] T.G. Brown. The intrinsic factors in the act of progression in the mammal. *Proc. R. Soc. B*, 84(572):308–319, 1911.

[84] Fred Delcomyn. Insect locomotion on land. In *Locomotion and energetics in arthropods*, pages 103–125. Springer, 1981.

[85] A. Büschges, H. Scholz, and A. El Manira. New moves in motor control. *Curr. Biol.*, 21(13):R513–R524, 2011.

[86] R. Eckhorn, R. Bauer, W. Jordan, M. Brosch, W. Kruse, M. Munk, and H.J. Reitboeck. Coherent oscillations: A mechanism of feature linking in the visual cortex? *Biol. Cybern.*, 60(2):121–130, 1988.

[87] E.R. Kandel, J.H. Schwartz, T.M. Jessell, S.A. Siegelbaum, and A.J. Hudspeth. *Principles of neural science*, volume 4. McGraw-hill New York, 2000.

[88] R.M. Noest and Z Jane Wang. Optimal wing hinge position for fast ascent in a model fly. *J. Fluid Mech.*, 2017.

[89] T. Weis-Fogh. Quick estimates of flight fitness in hovering animals, including novel mechanisms for lift production. *J. Exp. Biol.*, 59(1):169–230, 1973.

[90] C.P. Ellington. Aerodynamics and the origin of insect flight. *Adv. Insect Physiol.*, 23:171–210, 1991.

[91] R.M. Alexander. Design by numbers. *Nature*, 412(6847):591–591, 2001.

[92] U. Pesavento and Z.J. Wang. Flapping wing flight can save aerodynamic power compared to steady flight. *Phys. Rev. Lett.*, 103(11):118102, 2009.

[93] M. Vanella, T. Fitzgerald, S. Preidikman, E. Balaras, and B. Balachandran. Influence of flexibility on the aerodynamic performance of a hovering wing. *J. Exp. Biol.*, 212(1):95–105, 2009.

[94] R.P. Ray, T. Nakata, P. Henningsson, and R.J. Bomphrey. Enhanced flight performance by genetic manipulation of wing shape in drosophila. *Nat. Commun.*, 7:10851, 2016.

[95] G. Fraenkel and J.W.S. Pringle. Biological sciences: halteres of flies as gyroscopic organs of equilibrium. *Nature*, 141:919–920, 1938.

[96] J.W.S. Pringle. The gyroscopic mechanism of the halteres of diptera. *Phil. Trans. of the R. Soc. of London B: Bio. Sciences*, 233(602):347–384, 1948.

[97] G.K. Taylor and H.G. Krapp. Sensory systems and flight stability: what do insects measure and why? *Adv. Insect Physiol.*, 34:231–316, 2007.

[98] S. Chang and Z.J. Wang. Predicting fruit fly's sensing rate with insect flight simulations. *Proc. Natl. Acad. Sci. U.S.A.*, 111(31):11246–11251, 2014.

[99] G. Fraenkel. The function of the halteres of flies (diptera). In *Proc. Zool. Soc. Lond.*, volume 109, pages 69–78. Wiley Online Library, 1939.

[100] L. Ristroph, G. Ristroph, S. Morozova, A.J. Bergou, S. Chang, J. Guckenheimer, Z.J. Wang, and I. Cohen. Active and passive stabilization of body pitch in insect flight. *J. R. Soc. Interface*, 10(85):20130237, 2013.

[101] L.F. Shampine and M.K. Gordon. *Computer solution of ordinary differential equations: the initial value problem*, volume 85. WH Freeman San Francisco, 1975.

[102] Z.J. Wang. Dissecting insect flight. *Annu. Rev. Fluid Mech.*, 37:183–210, 2005.

[103] U. Pesavento and Z.J. Wang. Falling paper: Navier-stokes solutions, model of fluid forces, and center of mass elevation. *Phys. Rev. Lett.*, 93(14):144501, 2004.

[104] A. Andersen, U. Pesavento, and Z.J. Wang. Unsteady aerodynamics of fluttering and tumbling plates. *J. Fluid Mech.*, 541:65–90, 2005.

[105] L B. Tuckerman. Inertia factors of ellipsoids for use in airship design. Technical report, Bureau of Standards, 1926.

[106] R. Grimshaw. *Nonlinear ordinary differential equations*, volume 2. CRC Press, 1991.

[107] M. Sun, J. Wang, and Y. Xiong. Dynamic flight stability of hovering insects. *Acta Mech. Sin.*, 23(3):231–246, 2007.

[108] S.P. Sane and M.H. Dickinson. The control of flight force by a flapping wing: lift and drag production. *J. Exp. Biol.*, 204(15):2607–2626, 2001.

[109] S. Alben. Optimal flexibility of a flapping appendage in an inviscid fluid. *J. Fluid Mech.*, 614:355–380, 2008.

[110] C.P. Ellington. The aerodynamics of hovering insect flight. iii. kinematics. *Phil. Trans. of the R. Soc. of London B: Bio. Sciences*, 305(1122):41–78, 1984.

[111] C.H. Greenewalt. The wings of insects and birds as mechanical oscillators. *Proc. Am. Philos. Soc.*, 104(6):605–611, 1960.

[112] C.H. Greenewalt. Dimensional relationships for flying animals. *Smithson. Misc. Collect.*, 144:1–46, 1962.

[113] M.L. May. Heat exchange and endothermy in protodonata. *Evolution*, 36(5):1051–1058, 1982.

[114] A. Azuma, S. Azuma, I. Watanabe, and T. Furuta. Flight mechanics of a dragonfly. *J. Exp. Biol.*, 116(1):79–107, 1985.

[115] Z.Jane Wang and D. Russell. Effect of forewing and hindwing interactions

on aerodynamic forces and power in hovering dragonfly flight. *Phys. Rev. Lett.*, 99(14):148101, 2007.

[116] J.M. Wakeling and C.P. Ellington. Dragonfly flight. iii. lift and power requirements. *J. Exp. Biol.*, 200(3):583–600, 1997.

[117] S.N. Fry, R. Sayaman, and M.H. Dickinson. The aerodynamics of free-flight maneuvers in drosophila. *Science*, 300(5618):495–498, 2003.

[118] J.A. Thomas, J.W.H. Trueman, A. Rambaut, and J.J. Welch. Relaxed phylogenetics and the palaeoptera problem: resolving deep ancestral splits in the insect phylogeny. *Systematic biology*, 62(2):285–297, 2013.

[119] S.D. Weatherbee, G. Halder, J. Kim, A. Hudson, and S. Carroll. Ultrabithorax regulates genes at several levels of the wing-patterning hierarchy to shape the development of the drosophila haltere. *Genes Dev.*, 12(10):1474–1482, 1998.

[120] B.M. Hersh, C.E. Nelson, S.J. Stoll, J.E. Norton, T.J. Albert, and S.B. Carroll. The UBX-regulated network in the haltere imaginal disc of D. melanogaster. *Dev. Biol.*, 302(2):717–727, 2007.

[121] F.T. Muijres, N.A. Iwasaki, M.J. Elzinga, J.M. Melis, and M.H. Dickinson. Flies compensate for unilateral wing damage through modular adjustments of wing and body kinematics. *Interface Focus*, 7(1):20160103, 2017.

[122] J. Melfi. *Flight Mechanics Of The Dragonfly*. PhD thesis, Cornell University, 2016.

[123] Ovid. Metamorphoseon libri, 8AD. Book VIII:183-235.

[124] M.H. Dickinson, F.-O. Lehmann, and S.P. Sane. Wing rotation and the aerodynamic basis of insect flight. *Science*, 284(5422):1954–1960, 1999.

[125] A.J. Bergou, L. Ristroph, J. Guckenheimer, I. Cohen, and Z.J. Wang. Fruit flies modulate passive wing pitching to generate in-flight turns. *Phys. Rev. Lett.*, 104(14):148101, 2010.

[126] M. Sun. Insect flight dynamics: stability and control. *Rev. Mod. Phys.*, 86(2):615–646, 2014.

[127] D.M. Wolpert, Z. Ghahramani, and M.I. Jordan. An internal model for sensorimotor integration. *Science*, 269(5232):1880–1882, 1995.

[128] E. Todorov and M.I. Jordan. Optimal feedback control as a theory of motor coordination. *Nat. Neurosci.*, 5(11):1226–1235, 2002.

[129] M. Desmurget and S. Grafton. Forward modeling allows feedback control for fast reaching movements. *Trends Cogn. Sci.*, 4(11):423–431, 2000.

[130] C.A. Buneo, M.R. Jarvis, A.P. Batista, and R.A. Andersen. Direct visuomotor transformations for reaching. *Nature*, 416(6881):632–636, 2002.

[131] B.T. Fang. Trilateration and extension to global positioning system navigation. *J. Guid. Control Dyn.*, 9(6):715–717, 1986.

[132] C.C. Hsieh, Y.C. Fang, M.E. Wang, C.K. Wang, M.J. Kim, S.Y. Shin, and T.C. Woo. Noise smoothing for VR equipment in quaternions. *IIE Trans.*, 30(7):581–587, 1998.

[133] M.-J. Kim, M.-S. Kim, and S.Y. Shin. A C^2-continuous B-spline quaternion curve interpolating a given sequence of solid orientations. In *Proc. Comp. Anim.*, pages 72–81. IEEE, 1995.

[134] W. Bialek. Physical limits to sensation and perception. *Annu. Rev. Biophys. Biophys. Chem.*, 16(1):455–478, 1987.